SAFETY IN MINES RESEARCH ADVISORY COMMITTEE

SIMRAC

Final Project Report

Title: DEVELOP A QUANTITATIVE UNDERSTANDING OF ROCKMASS BEHAVIOUR NEAR EXCAVATIONS IN DEEP MINES

Part 2: Chapters 3 - 6

Author/s: JAL Napier, MW Hildyard, JS Kuijpers, A Daehnke, EF Sellers, DF Malan, E Siebrits, MU Özbay, T Dede and PA Turner

Research Agency: CSIR: Division of Mining Technology

Project No: GAP 029

Date: December 1995

3. METHODS TO ANALYSE THE MECHANICS OF THE STOPE FRACTURE ZONE

Modelling of failure processes in rock is an essential adjunct to the analysis of observations of underground rock fracturing. The identification of mechanisms of deformation represents a basic step in the understanding of rock mass behaviour and provides a foundation for the prediction of this behaviour in different geological settings and at different working depths. In a number of instances it may be appropriate to apply very simple and mathematically tractable models to the analysis of stress distributions around openings in elastic ground. The two-dimensional solutions for a parallel sided panel with and without closure, two parallel panels, a solid ribside, an isolated pillar and an infinite series of adjacent panels are particularly useful in this respect (Salamon 1968). It is also apparent that these idealized models are limited in predicting the behaviour of mine openings close to the working face and, in particular, the interaction of support systems with the fractured rock near the stope face. In these cases the elastic models generally predict a tensile stress parallel to the hangingwall and footwall which is not consistent with the general self-stability of openings at depth in deep level gold mines.

The representation of inelastic deformation processes and rock failure phenomena in computer models presents a number of difficulties. One general approach to inelastic modelling is to use plasticity theory to represent the incremental changes in the inelastic components of strain at all positions within the domain of interest. The problem analysis requires the specification of both the failure conditions of the rock mass and the rules relating incremental strains to incremental stress changes once failure has occurred. This approach can be implemented using finite element and finite difference numerical techniques. In brittle materials failure is observed to occur either as tension or extension fractures which follow the direction of the major principal stress or as localized shear bands that are inclined to the major principal stress direction. To represent these failure processes the continuum-based finite element or finite difference analyses must be carried out using sufficiently fine mesh gridding to delineate localized failure zones. This can be an inefficient process and can obscure failure patterns.

An alternative approach is to assume that the positions of major faults and fractures are pre-defined and then to solve the resulting system as a set of interacting cracks and blocks that are elastic or plastically deformable and which move according to Newtonian mechanics. This approach has been termed the Distinct Element Method (DEM) by Cundall (Cundall 1988) and has proved to be of great utility in solving a variety of geotechnical problems ranging from rock slope stability to keyblock analyses. The DEM forms a natural extension to keyblock theory as developed by Goodman (Goodman and Shi 1985). Computer codes have been produced, for example, by Cundall (UDEC and 3DEC, Cundall 1988) and by Gen-Hua Shi (Goodman and Shi 1985) for the solution of multiple interacting block assemblies. One facet of the analysis of interacting block systems is the need to maintain lists of all specified block positions and to resolve the mechanical interactions between corners and edges as the blocks move relative to one another. The entire system is updated in a series of incremental time steps that depend on the properties of the block contact interfaces. In particular, the interface stiffness determines the critical length of the timestep that is needed to advance the system state incrementally. High contact stiffnesses demand small time steps and consequently result in long run times for problem analyses. One of the major disadvantages of the DEM for the analysis of stope fracturing is that all discontinuities have to be specified at the start of the problem. This drawback can be overcome partially if the domain of interest is covered by a random mesh which defines the boundaries of interacting blocks which can then be mobilized selectively.

A further simplification to the problem of modelling discontinuum structures can be made if the movements on all discontinuities are sufficiently small so that small strain approximations are acceptable. This assumption is realistic in deep mining problems relating to the formation of fractures ahead of or near to the stope face. The assumptions are obviously inappropriate if an explicit analysis of dislodged or falling blocks is considered. In the analysis of stope or tunnel design procedures, the dislodgement of a keyblock is of secondary interest to establishing the conditions that will lead to the block instability and the support requirements that must be designed to prevent rockfalls. It can be argued therefore that the assumption of small strain is acceptable in many instances in analysing the formation and propagation of the fracture zone around openings in brittle rock. This admits the possibility of using an alternative numerical approach to the solution of multiple interacting fractures by means of strain dislocations which are introduced into an elastic continuum at the positions of the fractures.

Work carried out as part of enabling output 2 is reported in the subsequent sections. This covers the development of the DIGS computer code, studies of micro-fracturing, physical modelling and numerical simulation of fracturing processes. The project plan detailed objectives for enabling output 2 are listed below for reference.

Objective 2.1 *Develop micro-mechanical models to encapsulate the onset of fracturing and to reflect the fracture mechanism of extension and shear failure and implement these models in numerical procedures.*

Objective 2.2 *Characterize using physical and numerical modelling, the mechanisms controlling the failure of rock in a stable manner or as a violent release of seismic energy in relation to both the fundamental properties of the rock type and to the geometric characteristics of an excavation and its geological environment.*

Objective 2.3 *Investigate, by means of physical models, underground observations and numerical models, the propagation of fractures from discontinuities and the interaction of growing fractures with existing discontinuities.*

Objective 2.4 *Identify the rockmass and geometric mechanisms controlling the spacing and orientation of fractures near stopes, the stability of the overall fracture zone that is generated and the effects of support and face advance increment size.*

Objective 2.5 *Improve the fracture mechanics basis for fracture propagation rules in numerical models (DIGS) and incorporate effects of fracture energy, slip weakening, dilation and automatic fracture mode selection.*

Objective 2.6 *Investigate better numerical representation of displacement discontinuity smoothness in DIGS to allow larger problems to be solved and to resolve difficulties of fracture intersection modelling.*

Objective 2.7 *Incorporate multiple material regions in DIGS to allow dykes or sills or other regional variations in material properties to be modelled.*

Objective 2.8 *Improve DIGS iteration efficiency for multiple material problems.*

Objective 2.9 *Control rigid body modes arising from detached or rotating blocks formed between fractures and other discontinuities or excavation surfaces.*

Objective 2.10 *Incorporate simple fluid flow logic in fracture propagation modelling to facilitate simulations of blast fracturing, hydraulic fracturing and fluid injection.*

Objective 2.11 *Develop methods to explore some three-dimensional fracture propagation and fracture interaction problems associated with lead-lag face geometries.*

3.1 DEVELOPMENT OF COMPUTER CODE DIGS

The use of small strain dislocations to represent slip and opening movements on faults and narrow tabular stopes is well-known in the South African mining context in terms of Salamon's "Face Element Principle" or the "Displacement Discontinuity Method (DDM)" and has been used in the development of the MINSIM computer codes by Deist, Moris and Georgiadis (Plewman et. al. 1969, Deist et. al. 1972) and later by Ryder and Napier, 1985. Both two- and three-dimensional versions of this technique have been embodied also in the computer codes MINAP, BESOL and MSCALC developed by Crouch (Crouch 1976). In order to analyse the evolution of fracturing around mine openings, Napier proposed that the DDM could be extended to model explicit fracture growth by joining discontinuity elements end-to-end in sequence according to postulated fracture growth rules (Napier 1990, Napier and Hildyard 1992). This approach allows for the interactive evolution of the fracture zone around a progressively extended opening and does not make any pre-judgement about the fracture orientations. If sufficiently many of these discontinuities are included in a stope scale problem, it is argued that they will provide a good representation of the overall inelastic damage processes near the mine openings. At a finer level of detail it is of great importance to understand the transition between the formation of fractures in direct tension and the formation of localized shear bands comprising a complicated assembly of tension or extension fractures. Insights into these phenomena can be gained by studying micro mechanical models of granular assemblies that can reveal the basic failure mechanisms. This fracture growth simulation procedure is embodied in the computer code DIGS (Discontinuity Interaction and Growth Simulation) (Napier 1990). A major advantage of the DIGS approach when compared to the Distinct Element method, is that no extensive lists of block positions or explicit block interactions have to be maintained. It should be noted that in the current implementation of the DIGS code elastodynamic effects are neglected. These effects can be included in the problem formulation by the use of special time-dependant influence functions for moving discontinuities (Siebrits and Crouch 1995). However, the numerical procedures become considerably more complicated and computationally arduous and the implementation of true dynamic fracture propagation capabilities has not yet been accomplished.

While providing a useful and insightful facility for the simulation of problems comprising several hundred fractures, a number of difficulties have impeded the application of the DIGS concept to large-scale multiple mining step problems. Poor iterative behaviour can result if largely disparate element sizes are used or if intersection angles between elements become too acute (less than twenty degrees). Additional problems have centred on the formulation of appropriate growth rules for the nucleation and evolution of shear bands and on the need to solve rapidly, large numbers of interacting crack elements. Some progress has been made in addressing these difficulties with good advances being made in the efficient numerical treatment of large numbers of interacting discontinuities. In order to resolve problems in the formulation of shear band growth rules, considerable attention has been given to the investigation of micro-mechanical failure mechanisms and the development of material-sensitive micro-structure models. These models have been developed in collaboration with P A Cundall using the distinct element code UDEC, and the particle flow code, PFC. In addition, special simulations of granular assemblies, comprising random mesh structures, have been undertaken using the DIGS code itself. This research effort is ongoing and particular attention must be given to relating all numerical procedures to physical model results and observed underground fracture patterns.

3.1.1 Element Shape Functions

Suppose that the region of interest is an isotropic elastic medium that is intersected by surfaces S_d across which the displacement field may be discontinuous. Define a normal vector with components $n_i(P)$ at point P of the surfaces S_d. Let $u_i(p)$ be the components of the displacement field at point p inside the body. If this point tends to a point P of the discontinuity surfaces, then the displacement discontinuity vector $D_i(P)$ is defined by the relationship

$$D_i(P) = u_i^-(P) - u_i^+(P) \qquad (3.1.1.1)$$

where

$u_i^+(P) =$ displacement vector on the positive normal side of the surface

$u_i^-(P) =$ displacement vector on the opposite side of the surface.

It is assumed that there is no jump in the traction vectors acting on each side of the discontinuity surface at point P. Define the discontinuity tensor Δ_{ij} by the relationship

$$\Delta_{ij} = \tfrac{1}{2}(D_i n_j + D_j n_i) \tag{3.1.1.2}$$

Assume that the discontinuity surfaces S_d are divided into small elements. In two-dimensional plane strain problems it is convenient to assume that each element is a straight line segment and that the components of the discontinuity tensor Δ_{ij} vary as a low order polynomial over the element. Assume that a local coordinate system (y,z) is centred on a typical element as shown in figure 3.1.1.1. The element length is $2b$ and there are three independent components of the discontinuity tensor Δ_{ij}.

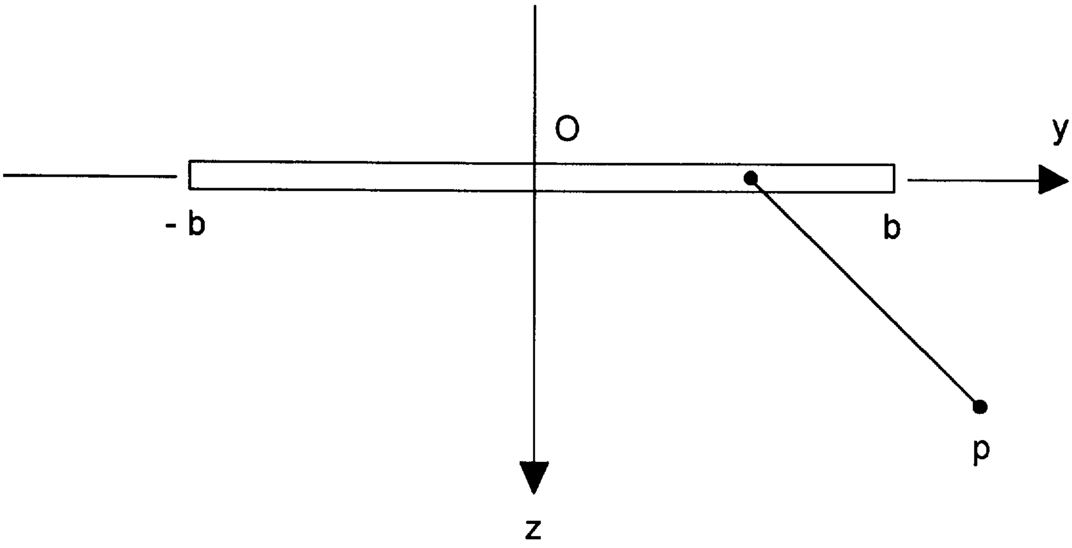

Figure 3.1.1.1 Local element coordinate system.

It can be shown (Peirce and Napier 1994) that the contribution of a given element to the total displacement field at point p is given by

$$\begin{bmatrix} u_y(p) \\ u_z(p) \end{bmatrix} = \frac{1}{8\pi(1-\nu)} \int_{-b}^{b} \begin{bmatrix} L_y & M_y & N_y \\ L_z & M_z & N_z \end{bmatrix} \begin{bmatrix} \Delta_{yy}(\eta) \\ \Delta_{yz}(\eta) \\ \Delta_{zz}(\eta) \end{bmatrix} d\eta \qquad (3.1.1.3)$$

where u_y and u_z are the local components of the displacement vector, ν is Poisson's ratio, and where

$$\begin{aligned} L_y &= (1-\nu)\Psi_{,yyy} + (2-\nu)\Psi_{,yzz} \\ M_y &= -\nu\Psi_{,yyz} + (1-\nu)\Psi_{,zzz} \\ N_y &= \nu\Psi_{,yyy} - (1-\nu)\Psi_{,yzz} \end{aligned}$$

$$\begin{aligned} L_z &= -(1-\nu)\Psi_{,yyz} + \nu\Psi_{,zzz} \\ M_z &= (1-\nu)\Psi_{,yyy} - \nu\Psi_{,yzz} \\ N_z &= (2-\nu)\Psi_{,yyz} + (1-\nu)\Psi_{,zzz} \end{aligned} \qquad (3.1.1.4)$$

In equations 3.1.1.4, the comma is used to denote derivatives of the biharmonic function Ψ which, for two-dimensional plane strain problems, is given by

$$\Psi = \tfrac{1}{2}(r^2 - r^2 \log r^2) \qquad (3.1.1.5)$$

where r is the distance between points p and Q. Ψ can be shown to satisfy the biharmonic relationship

$$\Psi_{,yyyy} + 2\Psi_{,yyzz} + \Psi_{,zzzz} = 0 \qquad (3.1.1.6)$$

It can be demonstrated (Peirce and Napier 1994) that if G is the shear modulus of the material, the contribution of the element to the total stress tensor components τ_{ij} at point p is given by

$$\begin{bmatrix} \tau_{yy}(p) \\ \tau_{yz}(p) \\ \tau_{zz}(p) \end{bmatrix} = \frac{G}{4\pi(1-\nu)} \int_{-b}^{b} \begin{bmatrix} -\Psi_{,zzzz} & \Psi_{,yzzz} & -\Psi_{,yyzz} \\ \Psi_{,yzzz} & -\Psi_{,yyzz} & \Psi_{,yyyz} \\ -\Psi_{,yyzz} & \Psi_{,yyyz} & -\Psi_{,yyyy} \end{bmatrix} \begin{bmatrix} \Delta_{yy} \\ 2\Delta_{yz} \\ \Delta_{zz} \end{bmatrix} d\eta \qquad (3.1.1.7)$$

It is important to note that the displacement components given by equation (3.1.1.3), depend only on the four independent derivatives $\Psi_{,yyy}$ $\Psi_{,yyz}$ $\Psi_{,yzz}$ and $\Psi_{,zzz}$. Using the biharmonic relationship (3.1.1.6), it can be seen that the influence matrix in equation (3.1.1.7) depends only on the four independent derivatives $\Psi_{,yyyy}$ $\Psi_{,yzzz}$ $\Psi_{,yyyz}$ and $\Psi_{,zzzz}$.

The total displacement and stress values at a given point p are estimated by summing all the contributions from each element of the discontinuity surfaces S_d. Moreover, in equations (3.1.1.3) and (3.1.1.7) all differentiations can be moved outside the integral sign since they are performed with respect to the field point p. It is then required to evaluate integrals of the form

$$I_{rs} = \int \Psi(r) \Delta_{rs} d\eta \qquad (3.1.1.8)$$

where Δ_{rs} are represented as low order polynomial functions of the local element position variable η. For example, linear variation displacement discontinuity variables are represented by

$$\Delta_{rs} = \alpha_{rs} + \beta_{rs} \eta \qquad (3.1.1.9)$$

where α_{rs} and β_{rs} are constants.

Consider the particular case of an element lying along the y-axis as shown in figure 3.1.1.1. In this case the components of the normal vector are $n_y = 0$ and $n_z = 1$ and, from equation 3.1.1.2, the discontinuity tensor components are related to the local shear and normal discontinuity components D_y and D_z by the following relations.

$$\begin{bmatrix} \Delta_{yy} \\ \Delta_{yz} \\ \Delta_{zz} \end{bmatrix} = \begin{bmatrix} 0 \\ \frac{1}{2} D_y \\ D_z \end{bmatrix} \qquad (3.1.1.10)$$

Assume that the the local shear and normal discontinuity components D_y and D_z vary linearly along the element as follows.

$$D_i = \alpha_i + \beta_i \eta \ , i = \text{y or z} \qquad .(3.1.1.11)$$

The influence coefficients in equations 3.1.1.3 and 3.1.1.7 can be evaluated by substituting equation 3.1.1.11 into equation 3.1.1.8 and then evaluating the derivatives with respect to y and z of the following two integrals.

$$D = \int_{-b}^{b} \Psi d\eta \qquad (3.1.1.12)$$

$$F = \int_{-b}^{b} \eta \Psi d\eta \qquad (3.1.1.13)$$

It can be shown that

$$D = \sum_{\varepsilon=\pm 1} \varepsilon \left[\tfrac{1}{2} (\tfrac{1}{3} B^3 + Bz^2) \log R^2 - \tfrac{2}{3} z^2 \tan^{-1}(z/B) - \tfrac{5}{18} B^3 - \tfrac{7}{6} Bz^2 \right] \qquad (3.1.1.14)$$

$$F = yD + \sum_{\varepsilon=\pm 1} \varepsilon \left[3R^4 - 3z^4 - 2R^4 \log R^2 \right] / 16 \qquad (3.1.1.15)$$

where $B = y - \varepsilon b$ and $R^2 = B^2 + z^2$.

The boundary element codes MINAP and MINSIM employ constant value displacement discontinuities (DD's) in each element. The advantage of the linear variation DD's given by equation 3.1.1.11 is improved accuracy of crack displacement values and the direct provision of crack-parallel stress components which would otherwise have to be estimated using numerical differentiation if constant strength elements are used.

It must be emphasized that boundary condition values are matched at only two points inside the domain of each element and that no continuity of the DD vector at element junctions is required. This can lead to large spurious stress values very close to element junctions. The use of higher order polynomial shape functions (quadratic, cubic etc.) in place of equation 3.1.1.11 does not eliminate the problem of singular stress values near the junction unless the continuity of the DD variation is enforced. If the DD value at a junction is continuous but the slope of the DD on each side of the junction is discontinuous, then the stress values have a logarithmic singularity close to the junction.

3.1.2 Crack Interface Logic

A variety of boundary conditions can exist at the interfaces of cracks specified in a DIGS problem analysis. These correspond to fixed specifications of the tangential and normal components of stress or displacement values at the crack surface or on one side of the crack surface. In addition to the fixed boundary conditions, constraints can be specified to limit crack interpenetration or to control crack sliding according to a given frictional resistance. A distinction must be drawn between the constitutive parameters that describe the initiation of fracture and the parameters that control the behaviour of a mobilized discontinuity. The parameters used in the DIGS code are defined in Table 3.1.2.1.

Table 3.1.2.1 Discontinuity constitutive parameters.

PARAMETER	UN-MOBILIZED	MOBILIZED
Friction angle	ϕ'	ϕ
Dilation angle	-	ψ, ψ_{rev}
Cohesion	S_0'	S_0
Cohesion weakening	-	β
Tension cut-off	T_c	0

Suppose that the local components of the displacement discontinuity vector are denoted by D_y and D_z with respect to the local coordinate system shown in figure 3.1.1.1. These values are to be chosen to satisfy given traction or displacement boundary conditions on a specified side of the element. The values of D_y and D_z can be solved using an iterative technique proposed by Ryder (Ryder and Napier 1985). In this procedure the tractions at a given collocation point inside the element can be expressed as

$$\begin{bmatrix} T_y \\ T_z \end{bmatrix} = K_0 \begin{bmatrix} D_y \\ D_z \end{bmatrix} + \begin{bmatrix} E_y \\ E_z \end{bmatrix} \qquad (3.1.2.1)$$

where T_y, T_z are the traction vector components and E_y, E_z represent "external" tractions including the primitive stress field and stresses induced by other mobilized discontinuities. K_0 is the self-effect influence coefficient. Rather than iterating D_y, D_z directly, it is more convenient to perform iterative acceleration of estimates of E_y, E_z and then to solve equations (3.1.2.1) for D_y, D_z. This is particularly useful for treating friction sliding conditions. In this case the equilibrium condition is that the driving shear traction is equal to the shear resistance according to

$$-eT_y = S_0 - \tan\phi \, T_z \tag{3.1.2.2}$$

where e = indicator variable
$= +1$ if $E_y < 0$
$= -1$ if $E_y > 0$
S_0 = residual cohesion
ϕ = residual friction angle.

If it is assumed that the discontinuity opening displacement is given by

$$D_z = -\tan\psi \left| D_y \right| \tag{3.1.2.3}$$

where ψ is the sliding dilation angle, then it can be shown that at equilibrium

$$D_y = \frac{-\left[E_y + e(S_0 - \tan\phi E_z)\right]}{K_0\left[1 + \tan\phi \tan\psi\right]} \tag{3.1.2.4}$$

Other conditions of discontinuity opening (zero stress) or locking are easily accommodated by appropriate solutions of equations (3.1.2.1). Initial failure of a discontinuity is determined by the unmobilized friction and cohesion, ϕ' and S_0', which are assumed to drop immediately to the mobilized values ϕ and S_0 when failure is initiated. More elaborate relationships, including cohesion weakening and discontinuity stiffness can be treated using the external influence structure of equations (3.1.2.1).

A simple cohesion weakening model can be formulated as follows. Let the cohesion S be defined as a function of the slip component D_y such that

$$S = S_0' - \beta \left| D_y \right| \qquad (3.1.2.5)$$

where β is the cohesion weakening parameter and $S \geq S_0$ the residual cohesion. D_y can be shown to be given by a modified form of equation 3.1.2.4.

$$D_y = \frac{-\left[E_y + e(S_0' - \tan\phi E_z)\right]}{K_0\left[1 + \tan\phi \tan\psi\right] - \beta} \qquad (3.1.2.6)$$

The following logic is used to control the evaluation of the slip-weakening condition.

(i) If $\beta \geq K_0$ then cohesion falls immediately to the residual value S_0 and equation 3.1.2.4 is applied.
(ii) If $\beta < K_0$ apply equation 3.1.2.6 and check that $S \geq S_0$. If $S < S_0$ apply equation 3.1.2.4.

3.1.3 Crack Growth Rules

Work carried out under objective 2.5 of the Rockmass Behaviour project plan is reported in this section.

The dilation and slip weakening models have been described in section 3.1.2. The dilation (crack opening) is assumed to be proportional to the crack slip. Different dilation angles can be used for forward and reverse slip movements. Slip weakening is treated by postulating that the cohesion is a linear function of the slip movement such that the cohesion falls from an initial value to a residual value after a critical amount of slip movement.

Fracture propagation rules are used to determine both the direction of fracture propagation and the likelihood or propensity for fractures to propagate at a given site. Different logical processes are used to evaluate the appropriate growth direction at a given site and then to decide whether the crack will grow at the site. The growth direction logic is controlled by defining two types of growth processes, namely tension (or extension) growth ('T' type) and shear band growth ('S' type). In general, growth directions are evaluated at a number of sites which are either free-standing points in the medium where fracture has not yet initiated, or at the ends of existing crack segments or at element junctions within a crack segment. After the growth direction is determined, a measure of the growth potential is assigned to each site that has been evaluated. This measure is used to decide whether growth can occur at each site and is also used to rank the potential for growth at all specified sites. Two growth potential rules are currently permitted. These are either to allow all sites which can grow to be initiated simultaneously, or to permit growth to occur only at the site having the highest ranked growth potential.

Evaluation of the growth potential at a free-standing point in the medium is carried out by evaluating the stress tensor at that point. Define α to be the direction, with respect to some global coordinate system, of the most tensile principal stress component at the given point. (Tensile stresses are assumed to be positive). For tensile growth ('T' type), the growth direction is then chosen to be at an angle of $\alpha \pm \pi / 2$. To make the choice specific, a base angle α_0 is associated with each free-standing seed point and either the angle $\alpha + \pi / 2$ or $\alpha - \pi / 2$ which is closest to α_0 is chosen as the growth direction. The criterion for growth potential is measured as the magnitude of the most tensile principal stress component (tensile stresses are positive) or as the energy release rate that would occur if the crack was introduced. For shear growth ('S' type) the initial growth direction is chosen from four possible conjugate growth angles as the angle that is closest to α_0. The four angles are $\alpha \pm (\pi + \phi + \psi) / 4$ and $\alpha + \pi \pm (\pi + \phi + \psi) / 4$ where ϕ is the mobilized friction angle and ψ is the dilation angle. These angles are compatible with shear band theory (Vermeer and de Borst 1984).

In the case of crack initiation from the ends of existing elements, a direct search is carried out at points located a fixed distance from the element end points to determine the optimum growth direction. The local coordinate system at the crack tip is shown in figure 3.1.3.1. The stress tensor is examined at points Q which are located at a fixed distance ρ from the element end point P. The points C_1 and C_2 in the existing element represent the collocation positions at which boundary condition values are matched within the element. Two such points exist within each linear variation displacement discontinuity element. In practice, it has been found to be satisfactory to set the search radius ρ equal to the distance between the crack tip P and the adjacent collocation position of the proposed element, Q (figure 3.1.3.1). Define a local system of coordinate axes r and θ that are parallel and normal to the direction PQ

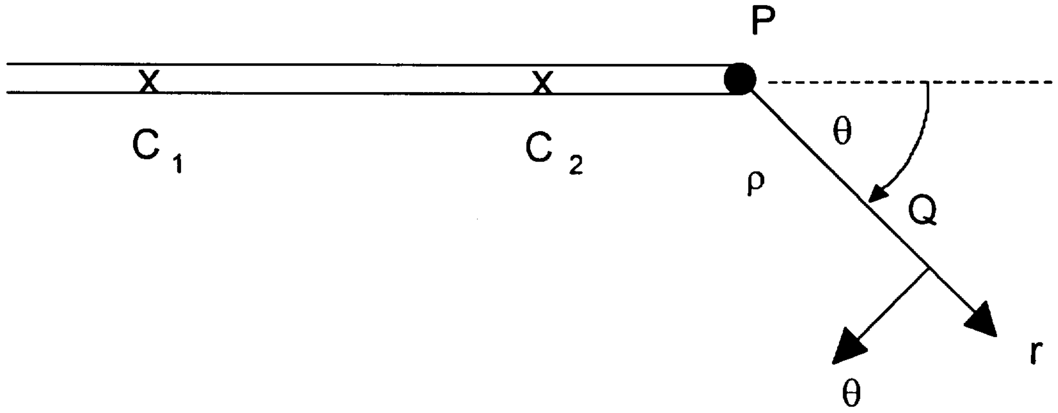

Figure 3.1.3.1 Local crack tip coordinate system.

respectively as shown in figure 3.1.3.1. Tension ('T' type) crack growth is controlled by choosing the angle θ for which the circumferential component $\tau_{\theta\theta}$ is a maximum (Napier and Hildyard 1992). Tensile stress is assumed to be positive. The criterion for growth potential is measured as the magnitude of the most tensile principal stress component or as the energy release rate that would occur with the proposed crack extension.

In the case of growing tensile fractures, it might be argued that the growth potential should be measured by the stress intensity factor at the crack tip. No difficulty would be introduced into the DIGS computational procedure by using special crack tip shape functions to describe the crack sliding and opening mode components, $i = y$ and $i = z$ respectively, by functions of the following form.

$$D_i(\xi) = k_i \xi^{\frac{1}{2}} (1 + m_i \xi) \qquad (3.1.3.1)$$

where ξ is the distance from the crack tip and k_i and m_i are constants. It can be shown that the in-plane stress intensity factors are related to the coefficients k_i by

$$K_i = -\left[\frac{G}{2(1-\nu)}\sqrt{\pi/2}\right]k_i \tag{3.1.3.2}$$

where G is the shear modulus and ν is Poisson's ratio. (It should be noted that, from the definition of the displacement discontinuity, equation 3.1.1.1, k_z is negative if the crack tip opens).

In the DIGS code a direct search is carried out ahead of each crack tip and special crack tip elements are not used. In addition, it is not clear that the functional form of equation 3.1.3.1 has any relevance in the growth of shear band structures. Provided that the search radius ρ is equal to the distance from the current crack to the collocation point of the proposed element, stress-based failure surfaces such as the Mohr-Coulomb or Hoek-Brown criteria, can be applied directly to measure the fracture growth propensity. If necessary, stress intensity factors can be estimated by computing the energy release rate at the crack tip by using the following procedure. Napier (1991) has shown that the incremental energy release on a specified fracture surface S_d is given by

$$\Delta W_A = -\tfrac{1}{2}\int_{S_d}\left[T_i^p(Q)+T_i^t(Q)\right]\left[D_i^t(Q)-D_i^p(Q)\right]dS_Q \tag{3.1.3.3}$$

where S_d = total crack surface including crack extensions,

T_i^p = Crack surface traction vector components prior to the crack extension,

T_i^t = Crack surface traction vector components after the crack extension,

D_i^p = Displacement discontinuity vector components prior to crack extension,

D_i^t = Displacement discontinuity vector components after crack extension.

In practice, it is found that equation 3.1.3.3 can be evaluated accurately for each element using the traction and displacement discontinuity vector components at the element collocation points in the following sum.

$$\Delta W_A^{el} \approx -\tfrac{b}{2} \sum_{\varepsilon=\pm 1} \left[T_i^p(\varepsilon c) + T_i^t(\varepsilon c) \right] \left[D_i^t(\varepsilon c) - D_i^p(\varepsilon c) \right] \qquad (3.1.3.4)$$

where c is the distance from the centre of the element to each collocation point and b is the half-length of the element.

To illustrate the application of equation 3.1.3.4 consider, for example, a straight crack of half-length $a = 100\text{m}$ that is modelled using twenty elements of length 10m in a tensile stress field of 100 MPa perpendicular to the crack. The computed crack opening discontinuity and the stress ahead of one of the edge crack elements are given in Table 3.1.3.1.

Table 3.1.3.1 Displacement discontinuity values and stresses adjacent to the edge of a tensile crack modelled with twenty elements (E = 70000MPa, ν = 0,2).

Position relative to centre of last element ($c = 2,5\sqrt{2}\,\text{m}$)	Displacement discintinuity (m)	Stress(MPa)
-c	-0,2196	0
+c	-0,1047	0
10-c	0	659,3
10+c	0	258,7

In the case of an open crack, equation 3.1.3.3 assumes the special form

$$\Delta W_A = -\tfrac{1}{2} \int_{\Delta S_d} T_i^p(Q) D_i^t(Q) dS_Q \qquad (3.1.3.5)$$

where ΔS_d is crack extension surface. Using the displacement discontinuity values and stress components given in Table 3.1.3.1, equation 3.1.3.5 can be evaluated approximately, using 3.1.3.4, to yield the energy release rate

$$\hat{G} = \Delta W_A / \Delta S_d \approx -\tfrac{1}{4}[-0,2196(659,3) - 0,1047(258,7)]$$
$$\hat{G} \approx 42,96 \text{ MJ/m}$$

From fracture mechanics theory, the value for G in plane strain is

$$\mathsf{G} = \frac{(1-\nu)K_I^2}{2G} \qquad (3.1.3.6)$$

For a straight crack of half-length a and normal to a tensile stress field σ it is well known that (Lawn and Wilshaw, 1975)

$$K_I = \sqrt{\pi a}\,\sigma \qquad (3.1.3.7)$$

Using the values $a = 100\text{m}$, $\sigma = 100\,\text{MPa}$, $E = 70000\,\text{MPa}$, and $\nu = 0{,}2$ it can be shown that G=43,08 MJ/m which is in very good agreement with the value for $\hat{\mathsf{G}}$. Although it is possible to estimate stress intensity factor values for a growing crack, it is apparent that energy release calculations can be carried out in a straightforward manner and consequently it is proposed that the energy release rate should form a uniform basis for determining the growth potential of a given crack. The criterion for determining whether a crack will grow can be formulated as $\mathsf{G} \geq \mathsf{G}_C$ where G_C is a material property representing representing the critical energy required for crack initiation or growth.

The energy release approach can be used to formulate growth rules for the formation of shear band structures (type 'S'). Strictly, all possible crack extension increments should be introduced explicitly and the entire problem re-solved to compute the released energy computed in each case. This would have to be repeated at all growth sites and would result in a prohibitive computational effort. It is, however, possible to estimate the energy release in a proposed growth direction as follows. From equation 3.1.3.3, the energy release per unit area of crack extension is

$$\mathsf{G} \approx \Delta W_A / \Delta S_d = -\frac{1}{2\Delta S_d}\int_{\Delta S_d}\left[T_i^p(Q) + T_i^t(Q)\right]\left[D_i^t(Q) - D_i^p(Q)\right]dS_Q \qquad (3.1.3.8)$$

where ΔS_d is the area of the crack tip extension and T_i and D_i represent the traction and displacement discontinuity components before and after the introduction of the crack extension area as defined previously. Since it is presumed that no fracture exists in the prior state,

$D_i^p = 0$. In solving for the crack movements, assume that the proposed element has a local coordinate system y-z with the y-axis tangent to the proposed element and the z-axis normal to the new element. The crack slip and opening movements D_y^t and D_z^t can be deduced from the stress equilibrium relationships given in section 3.1.2.

$$T_y^t = K_0 D_y^t + E_y \tag{3.1.3.9}$$

$$T_Z^t = K_0 D_Z^t + E_Z \tag{3.1.3.10}$$

$$-eT_y^t = S_0 - \tan\phi\, T_z^t \tag{3.1.3.11}$$

$$D_z^t = -\tan\phi \left|D_y^t\right| \tag{3.1.3.12}$$

where K_0 = self-effect influence at proposed collocation point,
E_y = external shear traction,
E_z = external normal traction,
S_0 = residual cohesion,
ϕ = mobilized friction angle,
ψ = dilation angle,
e = slip direction indicator variable ($e = +1$ if $E_y < 0$; $e = -1$ if $E_y > 0$)

From equations 3.1.3.9 to 3.1.3.12 it can be shown that for sliding equilibrium

$$D_y^t = \frac{-\left[E_y + e(S_0 - \tan\phi E_z)\right]}{K_0\left[1 + \tan\phi \tan\psi\right]} \tag{3.1.3.13}$$

The energy release rate can be approximated by the sum

$$\mathrm{G} \approx -\tfrac{1}{2}(E_y + T_y^t)D_y^t - \tfrac{1}{2}(E_z + T_z^t) \tag{3.1.3.14}$$

where it is asssumed that

$$E_y \approx T_y^p \tag{3.1.3.15}$$

and $$E_z \approx T_z^p \tag{3.1.3.16}$$

The nature of the approximation lies in the fact that the external stresses E_y and E_z are determined *before* the new element is allowed to interact with the existing elements in the system. The stress terms in equation 3.1.3.14 can be reduced to functions of D_y^t by employing equations 3.1.3.9, 3.1.3.10 and 3.1.3.12. D_y^t is itself given by equation 3.1.3.13 which contains known quantities. In the particular case where the angle of dilation, ψ, and the residual cohesion, S_0, are zero, it can be seen from equation 3.1.3.13 that $K_0 D_y^t = -E_y + e\tan\phi E_z$. From equation 3.1.3.12 $D_z^t = 0$ since the dilation angle is zero and hence, equation 3.1.3.14 becomes

$$\mathrm{G}_S = \left[E_y^2 - \tan^2\phi\ E_z^2\right] / 2K_0 \tag{3.1.3.17}$$

The subscript S in equation 3.1.3.17 is used to designate shear band energy release and it is assumed that the discontinuity is in a state of compression normal to the discontinuity surface ($T_z^t < 0$). If the crack opens, the tractions T_i^t become zero and from equations 3.1.3.9 and 3.1.3.10,

$$D_y^t = -E_y / K_0 \tag{3.1.3.18}$$

$$D_z^t = -E_z / K_0 \tag{3.1.3.19}$$

Substituting these expressions into equation 3.1.3.14, the energy release rate for an opening crack becomes

$$\mathrm{G}_T = \left[E_y^2 + E_z^2\right] / 2K_0 \tag{3.1.3.20}$$

The subscript T in equation 3.1.3.20 designates energy release in tension or opening mode. These relationships provide the basis for a uniform treatment of the growth potential of fractures in tension or in shear. In shear mode, G is evaluated using equation 3.1.3.14 with the aid of equation 3.1.3.13 and the growth direction is chosen to maximize G_S. The growth potential is assigned a value $G_S - G_{Sc}$ where G_{Sc} is the appropriate critical shear energy for the material. Similarly for tensile mode failure, G_T is evaluated using equation 3.1.3.20 and the growth direction is chosen to maximize $G_T - G_{Tc}$ where G_{Tc} is the critical energy for tensile fracture. Values of G_{Sc} and G_{Tc} have to be calibrated for particular materials.

3.1.4 Solution of Large-Scale Problems.

This section describes work carried out under project plan objective 2.6. In general, the elements in a crack simulation problem are irregularly positioned in space and an appropriate influence coefficient must be stored for every sending/receiving combination. This implies that for a problem with N elements the influence storage space is proportional to N^2 and, in an iterative scheme, the cost of each iteration is proportional to N^2. This problem of dimensionality can be reduced if the elements are located on a regular grid mesh. Since the influence function depends only on the relative distance between elements, the influence computation can be considered to be a convolution operation that admits evaluation using the Discrete Fourier Transform (DFT) (Peirce *et al* 1992). This requires influence coefficient storage space proportional to N rather than N^2 and the influence computation cost for each iteration is proportional to $N \log N$.

The present problem can be cast into this form (Napier and Peirce 1995) by noting that the biharmonic potential function Ψ can be written in terms of the field point coordinates p_i and q_i in the form

$$\Psi(p_i - q_i) = \Psi(p_i - q_i^0 + q_i^0 - q_i) \qquad (3.1.4.1)$$

where q_i^0 is chosen as a "regular" mesh point that is "close" to q_i. Equation 3.1.4.1 can be expanded in a Taylor series

$$\begin{aligned}\Psi(p_i - q_i) = {} & \Psi^0 + (q_i^0 - q_i)\Psi_{,i}^0 \\ & + \tfrac{1}{2}(q_i^0 - q_i)(q_j^0 - q_j)\Psi_{,ij}^0 + \dots\end{aligned}$$

where $\Psi^0_{,i} \equiv \frac{\partial}{\partial p_i}\Psi(p_i - q_i^0)$. Hence, designating the distance between p and q^0 as r^0, equation 3.1.1.8 becomes

$$\int \Psi(r)\Delta_{rs}d\eta = \Psi(r^0)M^0_{rs} + \Psi_{,i}(r^0)M^i_{rs} + \Psi_{,ij}(r^0)M^{ij}_{rs} + \ldots \qquad (3.1.4.2)$$

where the multipole strain moments $M^{ij\cdots}_{rs}$ are defined by

$$\begin{aligned} M^0_{rs} &= \int \Delta_{rs}d\eta \\ M^i_{rs} &= \int (q_i^0 - q_i)\Delta_{rs}d\eta \\ M^{ij}_{rs} &= \int (q_i^0 - q_i)(q_j^0 - q_j)\Delta_{rs}d\eta \quad \text{etc.} \end{aligned} \qquad (3.1.4.3)$$

Hence by choosing a regular array of points q_i^0 to be at the centres of rectangular cells, it is possible to expand all discontinuity elements that intersect these cells in terms of the multipole strain moments defined by equations 3.1.4.3. Influences are determined in terms of the derivatives of the potential function $\Psi(r^0)$ and can be computed using a suitable DFT scheme. In practice it is found that the accuracy of the multipole expansion is adequate if third order moments are included but deteriorates when the sending cell centre q^0 becomes closer than three or four cell units from the receiving point p. This difficulty is overcome by setting up square clusters of receiving grid cells in pre-defined positions. A pad region is defined to surround each cluster. All multipole influences originating within the pad region are subtracted from the multipole influences computed from the DFT convolution and are replaced by influences computed directly from the actual element configurations within the pad region.

This scheme allows for large scale irregular geometries to be analysed efficiently in terms of remote influences while retaining necessary accuracy with respect to detailed local geometrical configurations. It must be appreciated also that the scheme proposed here allows sending influences to arise from either displacement discontinuities or from plastic volume elements. This provides the opportunity to combine individual discontinuities, plastic regions or regions represented by suitable damage models within the same numerical scheme.

The efficiency of the multipole method has been evaluated by running a series of test problems comprising different numbers of parallel cracks (Peirce and Napier 1995). These problems were solved initially by direct computation of influences between each sending/ receiving point, and then solved again using a suitable multipole grid to compute the inter-element influences. It was found that the multipole scheme ran faster than the direct influence computation method if the number of elements exceeded 700. It was confirmed that the run times of the multipole method increased approximately in proportion to the number of elements whereas the the run times of the direct influence method were proportional to the square of the number of elements, for a fixed number of iterative cycles. The multipole method was found to require about 16 MBytes of main memory for every 1000 elements.

Although the multipole method has achieved a marked break-through for the solution of any given problem comprising several thousand elements, it must still be appreciated that the effective solution of multiple step crack growth problems remains a major challenge. Therefore, an additional break-through is required to enable the efficient simulation of stope scale multistep mining problems comprising of the order of 100 000 elements.

3.1.5 Solution of Multiple Material Problems

Project plan objectives 2.7 and 2.8 are formulated to address problems of multiple material modelling.

In some cases it will be of interest to model differences in the elastic properties of the rock mass. This can arise both at the rock fabric level where variable grain and matrix properties may lead to local stress concentrations and at a stope scale level of detail, where regional variations in rock modulus may be important. A clear distinction must be drawn in all cases between differences in the rock elastic properties and variations in the strength of the rockmass, depending on the rock type.

In order to model multiple material regions in DIGS it is necessary to formulate additional relationships that must be defined at the interface between two regions. These conditions depend on the specific boundary condition that is to be satisfied at the interface. In general, four relationships must be satisfied at the interfaces of two-dimensional problems. These relate to the normal and tangential components of the displacement and traction vectors at each point of the interface. In order to satisfy these interface constraints it is necessary to superimpose two layers of displacement discontinuity elements along each interface. Figure 3.1.5.1 depicts such an interface separating regions **a** and **b** and having a local coordinate axis y parallel to the interface and axis z normal to the interface. This formulation is essentially equivalent to that given by Crouch and Starfield, 1983, except that in the present case displacement discontinuity elements are used instead of so-called force discontinuity elements. Displacement discontinuity elements are more appropriate if crack growth from interfaces is to be permitted.

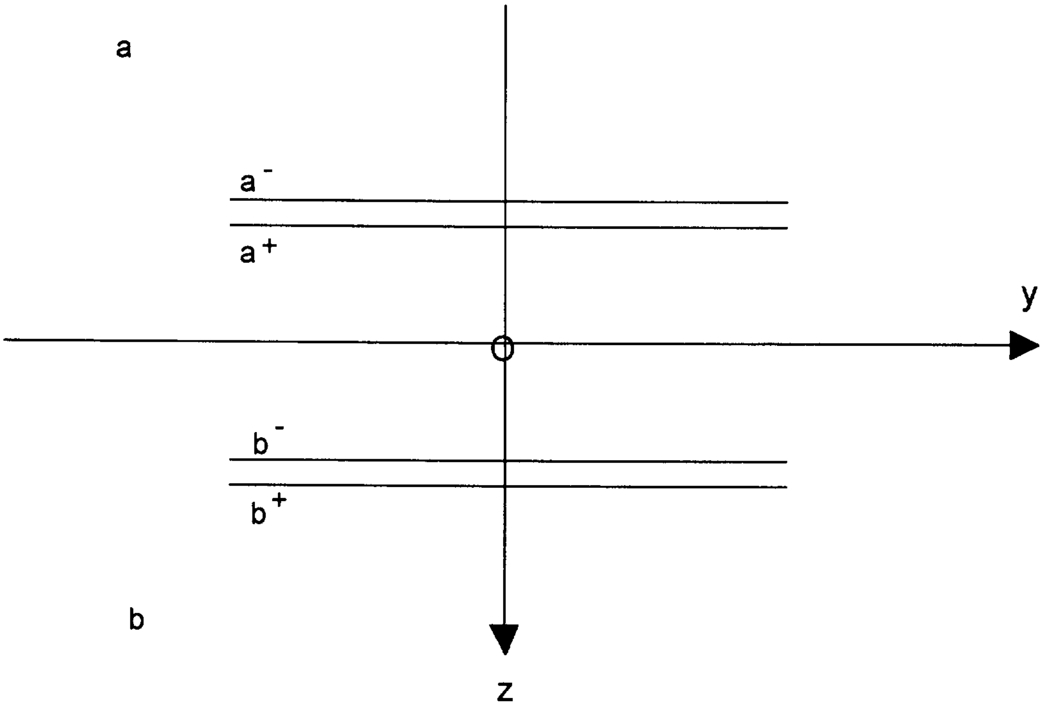

Figure 3.1.5.1 Double element scheme for modelling multiple material interfaces.

Let the unknown components of the displacement discontinuity vectors in the adjacent elements **a** and **b** be designated as D_y^a , D_z^a and D_y^b , D_z^b respectively. For a bonded interface, the following conditions must be satisfied by the displacement vector components.

$$u_y^{a-} = u_y^{b+} \tag{3.1.5.1}$$

$$u_z^{a-} = u_z^{b+} \tag{3.1.5.2}$$

Similarly, the traction vector components must satisfy the conditions

$$T_y^a = T_y^b \tag{3.1.5.3}$$

$$T_z^a = T_z^b \tag{3.1.5.4}$$

Designating the "external" displacement influence components at the point of interest Q by the quantities $F_y^a, F_y^b, F_z^a, F_z^b$ the total displacement components on the outer sides of the double element can be wtitten in the form

$$u_y^{a-} = \tfrac{1}{2} D_y^a + F_y^a \tag{3.1.5.5}$$

$$u_z^{a-} = \tfrac{1}{2} D_z^a + F_z^a \tag{3.1.5.6}$$

$$u_y^{b+} = -\tfrac{1}{2} D_y^b + F_y^b \tag{3.1.5.7}$$

$$u_z^{b+} = -\tfrac{1}{2} D_z^b + F_z^b \tag{3.1.5.8}$$

Similarly, if $E_y^a, E_y^b, E_z^a, E_z^b$ designate the external traction influences, the total traction components at point Q can be expressed as

$$T_y^a = K_a D_y^a + E_y^a \tag{3.1.5.9}$$

$$T_z^a = K_a D_z^a + E_z^a \tag{3.1.5.10}$$

$$T_y^b = K_b D_y^b + E_y^b \tag{3.1.5.11}$$

$$T_y^b = K_b D_y^b + E_y^b \tag{3.1.5.12}$$

where K_a and K_b are the traction kernel self-effects for regions **a** and **b** respectively. Substituting equations 3.1.5.5 to 3.1.5.12 into the constraints 3.1.5.1 to 3.1.5.4, it can be shown that the unknown displacement discontinuities are given by

$$\begin{bmatrix} D_y^a \\ D_z^a \\ D_y^b \\ D_z^b \end{bmatrix} = \frac{1}{K_a + K_b} \begin{bmatrix} K_b & 0 & 1 & 0 \\ 0 & K_b & 0 & 1 \\ K_a & 0 & -1 & 0 \\ 0 & K_a & 0 & -1 \end{bmatrix} \begin{bmatrix} 2(F_y^b - F_y^a) \\ 2(F_z^b - F_z^a) \\ E_y^b - E_y^a \\ E_z^b - E_z^a \end{bmatrix} \tag{3.1.5.13}$$

The conditions $K_a = 0$ or $K_b = 0$ imply that either region **a** or region **b** is open. The bonded interface behaviour can be illustrated by considering the uniaxial loading of a rectangular block containing two circular inclusions which are aligned with the loading direction. Figure 3.1.5.2 shows the exaggerated distortion of the block, following the application of the load, for the case when the two inclusions have a lower modulus (50000MPa) than the surrounding material in the block (90000MPa). The inclusions can be seen be seen to be deformed in a similar manner to two circular openings. If the relative moduli are reversed, with the included regions being harder than the surrounding material, the distorted deformation pattern shown in figure 3.1.5.3 results.

Additional constitutive models for interface sliding can be formulated in a similar manner to equation 3.1.5.13 but detailed explorations of these possibilities have not been carried out at the present time. In the case of bonded inhomogeneities it is found that the main stress changes are most noticeable near the material interfaces. This phenomenon deserves further exploration in relation to the evaluation of dyke failure mechanisms.

With respect to the project output 2.8, a suitable iterative scheme has been included to allow efficient solution of multiple material problems.

3.1.6 Fracture propagation as a result of fluid pressure

Simulation of fracture growth as a result of blasting, hydraulic fracturing or fluid injection requires the calculation of the fluid pressure within the fractures. Much work has been done for hydraulic fracturing simulation in the oil industry using boundary element (Lam and Cleary 1988) and finite element (Boone and Ingraffea 1990) techniques. The consideration of fracture growth due to the penetration of blast gases is more complex as gas is compressible, and heat and seepage losses along cracks are significant and requires the solution of coupled elasticity, fluid flow and heat transfer equations (Nilson et al. 1985). Semi-analytical solutions can be obtained for simple situations such as the propagation of planar cracks from a borehole. Modelling of two-dimensional fracture growth in a non-uniform stress state can be achieved using boundary element techniques to solve for the stresses around the fracture and a partially coupled finite difference mesh to solve the fluid flow and heat transfer equations (Christianson et al. 1988).

As part of objective 2.10, a simple scheme for simulating fluid driven fracture propagation in two-dimensions has been implemented into the DIGS code. The method is based on the technique proposed by Swenson and Taylor (1983) for blast stimulation of oil wells. The pressure decay function in the borehole is defined explicitly. A constant value of gas pressure

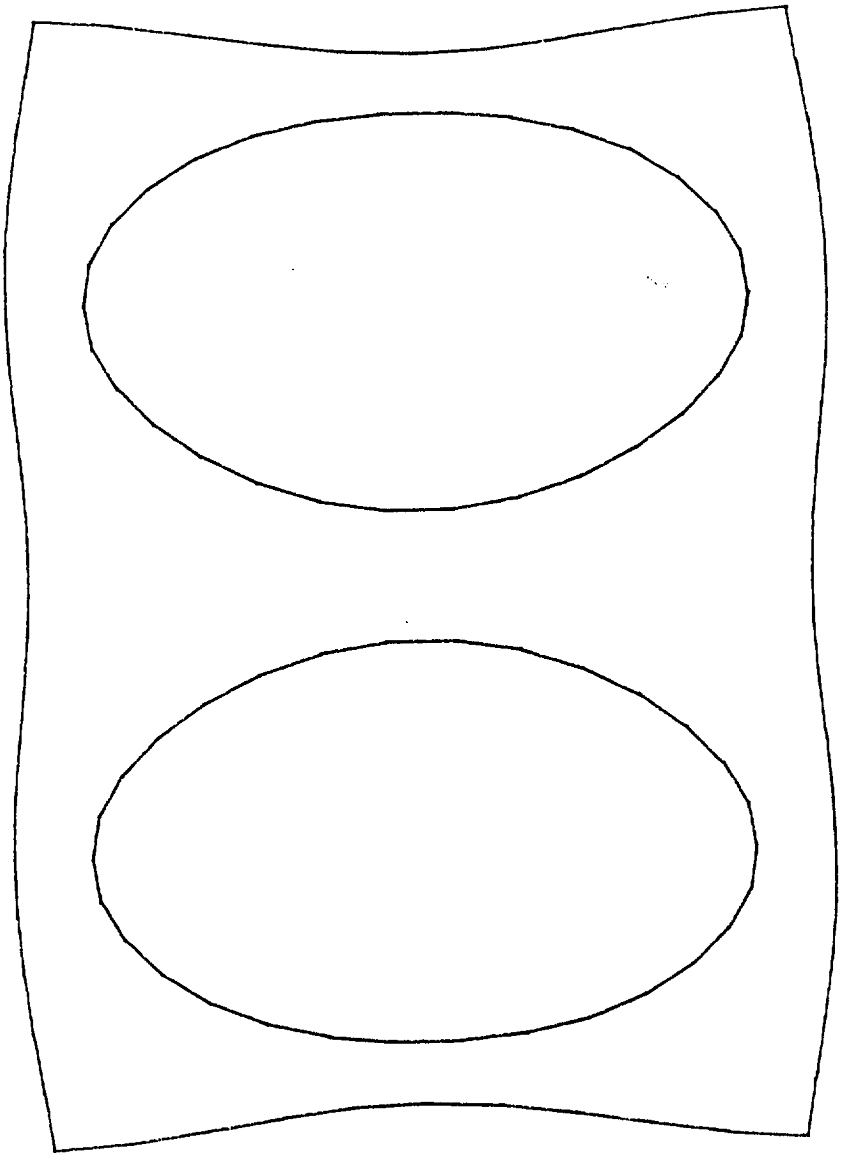

Figure 3.1.5.2 Deformation of a uniaxially loaded rectangular block containing two soft inclusions.

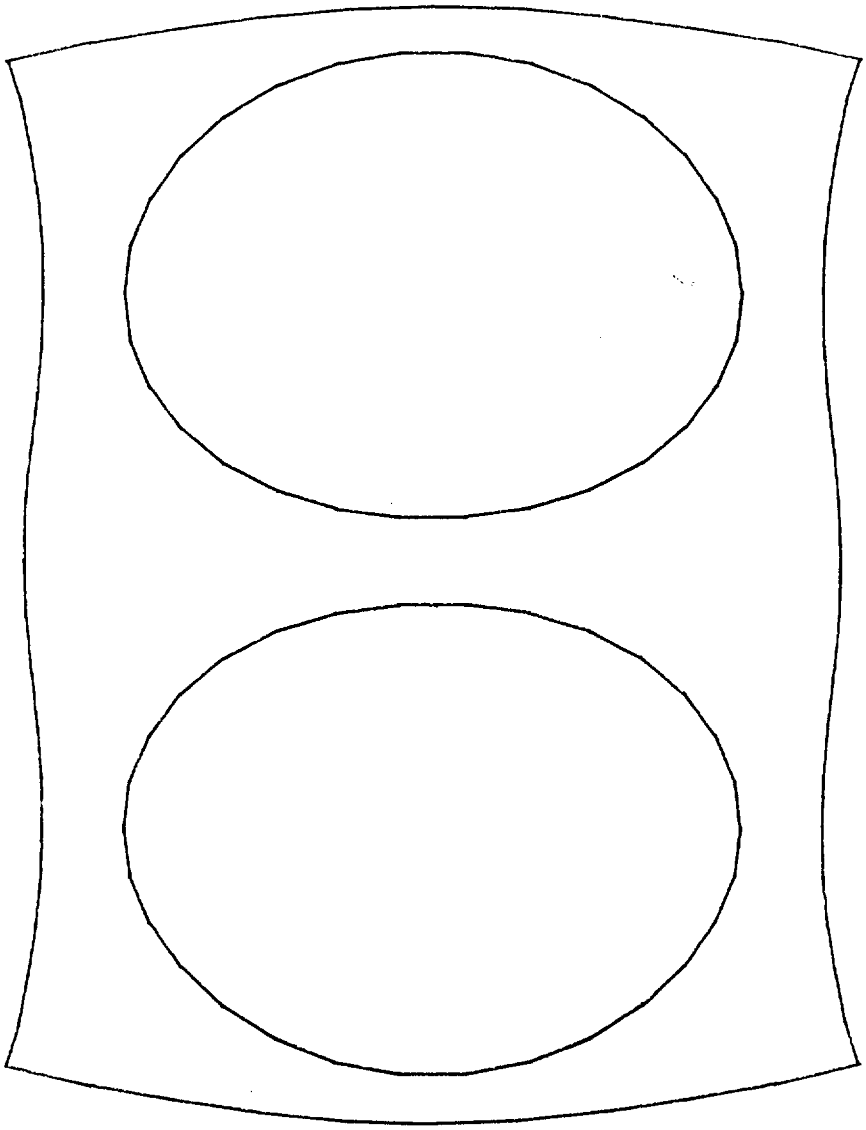

Figure 3.1.5.3 Deformation of a uniaxially loaded rectangular block containing two hard inclusions.

is applied as a pore pressure to the displacement discontinuity elements and is assumed to act over a specified fraction of the crack length. Thus, the gas is assumed to flow instantaneously into the fracture, at a pressure which is lower than the borehole pressure. The incremental solution procedure of DIGS is modified into a time-stepping scheme. The time increment is calculated by dividing the assumed crack increment length by the terminal velocity of the crack growth (Bieniawski, 1967).

Simulation of borehole blasting experiments suggest that the crack extends much further when the blast pressure is taken into account. The addition of a free surface to simulate a bench blast causes fractures to initate from seeds adjacent to the borehole. These will extend into the hangingwall if the pressure is sufficiently large and extends over a significant proportion of the crack length.

The simple model described above has shown that much of the blast fracture growth is due to the quasi-static gas pressure as opposed to the dynamic effects of the blast wave. A more realistic fluid pressure model is planned to be implemented into the DIGS program as a first step towards the ultimate aim of adressing the growth of gas and fluid filled fractures in three-dimensions.

3.1.7 Three-dimensional Fracture Modelling

This topic is covered by the project plan objective 2.11.

The solution of arbitrarily oriented and intersecting cracks in three dimensions presents a number of special problems relating to the element mesh shape that is used to cover the crack surface. For solution run-time efficiency, it is generally desirable to cover the crack surface with regular polygons such as squares, equilateral triangles, or hexagons. Clearly, these regular meshes preclude the modelling of arbitrarily oriented planar intersections. Thus it is necessary to employ irregular sided polygonal elements near the junctions between intersecting cracks, where the regular mesh can be distorted appropriately. If automatic mesh generation facilities are used, such as Delaunay triangulation schemes, it is desirable to use arbitrarily shaped triangles to cover the crack surface.

Consider a trapezoidal region, A, defined in the x-y plane as shown in figure 3.1.7.1 It has been demonstrated (see for example, Crouch and Starfield, 1983) that the displacement and stress field induced at point $P(x, y, z)$ by a constant displacement discontinuity vector over the region A, can be expressed in terms of the derivatives with respect to x, y, and z of the potential integral

$$I(P) = \int_A \frac{1}{r} dS_Q \tag{3.1.7.1}$$

where $r = |P - Q|$ and dS_Q is an elementary area at point Q inside A. For a general polygon, comprising N sides, the total potential, E, at point $P(x, y, z)$ can be evaluated by summing expressions corresponding to equation 3.1.7.1 for each side. In particular, it can be shown that

$$E(x,y,z) = \sum_{k=1}^{N} \left[I(A_{k+1}, B_k, m_k, z) - I(A_k, B_k, m_k, z) \right] \tag{3.1.7.2}$$

where side k is considered to extend between x_k and x_{k+1} and to have a slope m_k and an intercept c_k (Sides parallel to the y axis are skipped in the sum). In addition,

$$A_k = x - x_k \tag{3.1.7.3}$$

$$B_k = y - m_k x - c_k \tag{3.1.7.4}$$

Define also the following quantities.

$$R^2 = A^2 + (B - m A)^2 + z^2 \tag{3.1.7.5}$$

$$w = B + mA + R \tag{3.1.7.6}$$

$$L = (1 + m^2) w - B + (A + mw)\sqrt{1 + m^2} \tag{3.1.7.7}$$

Using equations 3.1.7.5 to 3.1.7.7, the potential I can be expressed most conveniently in terms of the following first derivative expressions

$$I_{,y} = \frac{1}{\sqrt{1 + m^2}} \log L \tag{3.1.7.8}$$

$$I_{,x} = \log w - mI_{y} \tag{3.1.7.9}$$

$$I_{,z} = -\tan^{-1}\left\{\frac{(A+mw)B}{z\left[R+m(A+mw)\right]}\right\} + \tan^{-1}\left\{\frac{A+mw}{z}\right\} \tag{3.1.7.10}$$

It should be noted from the properties of the arctan function in eqation 3.1.7.10 that $lim|_{z \to \pm 0}$ $E_{,z} = \mp 2\pi$ if $(x,y) \in$ Interior of A, and $lim|_{z \to 0}$ $E_{,z} = 0$ if $(x, y) \notin$ A. Particular expressions for the displacement and stress field components u_i and τ_{ij}, respectively, at the field point P, can be recovered in terms of the first to third order derivatives of E. These expressions are given in component form as follows.

$$\begin{bmatrix} u_x \\ u_y \\ u_z \end{bmatrix} = \frac{1}{8\pi(1-\nu)} \begin{bmatrix} 2(1-\nu)E_{,z} - zE_{,xx} & -zE_{,xy} & -(1-2\nu)E_{,x} - zE_{,xz} \\ -zE_{,xy} & 2(1-\nu)E_{,z} - zE_{,yy} & -(1-2\nu)E_{,y} - zE_{,yz} \\ (1-2\nu)E_{,x} - zE_{,xz} & (1-2\nu)E_{,y} - zE_{,yz} & 2(1-\nu)E_{,z} - zE_{,zz} \end{bmatrix} \begin{bmatrix} D_x \\ D_y \\ D_z \end{bmatrix} \tag{3.1.7.11}$$

and

$$\begin{bmatrix} \tau_{xx} \\ \tau_{yy} \\ \tau_{zz} \\ \tau_{yz} \\ \tau_{zx} \\ \tau_{xy} \end{bmatrix} = \frac{G}{4\pi(1-\nu)} \begin{bmatrix} 2E_{,xz} - zE_{,xxx} & 2\nu E_{,yz} - zE_{,xxy} & -E_{,xx} - 2\nu E_{,yy} - zE_{,xxz} \\ 2\nu E_{,xz} - zE_{,xyy} & 2E_{,yz} - zE_{,yyy} & -E_{,yy} - 2\nu E_{,xx} - zE_{,yyz} \\ -zE_{,xzz} & -zE_{,yzz} & 2E_{,zz} - zE_{,zzz} \\ -\nu E_{,xy} - zE_{,xyz} & E_{,zz} + \nu E_{,xx} - zE_{,yyz} & -zE_{,yzz} \\ E_{,zz} + \nu E_{,yy} - zE_{,xxz} & -\nu E_{,xy} - zE_{,xyz} & -zE_{,xzz} \\ (1-\nu)E_{,yz} - zE_{,xxy} & (1-\nu)E_{,xz} - zE_{,xyy} & -(1-2\nu)E_{,xy} - zE_{,xyz} \end{bmatrix} \begin{bmatrix} D_x \\ D_y \\ D_z \end{bmatrix} \tag{3.1.7.12}$$

G and ν are the shear modulus and Poisson's ratio respectively and subscripts on E designate derivatives with respect to the indicated directions ($E_{,x} \equiv \partial E / \partial x$ etc.).

It is important to note certain consequences of assigning a constant displacement discontinuity shape function over the element. When $z \to 0$, the stress components, τ_{ij} at point P become singular when P falls on the edge of the element and it is not possible to determine the average value of $\tau_{ij}(P)$ over the area of the element, A. $\tau_{ij}(P)$ must therefore be interpreted as representing a measure of the average value of the stress in the element. In formulating a numerical solution procedure, a suitable point P must be chosen within each element. One natural choice is the centroidal position, given by coordinates

$$\begin{aligned}\bar{x}_P &= \frac{1}{N}\sum_{k=1}^{N} x_k \\ \bar{y}_P &= \frac{1}{N}\sum_{k=1}^{N} y_k\end{aligned} \tag{3.1.7.13}$$

It should be noted that the value of the stress components at the centroid are generally different from the extremum possible values within the element. This deviation is most pronounced for elements with large aspect ratios exceeding four or five. For aspect ratios below two, there is little difference between the extremum stresses and the stresses at the centroid. As an empirical rule of thumb, it is suggested that, unless a higher order displacement discontinuity variation is used, triangular element angles should be constrained to lie within 20° and 90°.

The accuracy of a triangular grid covering scheme was assessed for the case of normal loading applied to the surfaces of a circular crack. Figure 3.1.7.2 shows an approximately circular region divided into 60 triangular elements. The nominal diameter of the region is 30m and covers an area of 698,8 m^2 compared to the corresponding circular area of 706 m^2.

For far field loading perpendicular to the crack surface, the theoretical crack opening displacement, D_z, at point x,y is given by (Salamon, 1964):

$$D_z(x,y) = \frac{4(1-\nu)q_z}{\pi G}(R^2 - x^2 - y^2)^{\frac{1}{2}} \tag{3.1.7.14}$$

where q_z is the far field stress loading normal to the crack surface and R is the radius of the crack. From equation 3.1.7.14, the "volume" of crack opening displacement is given by

$$V_z = \frac{8(1-\nu)q_z}{3G}R^3 \tag{3.1.7.15}$$

Using a value of $G = 29166{,}7$ MPa, $\nu = 0{,}2$ and $q_z = 100$ MPa it is found that when R is set to give an area equal to that of figure 3.1.7.2, the theoretical closure volume is $V_z = 24{,}27\,m^3$.

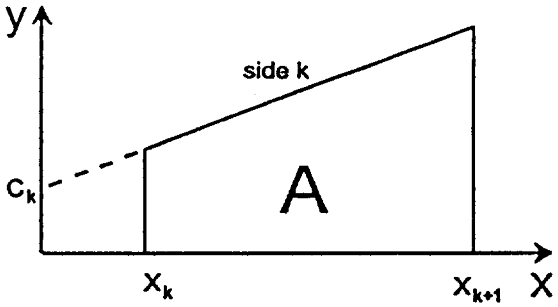

Figure 3.1.7.1 Trapezoidal region for formulation of polygonal 3D elements.

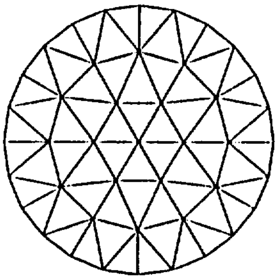

Figure 3.1.7.2 Triangular element division of circular crack.

Dividing each triangle shown in figure 3.1.7.2 into finer sub-triangles, the overall volume of closure is found to decrease slowly towards the theoretical value of 24,27 m^3. The particular values are reported in Table 3.1.7.1.

No of elements	Opening volume	% error
60	29,14	20,1
240	26,64	9,8
540	25,82	6,4
960	25,42	4,7
1500	25,20	3,8

Table 3.1.7.1 Accuracy of numerically determined crack opening volume for a circular crack covered by different numbers of triangular elements.

It appears from Table 3.1.7.1 that when 60 triangles are used, the volume of crack opening displacement is over-estimated by about 20 percent. It is also seen that the percentage error decreases very slowly as the number of triangles is increased. It has been demonstrated previously (Ryder and Napier, 1985), using square elements, that this error behaviour is related to the singular stress near the periphery of the crack opening. It was found heuristically that if the opening was reduced by one quarter of the element grid size, the crack opening displacement matched the theoretical profile very closely. This rule was found to be robust for a wide range of grid sizes. In order to deduce a similar rule for triangular elements, define the equivalent grid size $\bar{g}$ for equilateral triangular elements by

$$\bar{g} = (4A_T / \sqrt{3})^{\frac{1}{2}} \qquad (3.1.7.16)$$

where $A_T = A / N_T$ is the average area of each triangle,

A = total area of the crack surface,

N_T = total number of triangles.

It is postulated that the crack surface is shrunk by an amount $\beta\bar{g}$ where β is a constant between 0 and 1. The adjusted radius R_a is given by

$$R_a = R - \beta\bar{g} \qquad (3.1.7.17)$$

Using a series of values of β it is found that for the 60 triangle geometry shown in figure 3.1.7.2, the value $\beta = 0,173$ yields both crack opening profiles and a crack opening volume very close to the theoretical values. The stability of the β factor was tested for several tessellation densities and the results are summarized in Table 3.1.7.2.

Number of triangles	Grid size $\bar{g}$ (m)	Radius change, $\beta\bar{g}$	New radius (m)	Opening volume (m^3)
60	5,19	0,90	14,10	24,23
240	2,59	0,45	14,55	24,33
540	1,73	0,30	14,70	24,32
960	1,30	0,23	14,77	24,34
1500	1,08	0,19	14,81	24,24

Table 3.1.7.2 Application of correction factor β to determine the crack opening displacement of a circular crack.

The values in the right hand column agree very well with the theoretical crack opening volume of 24,27 m^3.

It is planned to develop the three-dimensional discontinuity modelling capabilities further to allow linked linear-variation elements to be employed and to simulate the growth of fractures in three dimensions.

CONCLUSIONS

A general description has been given of the technical basis underlying the formulation of the DIGS code. This includes the treatment of sliding cracks with friction, dilation and slip-weakening and a discussion of the rules used to control fracture growth simulation. Extensions to the DIGS framework for the solution of large-scale problems, multiple material problems and simple fluid flow logic are described. Finally, an outline is given of the formulation of three-dimensional polygonal elements. This will form the basis for future work in the simulation of three-dimension fracture growth.

REFERENCES

Bienawski, Z.T. (1967) Mechanism of brittle fracture of rock, *Int. J. Rock. Mech Min Sci*, Vol 4, 395-406.

Boone, T., Ingraffea, A. (1990) A numerical procedure for stimulation of hydraulically-driven fracture propagation in poroelastic media, *Int. J. Numer. Anal. Meth. Geomech.* V14, 27-47.

Christianson, M., Hart, R. Schatz, J (1988) Numerical analysis of multiple radial fracturing, *Key Questions in Rock Mechanics*, Cundall, et al. (eds) Balkema, 441- 451.

Crouch, S.L. (1976) Solution of plane elasticity problems by the displacement discontinuity method. *Int. J. Num. Methods Engng* vol. 10 pp. 301-343.

Crouch, S.L. and Starfield, A.M. (1983) *Boundary element methods in solid mechanics.* London, George Allen and Unwin.

Cundall, P.A. (1988) Formulation of a three-dimensional distinct element model - Part I. A scheme to detect and represent contacts in a system composed of many polyhedral blocks. *Int. J. Rock Mech. Min. Sci. & Geomech. Abstr.* 25:107-116.

Deist, F.H., Georgiadis, E. and Moris, J.P.E. (1972) Computer applications in rock mechanics. *Application of Computer Methods in the Mineral Industry*, 10th Int. Sym. Johannesburg.

Goodman, R. and Shi, G. (1985) *Block theory and its application to rock engineering.* Prentice-Hall, Englewood Cliffs, New Jersey.

Lam K., Cleary, M (1988) Three dimensional fracture propagation under specified well bore pressure, *Int. J. Numer. Anal. Meth. Geomech.* V12, 583-598.

Lawn, B.R. and Wilshaw, T.R. (1975) Fracture of brittle solids. Cambridge University Press.

Napier, J.A.L. (1990) Modelling of fracturing near deep level mine excavations using a displacement discontinuity approach. In H.P. Rossmanith(ed), *Mechanics of jointed and faulted rock*: 709-715. Rotterdam: Balkema.

Napier, J.A.L. (1991) Energy changes in a rockmass containing multiple discontinuities. *J. S. Afr. Inst.Min. Metall.*, 91, 145-157.

Napier, J.A.L. and Hildyard, M.W. (1992) Simulation of fracture growth around openings in highly stressed brittle rock, *J. S. Afr. Inst. Min. Metall.*, 92, 159-168.

Napier, J.A.L. and Peirce, A.P. (1995) Simulation of extensive fracture formation and interaction in brittle materials. In H.P. Rossmanith(ed), *Mechanics of jointed and faulted rock*: 709-715. Rotterdam: Balkema.

Nilson, R, Proffer, W, Duff, R (1985) Modelling of gas-driven fractures induced by propellent combustion within a borehole, *Int J. Rock Mech. Min. Sci.* Vol 22, 3-19.

Peirce, A.P., Spottiswoode, S. and Napier, J.A.L. (1992) The spectral boundary element method: a new window on boundary elements in rock mechanics. *Int. J. Rock Mech. Min. Sci. & Geomech. Abstr.* 29:379-400.

Peirce, A.P. and Napier, J.A.L. (1995). A spectral multipole method for efficient solution of large-scale boundary element models in elastostatics. *Int. j. numer. methods eng.*, 38, 4009-4034.

Plewman, R.P. Deist, F.H. and Ortlepp, W.D. (1969) The development and application of a digital computer method for the solution of strata control problems. *J.S. Afr. Inst. Min. Metall.*, vol. 70, pp. 33-44.

Ryder, J.A. and Napier, J.A.L. (1985) Error analysis and design of a large-scale tabular mining stress analyser. In *Proceedings of the fifth international conference on numerical methods in geomechanics*. Nagoya. 1549-1555.

Salamon, M.D.G. (1964) Elastic analysis of displacements and stresses induced by the mining of seam or reef deposits, *J. S. Afr. Inst. Min. Metall.*, 65, Part IV, 319-338.

Salamon, M.D.G. (1968) Two-dimensional treatment of problems arising from mining of tabular deposits in isotropic or transversely isotropic ground. *Int J. Rock Mech. Min. Sci.* Vol 5, 159-185.

Siebrits, E and Crouch, S.L. (1995) Two-dimensional elastodynamic displacement discontinuity method. *Int J. Num. Meth.Eng.*. Vol 37, 3229-3250.

Swenson D. and Taylor, L. (1983) A finite element model for the analysis of tailored pulse stimulation of boreholes. *Int. J. Numer. Anal. Meth. Geomech.* V7, 469-484.

Vermeer, P.A. and de Borst, R. (1984) Non-associates plasticity for soil, concrete and rock. *HERON* 29:1-64.

3.2 MICROFRACTURE STUDIES

Investigation of brittle rock fracture has been a central topic of investigation in the rock mechanics fraternity for many years. However, robust constitutive models that can be used to represent extension fracturing and the transition from extension fracturing to the formation of shear band structures, are not yet available for incorporation into numerical procedures. The term "extension fracture" is used to designate a fracture that has a single well defined surface that appears to follow the direction of maximum compression and can form under conditions of compressive confinement. This form of fracturing occurs ubiquitously around deep level gold mine stopes and plays an important role in controlling the stress distribution and the stability of deep level stopes. Understanding the genesis of these fractures has been the focus of objective 2.1 in order to facilitate the design of appropriate support systems and assist in the evaluation of strategies that might be used to engineer their formation.

The study of microfracture generation and propagation in rock is essential for understanding basic tensile, extension and shear modes of fracturing and the eventual fracture distribution observed in underground workings. Early investigators have performed a vast number of experiments on crack growth under compressive stress (e. g. McClintock and Walsh 1962, Brace and Bombolakis 1963, Hoek and Bieniawski 1965, Horii and Nemat-Nasser 1985). Various studies predicted that microcracks generated under compression are extensile in nature (e. g. Brace and Bombolakis 1963, Hallbauer, Wagner and Cook 1973, Krantz 1983). These observations were confirmed by experimental electron microscopy work (e.g. Tapponnier and Brace 1976, Wong 1982, Fredrich, Evans and Wong 1989, Zheng 1989). A difficulty most researchers have encountered is to explain the interaction and coalescence of the microcracks to form macro-extension fractures or shear bands. The reason is that only global responses of a granular medium can be monitored in experimental work while information of the micro-processes is needed. A possible solution is to use numerical simulations of granular media to provide this information. Naturally, such numerical experiments have to be compared with physical reality when candidate failure mechanisms have been identified.

A number of noteworthy numerical models of micro-processes are described in the literature. The behaviour of an assembly of bonded particles has been studied with the distinct element method using circular discs (Cundall and Strack 1979, Cundall 1989) and polygonal elements (Handley 1994). No through-grain fracturing was allowed in these models. Numerical models based on the displacement discontinuity principle have been proposed to model the mechanisms of extensile microcrack formation and the interaction of the microcracks to form shear bands (Zheng 1989, Kemeny and Cook 1987, Kemeny and Cook 1991, Reches and Lockner 1994). Further mechanisms of great importance are through-grain splitting, the effects of different grain and matrix elastic properties and the possibility of locked in initial stresses (Friedman 1972). These effects require further investigation to formulate macroscopic localization representations.

The experimental evidence mentioned above indicates that intragranular (through-grain fracturing not propagating across grain boundaries) and transgranular (intragranular fracturing propagating across grain boundaries) fracturing are ubiquitous processes in the damage of rock fabrics. The aim of this research work has been therefore to extend the abovementioned work by addressing the following three questions.

1. Can the initial intra- and transgranular fracture growth in a granular medium be modelled by using a small-strain approach to simulate fractures and grain boundaries as distributed dislocations?
2. Can mechanisms for the generation of tensile fractures in a compressive stress field be identified and modelled?
3. Will it be possible to model the coalescence of microfractures to form a shear band?

Basic flaw mechanisms

The formation of extension fractures in brittle materials has been the subject of many investigations and has received considerable attention in the geotechnical literature (Fairhurst and Cook 1965, Nemat-Nasser and Horii 1982, Horii and Nemat-Nasser 1985, Myer et al. 1992). In the absence of direct tension, the formation of such fractures, parallel to the major principal stress, cannot be explained unless explicit assumptions are made about the microstructure of the material. These include the granular composition, the rock matrix, the mineralogical composition, cleavage directions in grains and the possibility of locked-in stresses (Friedman 1972). An adaptation of the classic Griffith crack model that has been employed to explain extension fracture mechanisms in brittle materials is the so called "sliding crack" model of Brace and Bombolakis (1963) illustrated schematically in figure 3.2.1a.

A substantial volume of literature has accumulated in the detailed analysis of the sliding crack model and various theories have been proposed to explain the formation of shear bands as linked echelon combinations of sliding crack structures (Nemat-Nasser and Horii 1982, Horii and Nemat-Nasser 1985, Myer et al. 1992, Petit and Barquins 1990, Reches and Lockner 1994). By comparing the results of Shen (1995) to those of Nemat-Nasser and Horii (1982 1985), it may be speculated that the bridging fractures form more readily in a granular or porous material such as gypsum than in materials such as glass or perspex (PMMA). This emphasizes that fracture coalescence in brittle materials can be expected to be controlled by both the nature of the material grain structure as well as by material independent stress raising mechanisms such as those illustrated in figure 3.2.1.

Spherical or cylindrical pores have also been postulated as starter mechanisms for the formation of extension fractures (e.g. Sammis and Ashby 1986). Figure 3.2.1b illustrates the formation of extension cracks, from the surface of a cylindrical cavity, which grow in the direction of the applied compressive loading. To examine the effectiveness of this mechanism in explaining the coalescence of macro fractures, the fracturing was simulated as a series of growth steps using the computer code DIGS (Napier ,1990). The result is illustrated in figure 3.2.2a where fractures are allowed to grow from the periphery of two pores which are aligned with an applied compressive stress field. It is apparent that the inner fractures do not link up but are deflected and then terminated. This is very similar to the observed results of experiments conducted in PMMA plates (Sammis and Ashby 1986). The region between the holes is shielded by the holes themselves and induced tensile stresses are too low to promote the coalescence of fractures. Even if no shielding occurs, the circular shape is ineffective in promoting tensile stresses at distances greater than a single hole radius.

In another DIGS simulation, fractures are allowed to initiate between two staggered pores, as shown in figure 3.22b. Strong growth of extension fracture sets, generally aligned to the loading direction, is promoted. This effect is observed also if the fractures are allowed to initiate adjacent to two pores aligned with the loading direction. The potential for fracture formation away from the pore surfaces seems to have been overlooked in experimental studies but could be verified by suitable microscopic observations. It should be noted that fracture nucleation adjacent to a pore will occur only if suitable nucleation sites are available as would be the case in a porous or inhomogeneous material.

Analysis of granular assemblies loaded in extension

Numerical modelling of triaxial extension tests in quartzite was conducted to compare simulated fracture growth in extension with microfractures observed in actual tests (Malan and Napier 1995). The physical experiments were conducted to simulate the stress environments around stopes in deep-level goldmines (Briggs and Vieler 1984). The quartzite used was a siliceous quartzite from the Millar reef in the MB5 zone in the Vaal Reef Basin near Klerksdorp in South Africa and of Precambrian age. The quartz content of the samples varied from 89 - 94 % of which 87 - 93 % comprised quartz grains. Experimental values of Young's modulus and the failure parameters were E = 70 GPa, σc = 320 Mpa and the slope of the failure envelope m = 9.32 respectively. In the experiments, cylinders of 76.2 mm length and 25.4 mm diameter were loaded hydrostatically $(\sigma_1 = \sigma_2 = \sigma_3)$ to the desired confinement and then the axial stress (σ_3) was reduced until the specimen failed. At a level of 42% of the expected axial strain to failure (before plastic strain has occurred) intragranular cracks parallel to the maximum principal stress were observed. The intensity of the intragranular fractures increased with further extension. At 75% of the expected axial strain to failure, transgranular fracturing became visible. With further extension, intra- and transgranular fracturing became intense in certain areas of the specimen. Eventually, coalescence of these fractures led to the formation of a shear zone and failure of the sample.

The triaxial extension test was modelled in plane strain using the DIGS program using three geometries of Voronoi tessellations, with values of k = 0.3, 0.5 and 0.8. The parameter, k, is the ratio of the minimum distance to the average distance between geometric centres in the Voronoi tessellation. Low values of k correspond to angular grains and high k to rounded grains. The simulations were limited to 500 elements (growth elements included). Therefore the size of each sample was limited to about 80 grains to allow appreciable fracture growth to take place. The interfaces between the grains were given properties similar to the experimental rock strength properties corresponding to the overall sample strength. Traction boundary conditions were applied to load the samples to a hydrostatic stress state of 600 MPa.

The similarity of the model results shown in figure 3.2.3a with the experimental samples shown in figure3.2.3b is evident. There is a high density of intragranular fracturing with several transgranular fractures visible. The fractures are sub-parallel to the maximum principal stress and in some areas several parallel fractures occur in the same grain. The density of intergranular fracturing is low compared to intra- and transgranular fracturing, as was noted in the experimental tests.

The importance of including the effect of intra- and transgranular fracturing, along with the intergranular fractures, was analysed by allowing fractures to initiate at seed points within the grains, and at the corners of the Voronoi polygons. Fracture growth is found to occur by two main mechanisms. Firstly, grain splitting occurs in the manner of a Brazilian test (Malan et al. 1994) when tensile stresses are developed in the center of a grain as shown in figure 3.2.4a. Secondly, shearing along a grain boundary can lead to growth of fractures from the ends of the sheared element, as shown in figure 3.2.4b. This corresponds to the sliding flaw mechanism depicted in figure 3.2.1 The stress-strain curves for a typical sample with and without through-grain fracturing are compared with an experimental stress - strain curve in figure 3.2.5a to illustrate the typical behaviour (the full curve is not displayed). The simulation with through-grain fracturing leads to an increase in axial strain at low stresses and thus approaches the experimental curve more closely. The stress-strain curves for Samples 1, 2 and 3 are compared in figure 3.2.5b to illustrate the effect of grain geometry (all other parameters were identical). The more rounded and equal sized grains (Sample 1) result in stronger material with less deformation for the same axial stress. The more angular grains (in sample 3) allow more slip to take place compared to Sample 1 where the rounded grains are interlocked. Through-grain fracturing, however, leads to an increase in axial strain at low stresses in all three samples. Figure 3.2.6 illustrates the density of intra- and transgranular fracturing as a function of strain obtained in the numerical analysis. A similar trend is observed in the experiments with a much bigger increase in intra- than transgranular fracturing density with increasing strain.

Analysis of granular assemblies loaded in compression

A series of numerical experiments were performed to study the effects of Voronoi and Delaunay tessellation patterns on the fracture mechanisms induced in random assemblies of dislocations, as might relate to the micro-structure of granular materials such as rock or concrete (Napier and Pierce 1995). In these experiments, incremental displacements were applied in a sequence of steps to the surface of a rectangular block as shown in figure 3.2.7. The length was set equal to twice the width of the block. Three Voronoi meshes and one Delaunay mesh were constructed by generating random geometric centres in a region covering the area of the block. The polygons were then clipped to conform to the edges of the block. Examples of Voronoi meshes, generated using 1000 random "centres" are shown in figures 3.2.8a and 3.2.8b respectively.

The discontinuities were assigned a cohesion of 15 MPa, tensile strength of 7 MPa, a 45° friction angle and no dilation was permitted. Upon mobilisation, the cohesion and tensile strength are set to zero and the friction angle reduces to 30°. The unconfined failure strength implied by these properties is $\sigma_c = -72{,}4$ MPa. The Young's modulus of the material is set equal to 70 GPa and the Poisson's ratio equal to 0,2.

A series of incremental displacements were applied to one edge of the block as shown in figure 3.2.7. Within each loading step, the boundary displacement was specified and the system was solved with all the internal discontinuities frozen at their current slip/ opening values. Following this, the internal discontinuities were "unfrozen" and the entire problem was re-solved. This process allows for incremental displacement of the boundary in fine steps and reduces spurious failure of discontinuities due to out of balance forces that arise when a new displacement increment is applied. If this procedure is not followed it is found that the block model starts to fail at average axial stresses that are well below the nominal strength implied by the interface properties. This spurious triggering of fracturing by out of balance forces in the numerical procedure must be distinguished from early failure in a real material resulting from random properties of the microstructure.

Three tests were performed to compare the effect of different densities of fractures when axial displacements were applied to unconfined blocks filled with different densities of Voronoi polygons. The test geometries were generated using 200, 1200 and 4000 geometric centres with each problem comprising 629, 1649 and 4052 elements respectively. The fracture patterns resulting from these tests are shown in figures 3.2.9a, 3.2.9b and 3.2.9c. When average axial stresses are computed it is found that the densely tessellated samples of Voronoi shaped grains display almost no load shedding once failure is initiated. In the case of the coarsest grained sample some load shedding occurs, corresponding to the pronounced crack opening seen in figure 3.2.9a. The results of figures 3.2.9b and 3.2.9c suggest that the Voronoi structure may in fact be self stabilizing and that progressively finer tessellations will not necessarily lead to load shedding behaviour. Handley performed a number of experiments on small samples comprising approximately 50 Voronoi grains and noted only limited load shedding in most cases (Handley 1995).

Quantitative comparisons between the results of these three tests shows that the crack density, increases with the progressively finer mesh in V1, V2 and V3 which is clearly visible in figures 3.2.9a, 3.2.9b and 3.2.9c. The coarsest sample, V1, has a higher degree of fracture mobilization than the other two samples V2 and V3, corresponding to a less anisotropic ratio of the principal components of the crack density tensor. In all cases, the alignment of the major fracture trend (the direction of the minor component of the crack density tensor) does not deviate by more than one degree from the loading direction.

Several experiments were carried out to compare the Delaunay triangulation to the Voronoi tessellation. More fractures are generated by the Delaunay triangulation than by the Voronoi tessellation for the same number of geometric centres. For the Delaunay sample D2, it was found that fracturing initiated at the first loading step and that rapid load shedding occurred. Figure 3.2.10a suggests failure by the formation of diamond shaped regions that force cracks to be wedged open in the axial loading orientation. Axial continuation of fractures is more easily accommodated in the Delaunay structure than in the Voronoi configurations (compare figures 3.2.9b and 3.2.10a). The tessellation scheme also has a striking effect on the volumetric strain in the sample with the Delaunay sample showing much stronger post-failure dilatancy than the Voronoi sample as shown in figure 3.2.11a.

The application of a lateral confinement of -10 MPa to the sample alters the final fracture pattern induced in the sample as shown in figure 3.2.10b, suggesting the incipient nucleation of a shear band forming diagonally across the sample. It was found that the sample shed load following each axial strain increment. The equivalent Voronoi tessellation showed no post-failure load shedding. These differences are shown most clearly in figure 3.2.11 in which axial stress is plotted against axial strain for the Voronoi and the Delaunay samples subjected to both uniaxial and confined compression.

In the case of the unconfined axial loading tests, the post-failure dilation angle $\overline{\psi}$, is found to rise sharply from the initial onset of failure to values between 25° and 30° as compared to the much lower values of between 6° and 15° for the confined loading tests. It is also found that the dilation is mobilized sooner in the Delaunay samples than in the Voronoi samples.

Allowing fracture growth to be initiated within a Voronoi assembly in addition to the mobilization of predefined discontinuities results in additional tensile fractures being nucleated within and from the vertices of the predefined grains. This leads to rapid load shedding and disintegration of the sample. The through-grain fracturing effectively modifies the angularity of the Voronoi grains which apparently has a major influence in reducing interlocking between grains.

In the simulations mentioned above, fracture was allowed to initiate simultaneously at all grain boundaries where the local stress state fell on or outside the specified failure surface. An alternative procedure is to allow fracturing to initiate in an incremental fashion by evaluating the stress tensor at each possible failure site and then mobilizing only the most favourable site according to a specified criterion. This can be considered to be a "weakest link" approach in which failure is allowed to occur in sequential steps. Figure 3.2.12a shows the first 100 cracks to be activated in an unconfined loading test on a Voronoi assembly. It is observed that failure initiates near one corner of the sample and then progresses across the sample forming a shear band mechanism. The initial angle of the band is at approximately 30 to 35 degrees with respect to the loading direction as compared to the theoretical Coulomb angle of 22,5 degrees for an internal friction angle of 45 degrees. The angle predicted by bifurcation theory (Vermeer 1990) would be 33,7 degrees.

If the uniaxial loading experiment is repeated using a Delaunay triangulation, the initial failure pattern is as shown in figure 3.2.12b and corresponds to the axial splitting mode observed in experiments, as depicted in figure 3.2.12c. If confinement is applied to the sides of the sample, the failure mode progresses in a connected echelon structure as shown in figure 3.2.13a, forming a type of shear band mechanism. A shear band that is observed in experiments is shown in figure 3.2.13.b. This is a very encouraging result in simulating the transition from extension to shear fracturing as confinement is increased. It is also of interest to note that in figure 3.2.13a, the effective shear band orientation seems to be closer to the Coulomb angle than the structure in figure 3.2.12a. It appears that the shape of the material grains affects not only the load shedding characteristics of the material but also the failure mode. The rounded grain shapes corresponding to the Voronoi assemblies apparently promote inherent shear banding even under uniaxial conditions.

Additional studies were done to investigate the influence of the micro-failure criteria and the properties of the Coulomb friction law assigned to the flaw surfaces. Brittle fracturing of the flaw surface is simulated by causing the cohesion to drop to a residual value after the failure criterion is attained. The material exhibits load shedding in the global stress - strain curve. Modelling of perfectly plastic sliding by keeping the cohesion constant during and after failure leads to an overall hardening of the global stress - strain response. Fewer flaws are activated and the active flaws are more evenly distributed throughout the sample. An increase in the dilation angle results in greater lateral strain in the sample and a greater ratio of the radial inelastic strain to the axial inelastic strain.

The macroscopic pattern of fracture activation depends on the choice of the micro-failure criterion. A failure criterion based on the excess shear concept results in the activation of short chains of fractures in the direction of the maximum principal stress which are arranged in a band across the sample as shown in figure 3.2.12a. When the tensile strength is used as the activation criterion, the fractures link up into a long backbone across the sample with several branches radiating towards the sample edges. The criterion that is used to activate a crack element can also alter the fracture pattern. All results presented have assumed that each crack element contains two collocation points and that only one of the collocation points needs to fail. The element containing the collocation point that is furthest outside the failure envelope will initiate first. An alternative is to permit activation only when both collocation points are outside the failure envelope. In this case, the directions of the active elements are close to the Coulomb angle with very few in the direction of the principal stress. Linking of elements with opposite sign leads to the formation of cracks which are approximately in the direction of the principal stress

A square sample with a side length of 80 mm was used to study the influence of initial flaws in the sample. The region was discretized with a Voronoi tessellation such that the polygons reprenting the grains are approximately the same size as in the smaller, rectangular sample. The change in geometry lead to a different macroscopic failure mode, shown in figure 3.2.14a, which corresponds to splitting in uniaxial compression instead of the formation of a shear band.

The application of a lateral confinement causes a fracture patttern which corresponds more closely to a shear band. The inclusion of a few flaws with lower cohesion introduces a region of high excess shear stress adjacent to the flaws. The stronger seeds activate in this region which propagates away from the flaw positions. The pattern of the active elements appears to be affected by the position, number and constitutive properties of the flaws.

Fracture modelling with discrete elements

Some numerical experiments have been performed which attempt to model the fracture processes in brittle rock with the Particle Flow Code (PFC) by representing the material as a collection of circular particles bonded together (Cundall 1995). The model seems to reproduce much of the behaviour that can be observed in physical tests and reveals mechanisms that are difficult to observe physically. For example, discrete cracks produced in tensile tests resemble physical fractures, sharp cracks propagate from a notch and rough tensile ruptures develop in unnotched specimens.

In unconfined compression tests, "microcracks" form parallel to the major axis and subsequently link up in structutures which macroscopically resemble shear bands, but microscopically embody a buckling or kinking mechansim with intense rotation of the particles. The linking up of microcracks depends on imposed kinematic constraints such as the end confinement. The application of biaxial confinement leads to extensive damage throughout the sample. Angled bands of cracks are produced but the microcracks exhibit a greater variation in angles than in the unconfined test. There is more slip on cracks and the episodes of failure are more sporadic and localized. The stress - strain curves resemble those seen in physical tests and the mechanisms develop automatically as a function of the loading and the boundary conditions. Qualitatively, there are some differences between numerical and physical results. No attempt was made to match the numerical model to any physcial material and the ratio of unconfined compressive strength to tensile strength is 4 which is much lower than observed (e.g. 20).

Some discrepancies are evident between the predictions and the assumptions of linear elastic fracture mechanics concepts. For example, the energy release rate is not equal to the crack extension force (a measure of energy absorbed) and there is no clear demarkation between regions of energy absorption and those of energy release. The computed fracture toughness appears to depend on the particle size if the direct tensile strength is made independent of the particle size. Further studies are required to resolve these differences and to vary the parameters to match a particular rock type.

Conclusions

Flaws in rock, such as sliding cracks or pores, can be easily modelled using the boundary element approach. The modelling has demonstrated how tensile fractures can be generated from these flaws in a compressive stress field. The studies have also shown that tensile fractures may be initated in the material surrounding the flaws due to the alteration of the stress field near the flaw.

The tessellation approach to modelling has provided many insights into the relationships between the micro-mechanics of flaws in rock and the failure of macroscopic samples. It is found that the tessellation pattern can have a dramatic effect on the sample failure characteristics and mechanisms. In particular, the Voronoi assemblies are less prone to shed load than the Delaunay triangulations. Increasing the density of Voronoi polygons does not appear to affect this conclusion; the Voronoi structure appears to be mechanically different from the Delaunay structure as individual cells become finer.

It is also found that the principal components of the crack density tensor are respectively orthogonal to and aligned with the axial loading direction. The predominant fracture orientation is parallel to the loading direction. The dilation angle, reflecting post-failure plasticity, is strongly reduced when lateral confinement is applied to the samples.

Finally, it is seen in a particular case that the inclusion of fracture growth mechanisms in a Voronoi assembly has a dramatic effect in reducing the post-failure load bearing capacity of a simulated granular material. Changing from a simultaneous activation rule to a sequential approach results in macroscopic failure patterns which closely correspond to failure modes observed in laboratory tests. Further studies have demonstrated that the macroscopic stress - strain behaviour of the sample is strongly dependent on the material properties assigned to the microscopic flaws. A challenging task which still remains is to link particular tessellation schemes to particular material characteristics such as grain size, porosity and crystal anisotropy.

References

Brace, W.F. and Bombolakis, E.G. (1963). A note on brittle crack growth in compression. *J. Geophys. Res.*, Vol. 68, pp. 3709-3713.

Briggs, D. J. and Vieler, J.D.S. 1984. Microfracture studies of quartzite in triaxial extension. *COMRO (now Miningtek, CSIR, South Africa) Internal Research Report* 12/84 (1984).

Cundall, P.A. 1989. Numerical experiments on localization in frictional materials. *Ingenieur-Archiv*, 59: 148-159.

Cundall, P.A. (1994) . A preliminary constitutive model for extension fracture based on micromechanics. *Unpublished Report to CSIR Division of Mining Technology.*

Cundall, P.A. (1995). Fracture modelling by micromechanics. *Unpublished Report to CSIR Division of Mining Technology.*

Cundall, P.A. and Strack, O.D.L., (1979). A discrete numerical model for granular assemblies. *Geotechnique*, 29: 47-65.

Fairhurst, C. and Cook, N.G.W. (1965). The phenomenon of rock splitting parallel to a surface under compressive stress. *Unpublished Chamber of Mines Research Report* No. 65/65.

Fredrich, J.T., Evans, B. and Wong ,T.-f., (1989). Micromechanics of the brittle to plastic transition in Carrara marble. *J. Geophys. Res.*, 94: 4129-4145.

Friedman, M. (1972). Residual elastic strain in rocks. *Tectonophysics*, Vol. 15, pp. 297-330.

Hallbauer, D.K., Wagner, H. and Cook ,N.G.W., (1973). Some observations concerning the microscopic and mechanical behaviour of quartzite specimens in stiff, triaxial compression tests. *Int. J. Rock Mech. Min. Sci.*, 10: 713-726.

Handley, M.F. (1995). An investigation into the constitutive behaviour of brittle granular media by numerical experiment. *PhD. Thesis*, Univ. of Minnesota.

Hoek, E. and Bieniawski, Z.T., 1965. Brittle fracture propagation in rock under compression. *Int J. Fract. Mech.* 1: 137-155.

Horii, H. and Nemat-Nasser, S. (1985). Compression-induced microcrack growth in brittle solids: axial splitting and shear failure. *J. Geophys. Res.*, Vol. 90, pp. 3105-3125.

Kachanov, M. (1992). Effective elastic properties of cracked solids: critical review of some basic concepts. *Appl. Mech. Rev.* 45:304-335.

Kemeny, J.M. and Cook, N.G.W., (1991), Micromechanics of deformation in rocks. In Shah, S.P., ed., *Toughening mechanisms in Quasi-brittle Materials*, Kluwer Academic Pub., Netherlands, 155-188.

Kranz, R.L., 1983. Microcracks in rocks: a review. *Tectonophysics*, 100: 449-480.

Malan, D.F. and Napier, J.A.L. (1995). Computer modelling of granular material microfracturing. *Tectonophysics*, paper accepted for publication.

Malan, D.F., Napier, J.A.L. and Watson, B.P., 1994. Propagation of fractures from an interface in a Brazilian test specimen. *Int. J. Rock Mech. Min. Sci.*, 31: 581-596.

McCLintock, F.A. and Walsh, J.B., 1962. Friction on Griffith cracks in rocks under pressure. In: Proc. *4 th U.S. Nat. Congr. Appl. Mech.*, New York, ASME, 1015-1021.

Myer, L.R. et. al. (1992). Extensile cracking in porous rock under differential compressive stress. *Appl. Mech. Rev.*, Vol. 45, No. 8, pp. 263-380.

Napier, J.A.L. (1990). Modelling of fracturing near deep level mine excavations using a displacement discontinuity approach. In H.P. Rossmanith(ed), *Mechanics of jointed and faulted rock*: 709-715. Rotterdam: Balkema.

Napier, J.A.L. and Peirce, A.P. (1995). Simulation of extensive fracture formation and interaction in brittle materials. In: H.P. Rossmanith (Editor), *Mechanics of Jointed and Faulted Rock - MJFR -2.* Balkema, Rotterdam, pp. 63-74.

Nemat-Nasser, S. and Horii, H., (1982). Compression-induced nonplanar crack extension with application to splitting, exfoliation, and rockburst. *J. Geophys. Res.*, 87: 6805-6821.

Nemat-Nasser, S. and M. Horii (1993). *Micromechanics: Overall properties of heterogeneous materials*. Amsterdam, North-Holland series in applied mathematics and mechanics.

Nemat-Nasser, S. and Horii, H. (1982). Compression-induced nonplanar crack extension with application to splitting, exfoliation, and rockburst. *J. Geophys. Res.*, Vol. 87, pp. 6805-6821.

Petit, J.P. and Barquins, M. (1990). Fault propagation in mode II conditions: Comparison between experimental and mathematical models, applications to natural features. In: H.P. Rossmanith (Editor), *Mechanics of Jointed and Faulted Rock*. Balkema, Rotterdam, pp. 213-220.

Reches, Z. and Lockner, D. (1994). Nucleation and growth of faults in brittle rocks. *J. Geophys. Res.*, Vol. 99, pp. 18159-18173.

Sammis, C.G. and Ashby, M.F. (1986). The failure of brittle porous solids under compressive stress states. *Acta Metall.*, Vol. 34, pp. 511-526.

Shen, B. (1995). The mechanism of fracture coalescence in compression - experimental study and numerical simulation. *Engng. Fracture Mech.*, Vol. 51, pp. 73-85.

Tapponier, P. and Brace, W.F., (1976). Development of stress-induced microcracks in Westerly granite. *Int. J. Rock Mech. Min. Sci.*, 13: 103-112.

Vermeer, P.A. (1990). The orientation of shear bands in biaxial tests. *Geotechnique,* Vol. 40, pp. 223-236.

Zheng, Z., 1989. Compressive stress-induced microcracks in rocks and applications to seismic anisotropy and borehole stability. *PhD Thesis*, University of California, Berkeley.

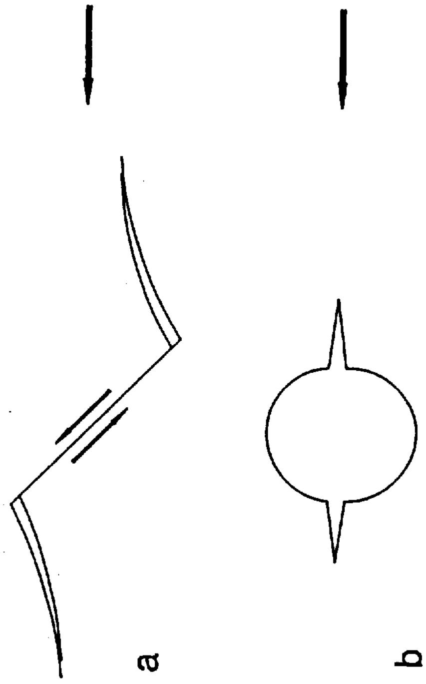

Figure. 3.2.1 Basic flaw mechanisms used to explain extension fracturing parallel to the direction of maximum compression. a) Sliding crack. b) Circular pore.

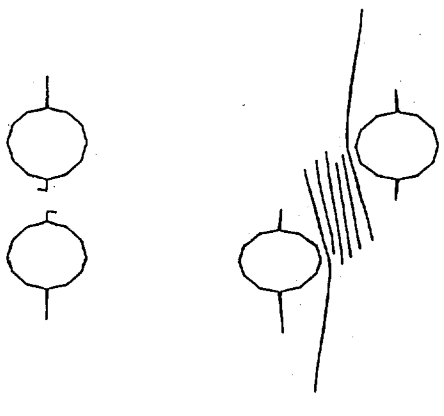

(a) (b)

Figure. 3.2.2 Growth of extension fractures near open pores on a horizontally applied stress field. a) Growth from the pore surfaces in the direction of the applied load. b) Growth between staggered pores from positions between the pores.

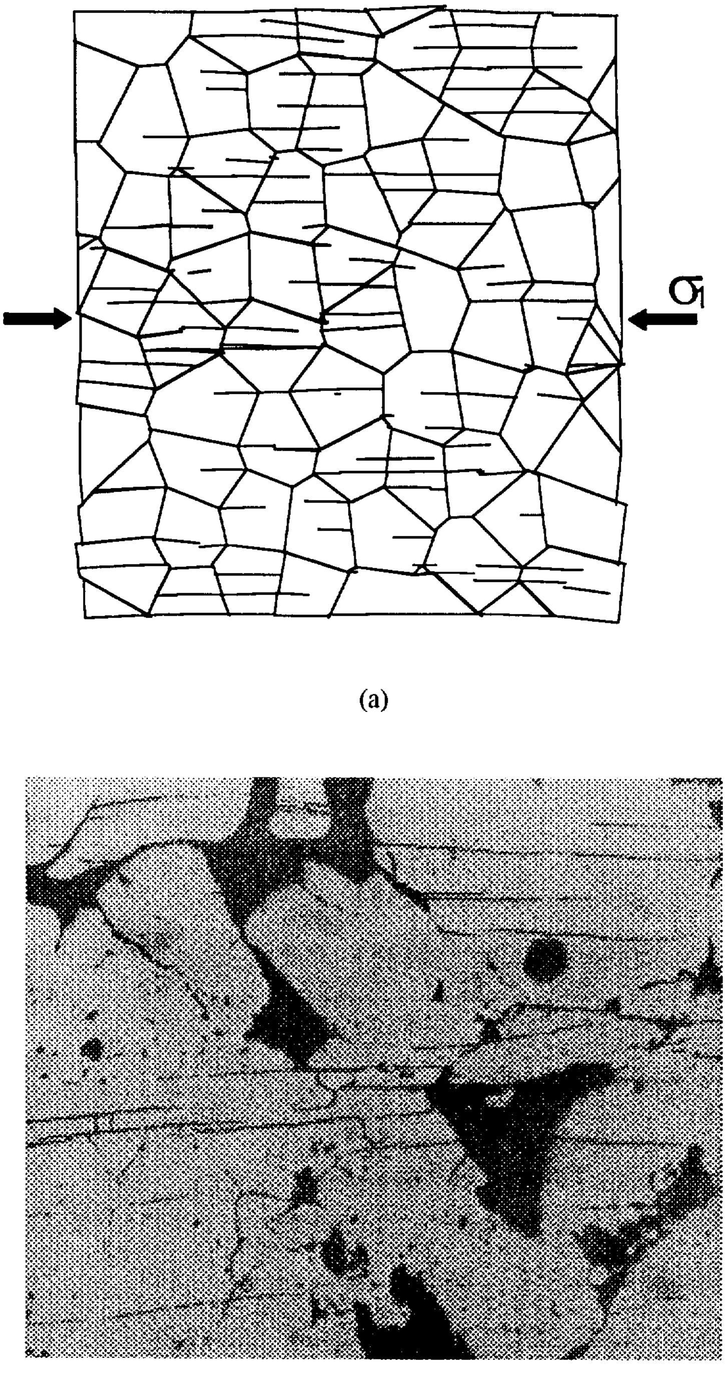

Figure 3.2.3 : a: Simulated and b: observed fracture patterns in triaxial extension test.

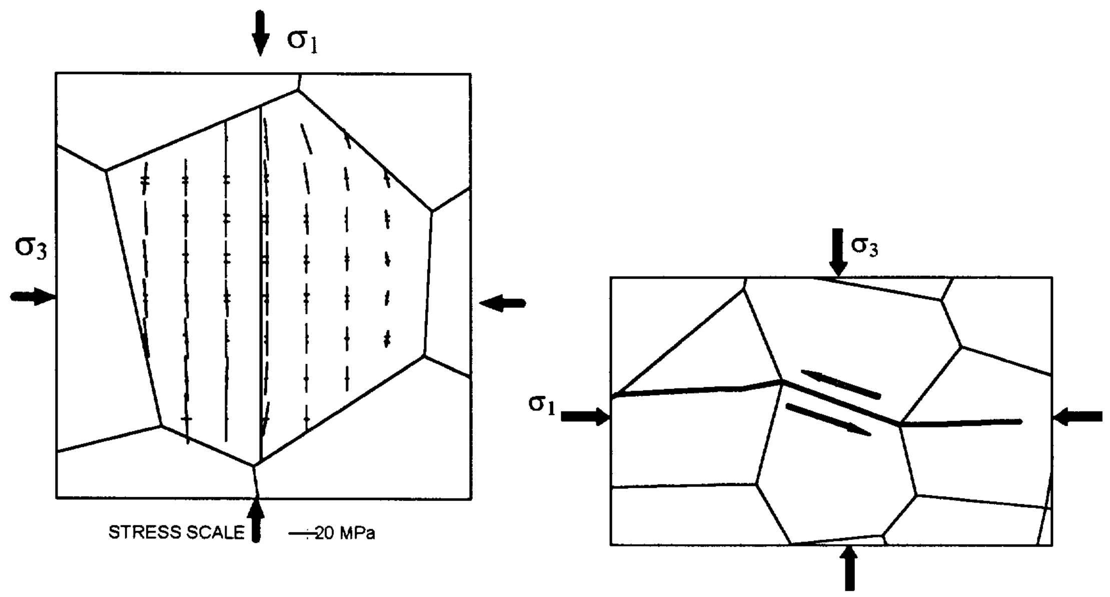

Figure 3.2.4 Micro mechanisms for the formation of intragranular fracturing observed in triaxial extension test simulation.

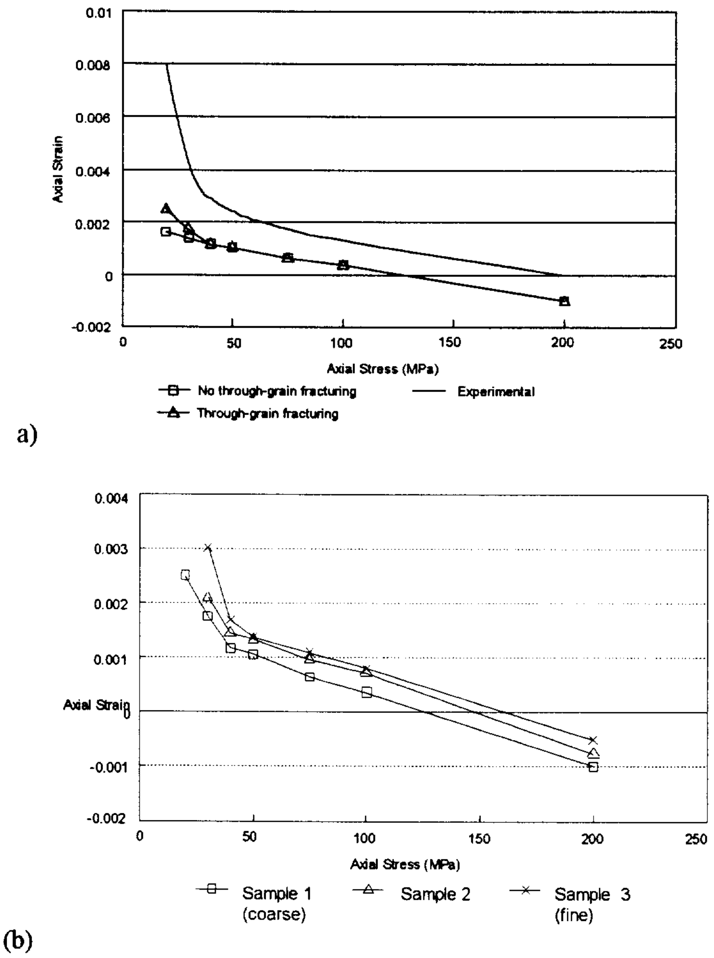

Figure 3.2.5 Axial strain - axial stress response obtained in simulation of triaxial extension tests. a: Effect of permitting intragranular fracturing, b: Effect of decrease in Voronoi polygon size .

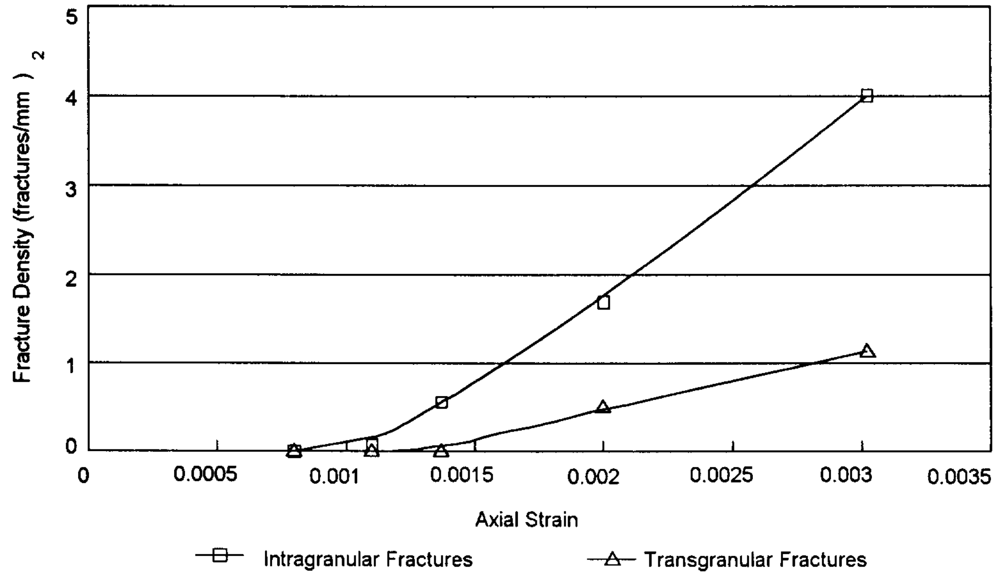

Figure 3.2.6 Increase in intra- and transgranular fracturing with axial strain in simulation of extension test.

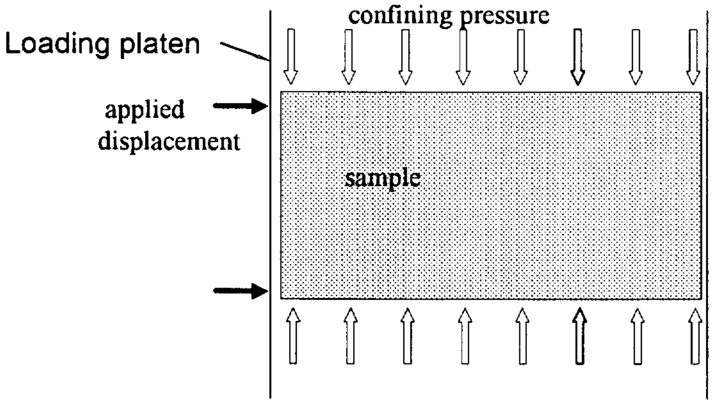

Figure: 3.2.7 Schematic of rectangular sample and loading

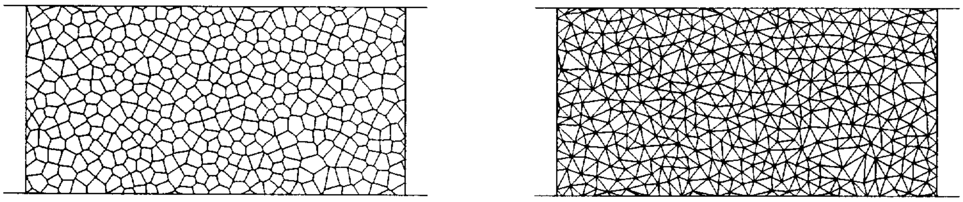

a. b:

Figure. 3.2.8 Examples of random tessellation patterns
a. Voronoi polygons b. Delaunay triangles.

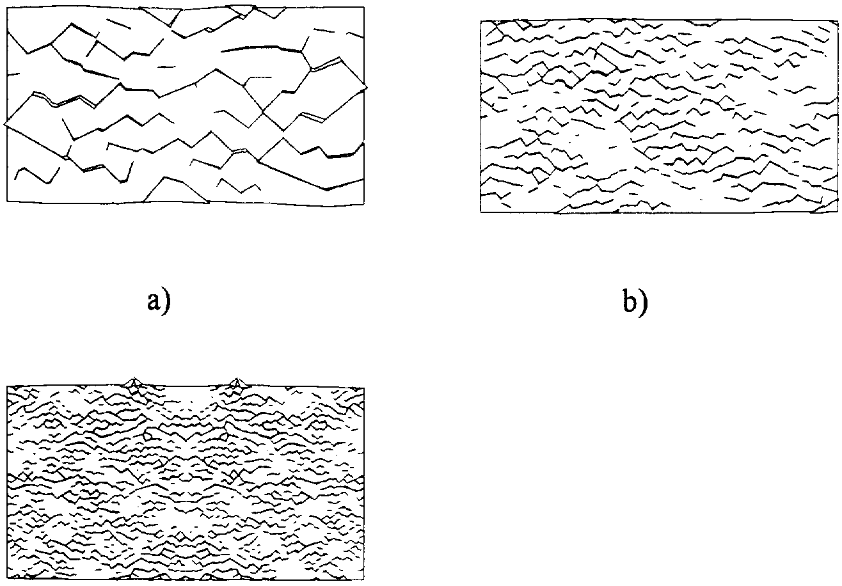

a)

b)

c)

Figure.3.2.9 Failure patterns in progressively finer Voronoi tessellations of uniaxially loaded samples. a) V1 - Coarse b) V2 - Intermediate c) V3 - Fine.

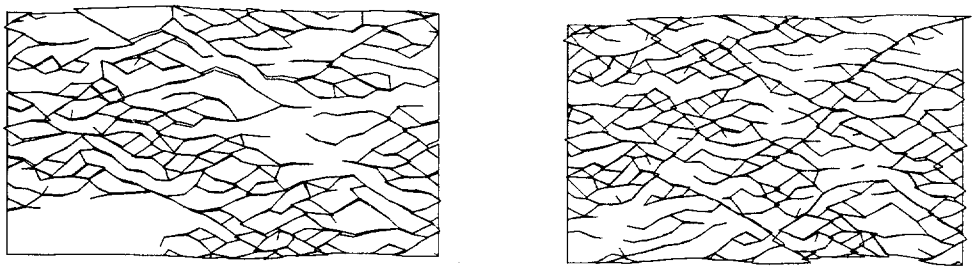

a.

b

Figure. 3.2.10 Deformation pattern of Delaunay sample D2 after six steps. a). Unconfined loading b) Confined loading.

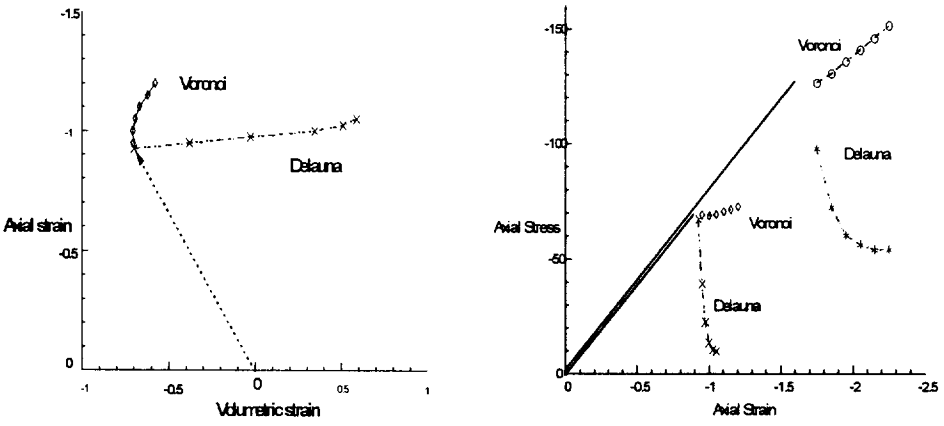

(a) (b)

Figure. 3.2.11 Comparison of Delaunay and Voronoi samples D2 and V2. a: axial strain against volumetric strain plots b: Axial stress plotted against axial strain

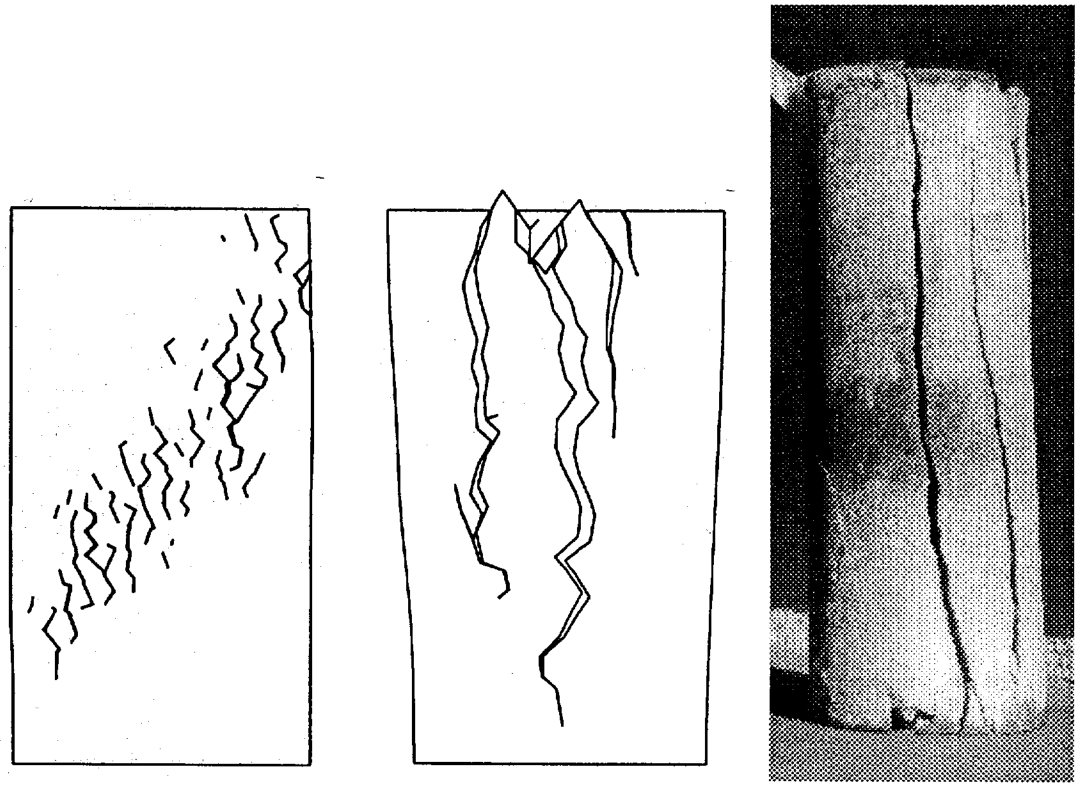

(a) (b) (c)

Figure. 3.2.12 Incremental activation of fractures. a) Shear band mechanism developing in a Voronoi assembly - uniaxial loading. b) Axial splitting using triangular grains - uniaxial loading. c) Photograph of quartzite specimen showing axial splitting

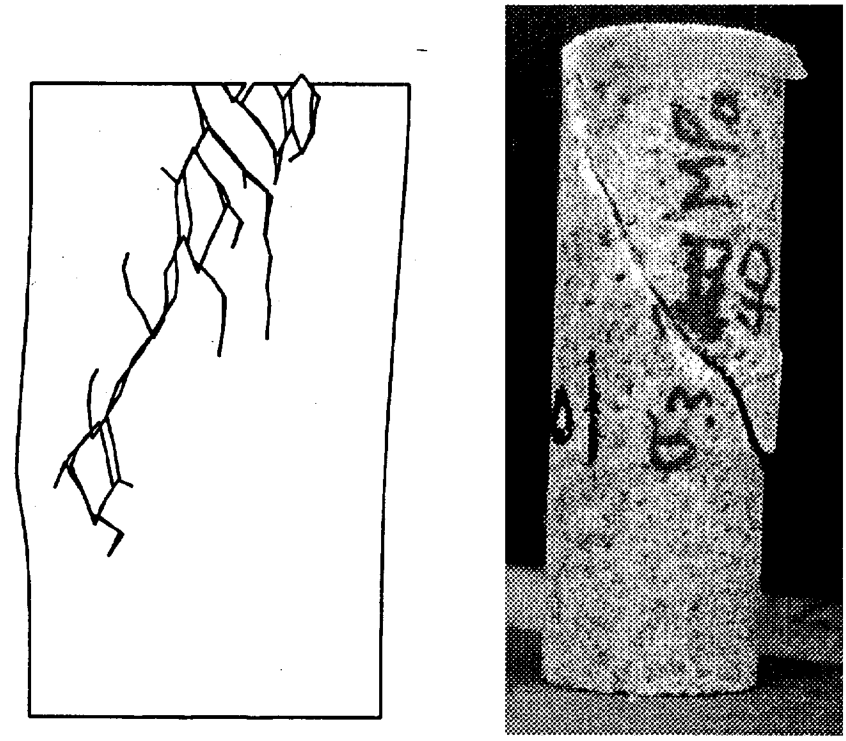

Figure. 3.2.13 Incremental activation of fractures. a) Transition to shear banding with triangular grains - confined loading. b) Photograph of quartzite specimen showing shear band

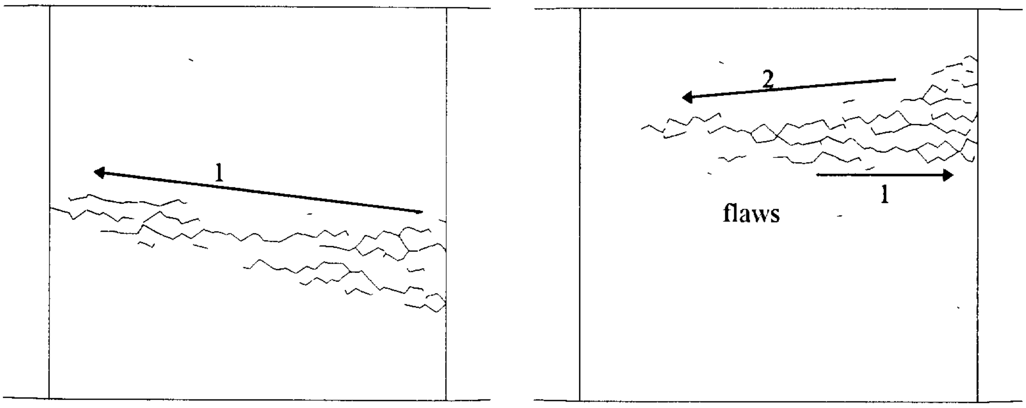

(a)

(b)

Figure 3.2.14 Incremental activation of fractures in a square block containing initial flaws. Arrows and numbers indicate the direction and sequence of the flaw activation.

3.3 PHYSICAL MODELLING

3.3.1 MODELLING OF FRACTURING SURROUNDING MINE OPENINGS AND PILLARS

One of the major impediments in the field of numerical modelling in rock mechanics is the limited knowledge of the mechanisms of fracture and failure of brittle rock. Improving the understanding of rock behaviour and developing better numerical models are interactive processes and the two need to be continually checked and validated against each other. Physical information obtained in situ is preferred to facilitate this interaction, but, in many cases, this is difficult because of the complexities involved in describing the rock mass structure and determining operating forces in situ. Testing of models under controlled conditions in the laboratory is probably a better option for initial calibration and validation of numerical models and constitutive laws, as well as studying the process of fracture initiation and growth.

This section describes the experimental work carried out during 1993 and between August 1994 to December 1995, firstly to improve the understanding of mechanisms of fracture onset and growth in brittle rock and, secondly to validate and calibrate the DIGS computer code. The work undertaken consists of two parts: The first part focuses on fracture formation and development around a mine-like opening in a layered brittle material, namely glass. The second part concentrates on fracture initiation and growth of fracturing in rock material caused by stress raisers encountered in mining such as pillars.

In this series of tests the models were prepared from square glass plates, each measuring 15x15x1 cm. A rectangular opening was introduced by arranging a series of adjacent glass strips, with a suitable gap, at the centre of the layer assembly. Figure 3.3.1.1 shows a cross section through a typical model and the test rig used. The relevant physical properties of the glass used are UCS = 50 MPa, E = 73 GPa, ν = 0,22 and , ϕ (between glass layers) = 13°. The layer assembly was subjected to biaxial loading applied in directions perpendicular and parallel to the layers. The layer faces perpendicular to the long axis of the central opening were stress free.

Two series of tests were carried out. In the first series, the model contained only one glass strip, which was removed after loading to simulate face advance. The model was first loaded to 7

MPa both horizontally and then the vertical stress was increased to 30 MPa. After recording the fracture pattern developed under load, the stress was lowered to zero, in a reverse sequence to the initial loading procedure.

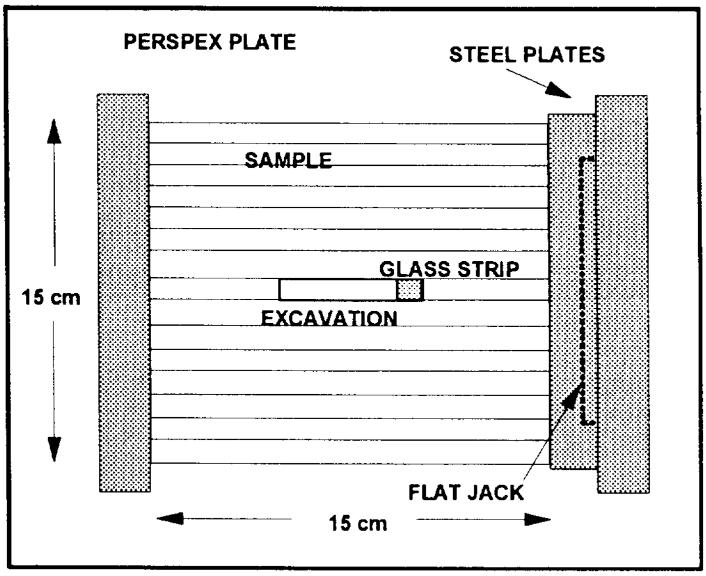

Figure 3.3.1.1 The schematic diagram of the glass layer model and test rig

Figure 3.3.1.2 shows typical results as obtained from one of the tests carried out for the one strip case. As seen in this figure, fracturing initiates at the inward corners of the excavation and no tension fractures occur at the centre, probably due to the 7 MPa confinement applied horizontally to the model. The fractures are not always continuous across layer interfaces. After the removal of the glass strip to simulate face advance, fracturing becomes more intense on the stationary edge. At the final stage of loading (27 MPa), fracturing on both sides becomes nearly perpendicular to the excavation.

The second series is similar to the first series, except that five face advance steps are carried out.

The same loading procedure was repeated for removing each subsequent strip corresponding to a face advance increment.

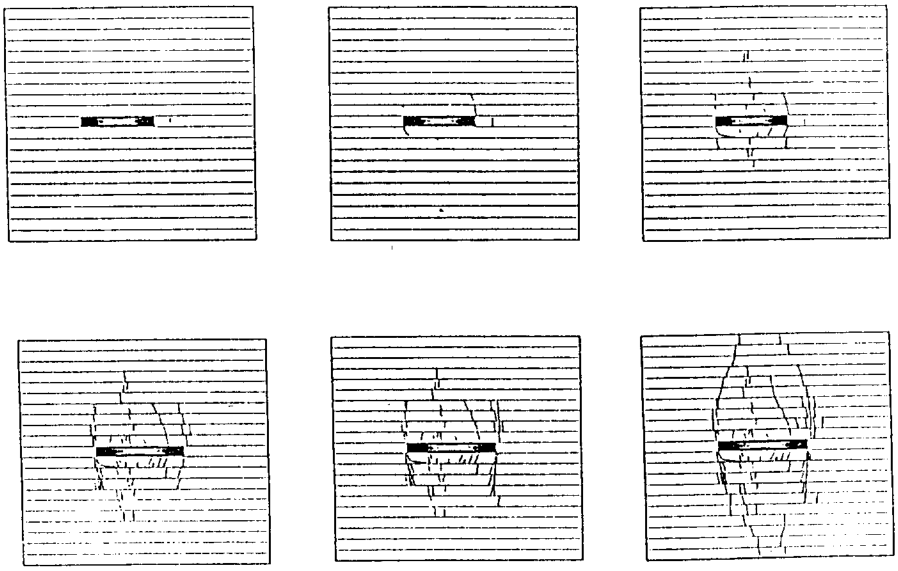

Figure 3.3.1.2 A schematic illustration of the development of the fracture pattern obtained from the single step mining

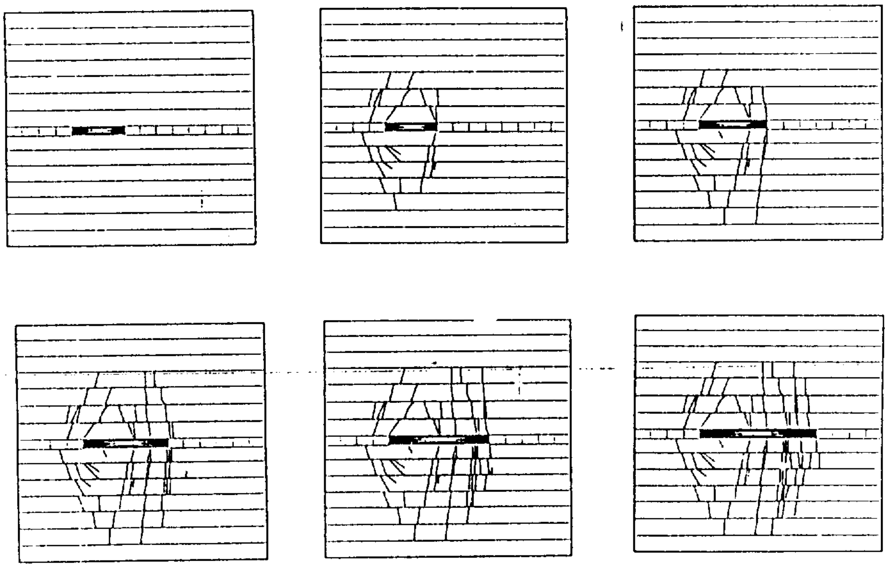

Figure 3.3.1.3 A schematic illustration of the development of the fracture pattern obtained from the multiple steps mining

The diagrams in Figure 3.3.1.3 show the fracture sequence at particular mining steps during multiple strip tests. As in the first tests tension fracturing in the centre of the slots is inhibited. Although initially the fracturing sequence is not related to the position of the opening, the final pattern shows that the fractures align almost vertically to the layers at the highest load (26 MPa) and at a particular mining stage. The orientation of fracture growth tends to become vertical as the opening is enlarged. At the largest span, the fractures at the corners develop away from the opening's centre line, towards the solid.

A numerical simulation of fracture growth around the initial opening was carried out using DIGS. Tension fractures, controlled by the tension growth rule were allowed to initiate fractures at the layer interfaces and at seed points within the layers. Figure 3.3.1.4 shows the simulated pattern of fracturing in the lower half of the layer assembly. The upper boundary shown in Figure 3.3.1.4 was specified as a plane of symmetry. Although fractures are seen to initiate from the layer interfaces, it is clear that tensile stresses induced parallel to the horizontal surface of the opening, cause tension fractures to develop at the centre of the opening. This is not observed in the physical model (Figures 3.3.1.2 and 3.3.1.3).

The principal stress pattern close to the surface of the opening, when no fractures are formed, is shown in Figure 3.3.1.5 where the tensile stress components are plotted as double lines. Large tensile stresses are seen to act parallel to the surface of the opening and along the interface below each side of the opening. However, it is also apparent that very large shear stresses occur near the corners of the opening at points A and B. If fractures are allowed to initiate at the corners, according to the shear growth rule, the fracture pattern is altered significantly as shown in Figure 3.3.1.6. In this case no tension fracturing arises at the centre of the opening because the induced tensile stress parallel to the surface of the opening is relieved by the formation of the shear driven fractures at the corners. Figure 3.3.1.6 depicts the formation of fractures following the first excavation step and shows that the fracture activity seems to move with the active side of the opening which is similar to the trend observed in Figures 3.3.1.2 and 3.3.1.3. A complete simulation of the fracture patterns observed in Figures 3.3.1.2 and 3.3.1.3 has not yet been accomplished. However, it is felt that efforts should now be directed towards the resolution of appropriate growth rules for rock materials rather than non-granular material such as glass.

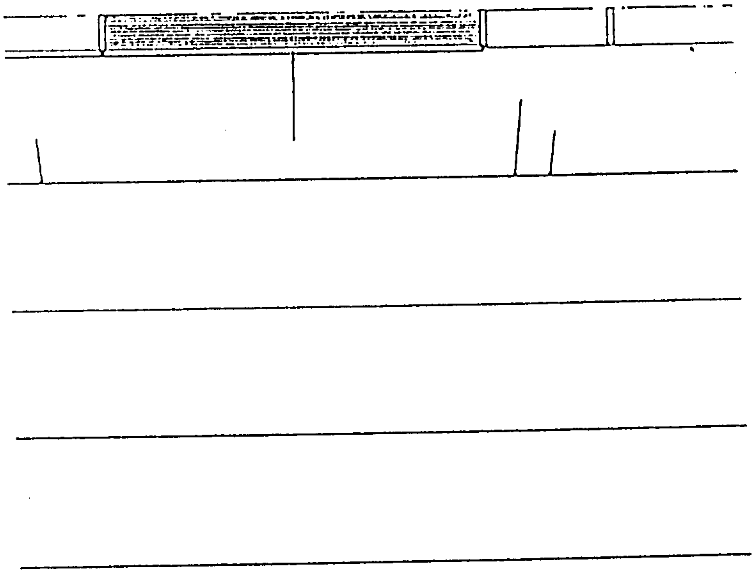

Figure 3.3.1.4 Simulated fracture growth in glass layers using the tension fracture growth rule

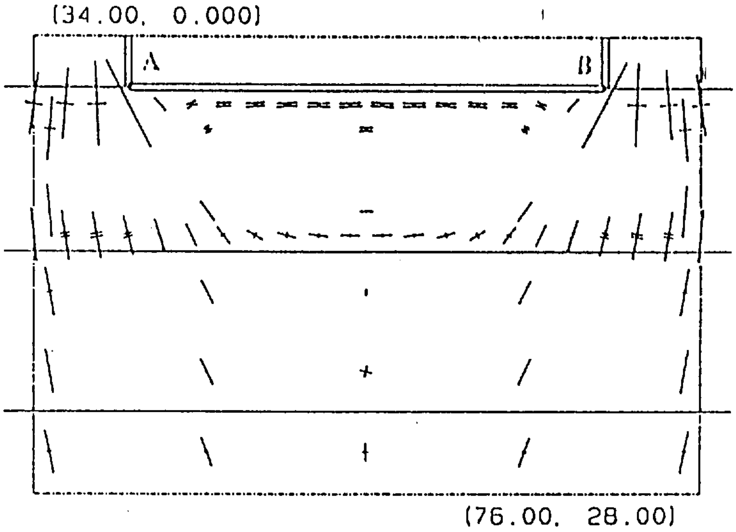

Figure 3.3.1.5 Principal stress plot near the opining when no fracturing has occurred. (Double lines denote tensile principal stress values).

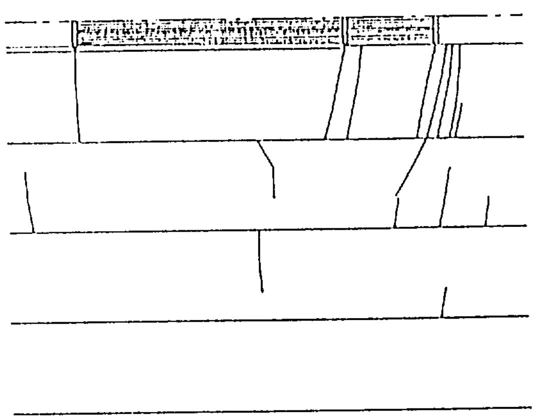

Figure 3.3.1.6 Simulated fracture growth in glass layers when shear driven fractures initiate from the edges of the opening.

Punch tests

The major objective of this work was to study the initiation of fractures in a layered material subjected to concentrated loading beneath circular and strip punches. The objective was to compare the patterns of fracturing between these two extreme loading geometries and to gain initial insight into the mechanisms of failure below pillar structures, which can be related to strip punch loading experiments. In particular, the following points are addressed a) where and how fractures first form, b) whether their first appearance changes with the characteristics of the layer, and if so, how? c) if there is more than one type of crack, do certain types coincide with certain regions of the complete stress-strain curve? and d) how does the rock type affect the fracture growth and its pattern? A literature survey pertaining to these questions was carried out. The following aspects were found to be related to the work undertaken:

- Effect of ratio between the width of loading and thickness of top layer on stress. σ_x, σ_y and τ_{xy} increase steadily with increasing b/h' (see Figure 3.3.1.7) at all points when the surface loading is uniformly distributed and of constant intensity.

- In changing the friction conditions at the interface from rough to smooth there is a substantial increase in horizontal tensile stress in the upper layer, and considerable increase in horizontal compressive stress in the lower layer. There is only a very slight change in the σ_y vertical stress at all points (usually a small decrease in stress), and very little change in the value of τ_{xy}, except at the interface where , the shear stress is zero. This clearly indicates the pronounced effect friction has on the horizontal stresses in both layers, and hence the necessity of taking friction into account in a rational analysis.

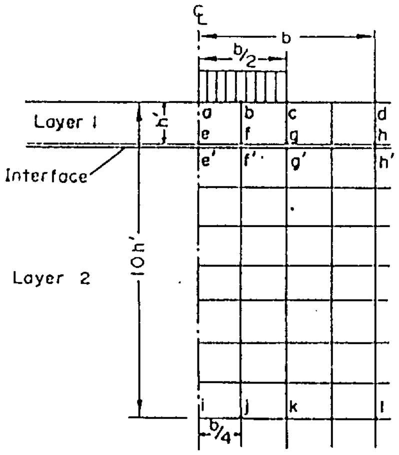

Figure 3.3.1.7 Two-layer system showing locations at which stresses were computed

- Effect of E_2/E_1 ratio on stress. For the smooth layers it was found that increasing the stiffness ratio E_2/E_1 from 0.02 to 0.1 i.e. decreasing E, nearly doubles the vertical stress,σ_y, at the interface and the horizontal stress,σ_x,(compressive) is reduced by a factor of 2. Increasing the stiffness ratio results in less load being carried by flexural stress and more by direct bearing on the supporting layer.

- In a layered media with E increasing downwards the σ_y stresses are of the same order of magnitude as those obtained in the case of homogeneous media having an elasticity modulus equivalent to that of the first layer. However in the case of layered strata with a value of E decreasing downwards, σ_y is less than that in homogeneous strata.

- Soft strata below the top layer reduce tension in the vertical direction compared to homogeneous strata.
- As the strength of rock under compression increases with confinement it is very unlikely that the rock will fail beneath the punch where all three principal stresses are compressive.

- Considering the relatively small tensile strength of rock it can be concluded that the failure will start with a tensile ring crack close to the edge of the stamp, when the tensile stresses reach their maximum value.

- It can be assumed that the rock will fail along the contour of a hemispherical region where one of the three principal stresses is tensile.

- At low confining pressure, the mode of rock fracture changes and a vertical tensile crack, parallel to the axis of the punch, splits the specimen before the formation of rock chips at the surface.

Description of the tests

Cylindrical (axisymmetric) tests were conducted on 54 mm diameter cylindrical specimens, prepared from solid or layers of sandstone, norite and quartzite (Table 3.3.1). The specimens were loaded by a 10 mm diameter cylindrical steel punch, under both confined and unconfined conditions. For the tests with confinement, the specimens were placed in a 4 mm thick steel tube and the level of confinement was monitored by strain gauges placed on the tube. The specimens were loaded to failure and sections were taken to observe the degree and pattern of fracturing that occurred in them.

Unconfined tests

In this series, solid and layered cylindrical sandstone specimens were subjected to "punch" loading using a 10 mm diameter cylindrical steel piece. The mode of failure observed in the 54 mm diameter and 60 mm long solid sandstone specimen is diagrammatically shown in Figure 3.3.1.8. The mode of failure is characterised by the formation of an inverted cone immediately under the punch and a radial tensile crack along the axis of the specimen. The base diameter and height of the cone are about 10 mm, which is equal to the punch diameter. The cone appears to have wedged into the specimen, axially splitting it in extension into two pieces. The white powdered material observed on the conical surface implies shear fracturing around the cone, while the split surfaces being free from any gouge material is an indication of failure in tension.

	NORITE	*SANDSTONE*	*QUARTZITE*
UCS (MPa)	210	90	200
ELASTIC MOD.(GPa)	112	21	70
POISSON'S RATIO	0.31	0.27	0.2
FRICTION ANGLE	53	43	50

Table 3.3.1.1 Material Properties of the rock types used in the tests

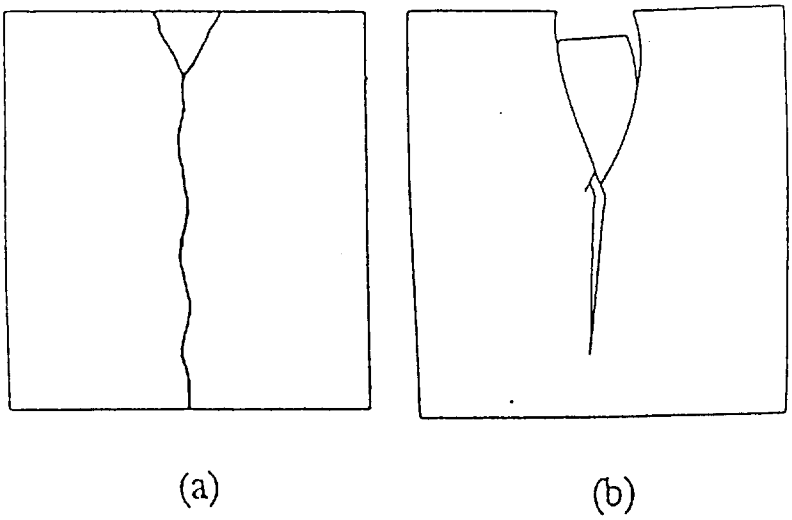

Figure 3.3.1.8 Fracturing in unconfined solid sandstone (a) lab. test (b) numerical model

Confined tests

In this series, the sandstone specimens were enclosed in 4 mm thick steel tubes. The confining stress build up during testing was monitored by strain gauges placed on the outer surface of the steel tubes.

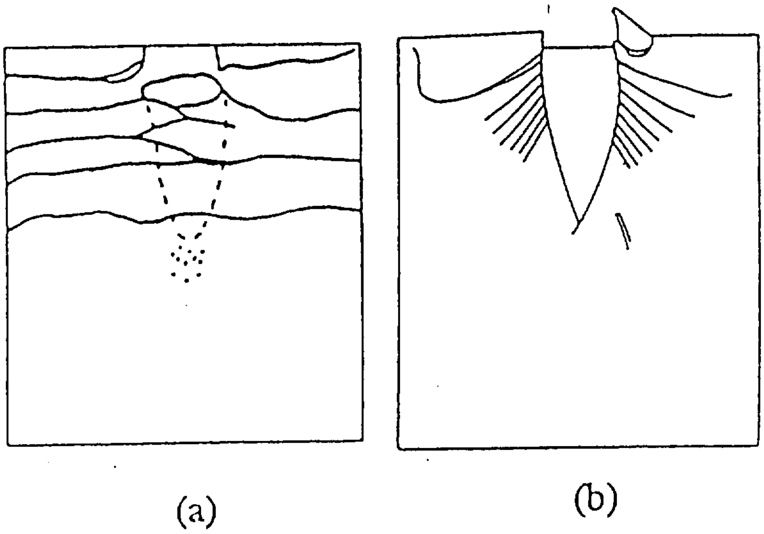

Figure 3.3.1.9 Fracturing in confined solid sandstone (a) lab. test (b) numerical model

The formation of surface parallel extension cracks around the edge of the punch is the most significant difference in this series compared to unconfined tests. Figure 3.3.1.9(a) is a diagrammatic illustration of fracturing developed in the solid specimen and shows repetitive formation of these fractures along the side of the longer but relatively poorly defined cone. The formation of axial tensile fracturing appears to be suppressed under the effect of confining stresses exerted by the steel tube, although an intense crushed region (shown by dotted area in Figure 3.3.1.9(a)) at the cone tip is evident. When a stack of three 20 mm high sandstone disks was placed in the steel tube and loaded by the steel punch, the tensile splitting was absent as shown by the sketch in Figure 3.3.1.10(a). The surface parallel cracks do not seem to propagate across the first interface.

Numerical modelling

Some insights were gained by comparing the results observed in the experiments, to two-dimensional plane strain DIGS simulations of fracturing in test configurations corresponding geometrically to a diametrical section through the samples. Because of the gross nature of this approximation, only three cases are presented and the differences between these results and the corresponding experimental observations are discussed briefly.

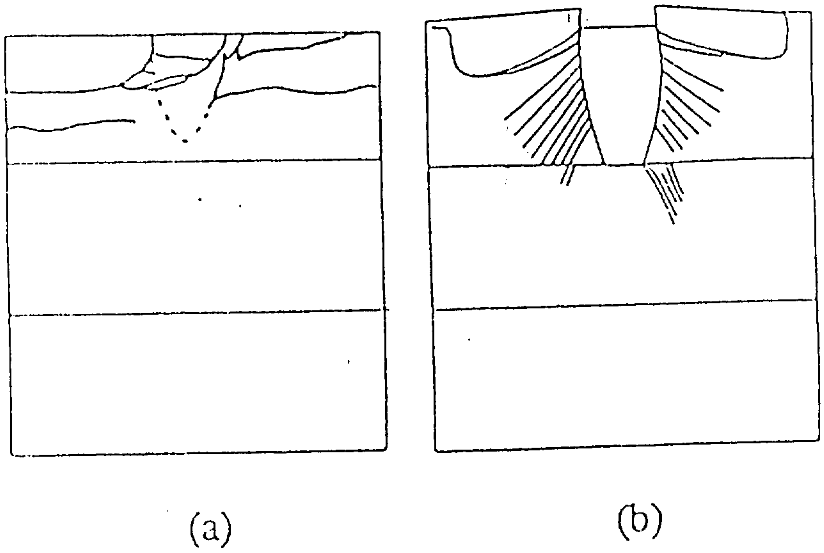

Figure 3.3.1.10 Fracturing in confined layered solid sandstone sample (a) lab. test (b) numerical model

In simulations, cracks are represented as small strain displacement discontinuity elements that are joined end to end in a series of growth steps corresponding to the development of the localized fracture zone. The growth of these cracks or shear bands are determined by two growth rules. Tensile fracture growth from an existing crack tip occurs in the direction in which the stress acting normal to the proposed growth increment is a maximum. (tensile stresses are assumed to be positive.) Shear band development is assumed to occur in the direction corresponding to the maximum incremental strain energy release. This growth rule is tentative and requires detailed experimental justification. (See section 3.1.3)

In the first case the punch loading the unconfined sandstone specimen, as shown in Figure 3.3.1.8(a), is considered. Two shear growth fractures are allowed to initiate below the edges of the region on the sample surface corresponding to the area covered by the punch. This area is loaded uniformly by the stress value corresponding to the maximum observed stress in the physical experiment. The shear fractures are seen to converge in a wedge shaped structure below the punch as shown in Figure 3.3.1.8(b). If a seed point is introduced subsequently to the formation of the shear fractures in the region below the punch, it is found to grow below the wedge structure. The final fracture pattern is qualitatively similar to the observed pattern in Figure 3.3.1.8(a) but shows a marked difference in the wedge angle and extent. The numerical model also ignores the possibility that the tensile fracture below the wedge may form prior to the complete localization of the wedge. The shape of the simulated wedge may differ from the observed shape because of the distinct differences that can arise between an axisymmetric and a plane strain loading geometry as well as inadequacy of the shear growth rule.

The second example attempts to simulate the confined sample depicted in Figure 3.3.1.9(a). In this case, it was assumed that the vertical edges of the sample were not able to move laterally and that no shear traction was imposed on these edges. Shear bands were allowed to initiate from the edges of the punch and tension fractures were allowed to initiate from "seed" points arranged in vertical columns on either side of the punch. The resulting growth pattern is shown in Figure 3.3.1.9(b). Although there are some qualitative similarities to the observed results, it is clear that the orientation of the tensile fractures is not sub-parallel to the free surface as observed in Figure 3.3.1.9(a). The introduction of two horizontal interfaces into the sample is shown in Figure 3.3.1.10(b) and can be compared to the experimental results in Figure 3.3.1.10(a). Each interface is modelled as a sliding crack with zero cohesion and a friction angle of 30 degrees. Figure 3.3.1.10(b) shows that most of the fracturing is confined to the upper layer but the detailed damage pattern is different from the observed fracturing shown in Figure 3.3.1.10(a). Further variations in the boundary conditions, such as a finite friction angle on the vertical interface, and axisymmetric or fully three dimensional crack growth procedures need to be investigated.

Biaxial cell and 3-D tests

In order to carry out 3-D tests on prismatic rock samples, a biaxial load cell shown in Figure 3.3.1.11 was built. The cell can accommodate 80 or 100 mm cubic samples under confining pressure levels of up to 9 MPa. The model is currently being modified to increase confinement

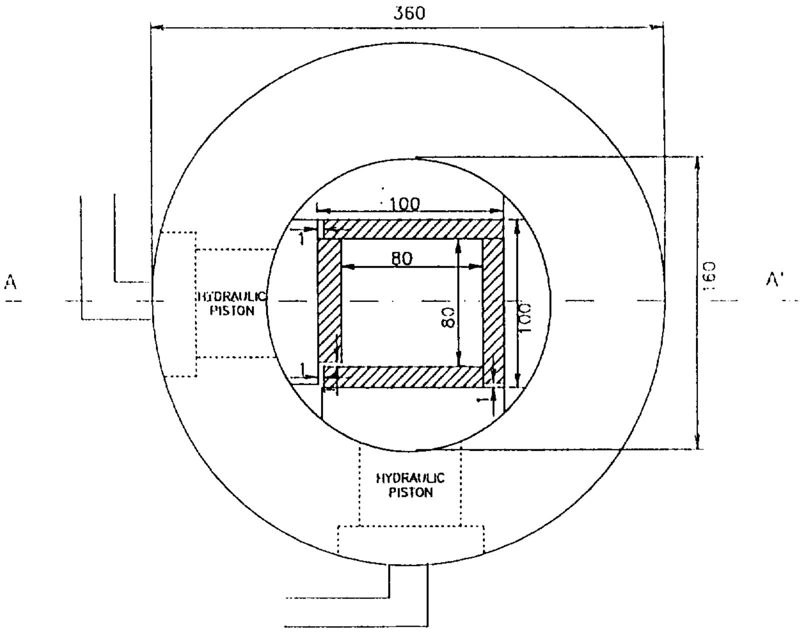

(a) Top View

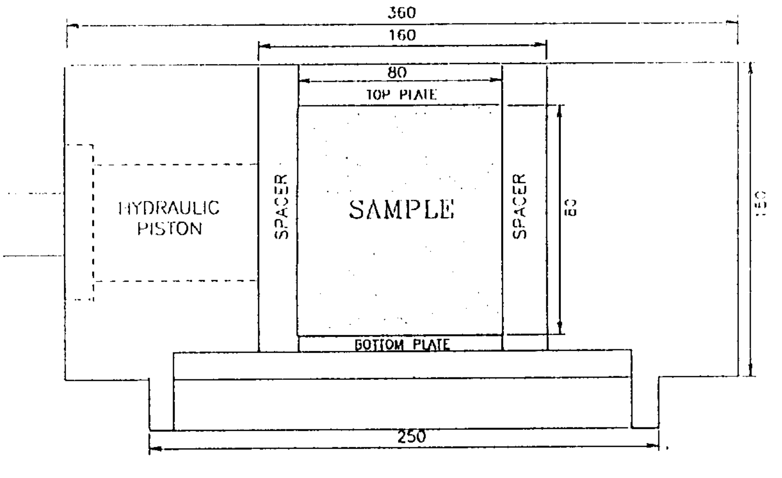

(b) A-A' Section
(units are in mm)

Figure 3.3.1.11 The biaxial frame (a) top view (b) A-A' secti levels to 25 MPa. Models representing strip and square pillars were prepared from quartzite and norite and tested.

The tests in this series have been recently completed and results are currently being analysed. The following is a qualitative description of the tests and results so far obtained.

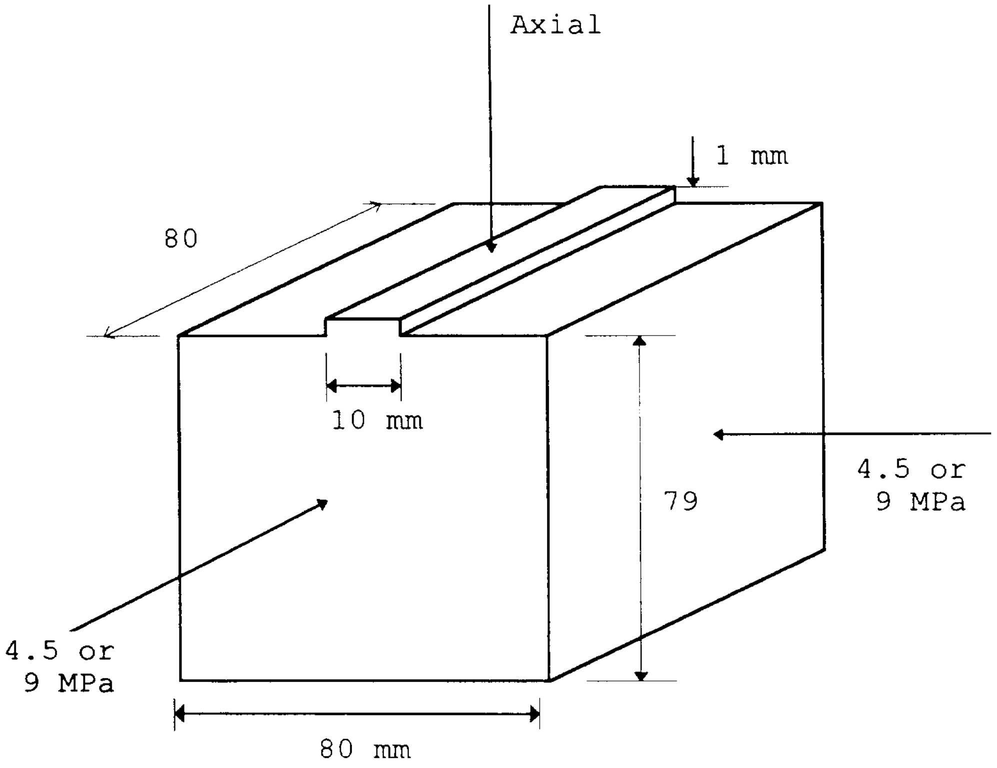

Figure 3.3.1.12 Dimensions of the strip punch tests specimen

Long strip punch tests

Cubical specimens were prepared in such a way that at the top of the specimen a 1 mm in height and 10 mm wide strip was left. The loading direction was through this punch. (Figure 3.3.1.12). Stearic acid was applied to all sides of the specimen which were in contact with the cell as the friction reducer. Two different levels of confinement were applied: 4.5 MPa and 9 MPa.

The fracture pattern obtained from the 4.5 MPa confinement case is shown in Figure 3.3.1.13 for which the failure stress was recorded to be about 490 MPa. The cone width is the same as the punch width of 10 mm. Unlike axisymmetric tests carried out previously, the cone height is greater than the punch width and corresponds more closely to the plane strain numerical simulation shown in figure 3.3.1.9b. The stress-strain curve of the tests, contains two peak points, as seen in Figure 3.3.1.14.

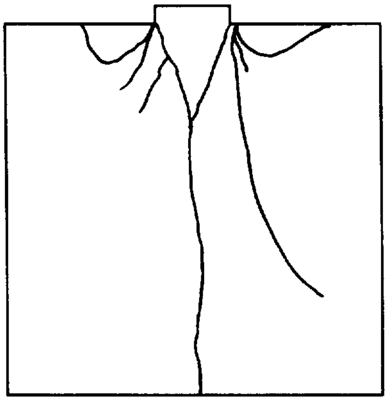

Figure 3.3.1.13 Main fracture pattern of strip punch test (at point C of Figure 3.3.1.14)

Incremental loading

To see the sequential growth of fracture, tests with different loads levels were conducted. As for the first case, the test was stopped at the bottom of the first peak, which is point B in Figure 3.3.1.14. The fracture pattern observed is given in Figure 3.3.1.15.

In the second test, the test was stopped just before the first peak (point A in Figure 3.3.1.14) and the fracture pattern observed is shown in Figure 3.3.1.16. It is interesting to note from the figure that the vertical tensile crack at the centre starts forming before the full formation of the cone

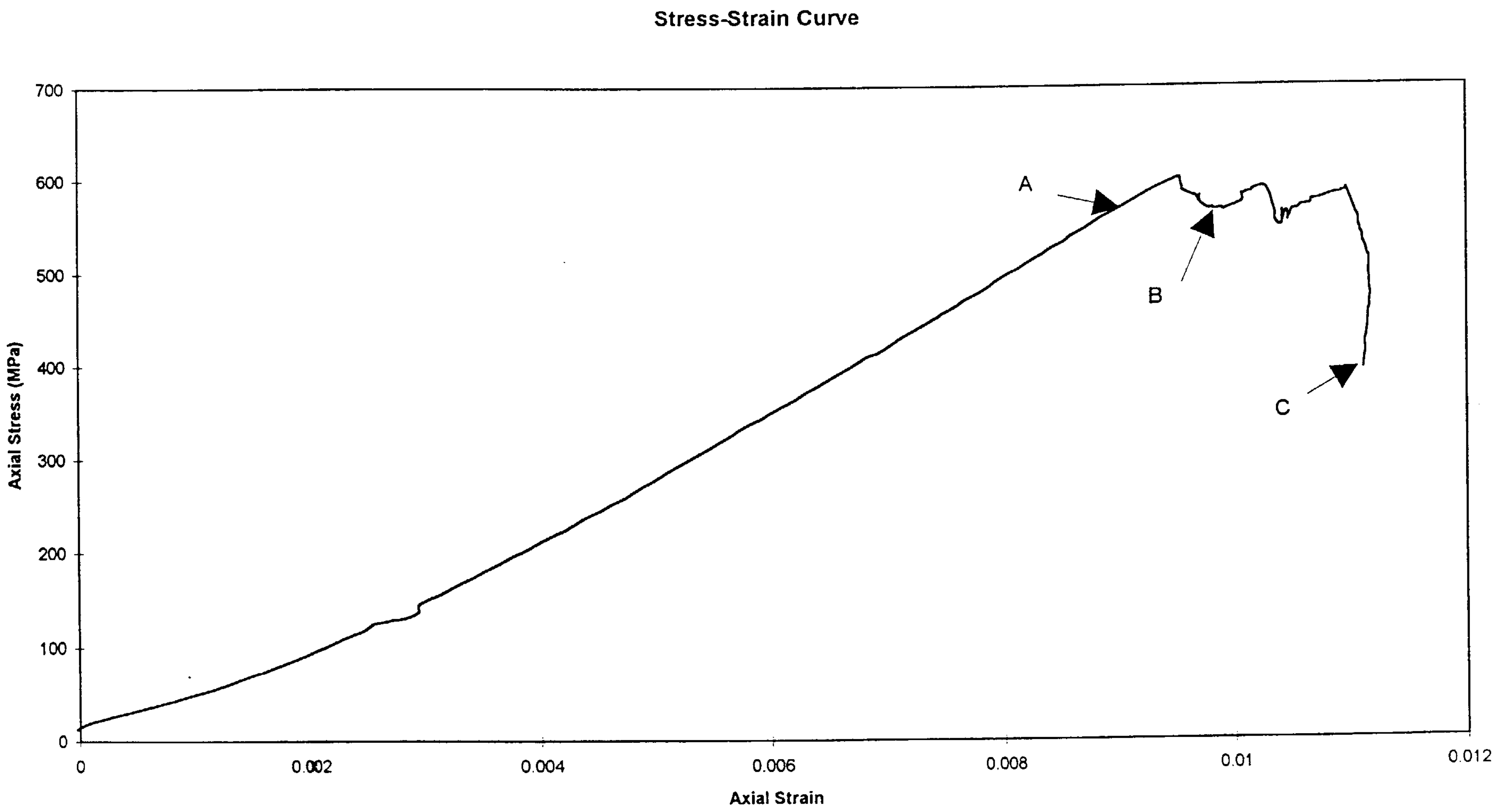

Figure 3.3.1.14 Stress-strain curve of strip punch test

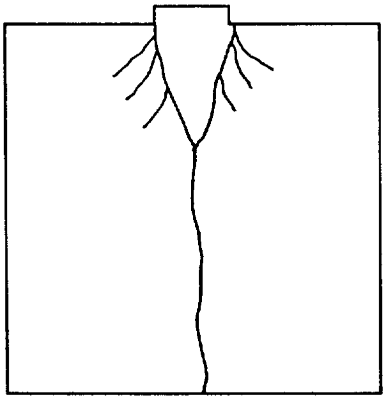

Figure 3.3.1.15 Main fracture pattern of strip punch test (at point B of Figure 3.3.1.14)

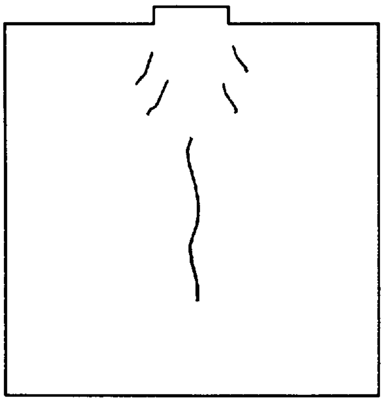

Figure 3.3.1.16 Main fracture pattern of strip punch test (at point A of Figure 3.3.1.14)

Square punch tests

For these tests, samples were prepared to form a square pillar of 1 mm in height and 10 mm in width, (Figure 3.3.1.17). Tested specimens are being prepared for fracture observations

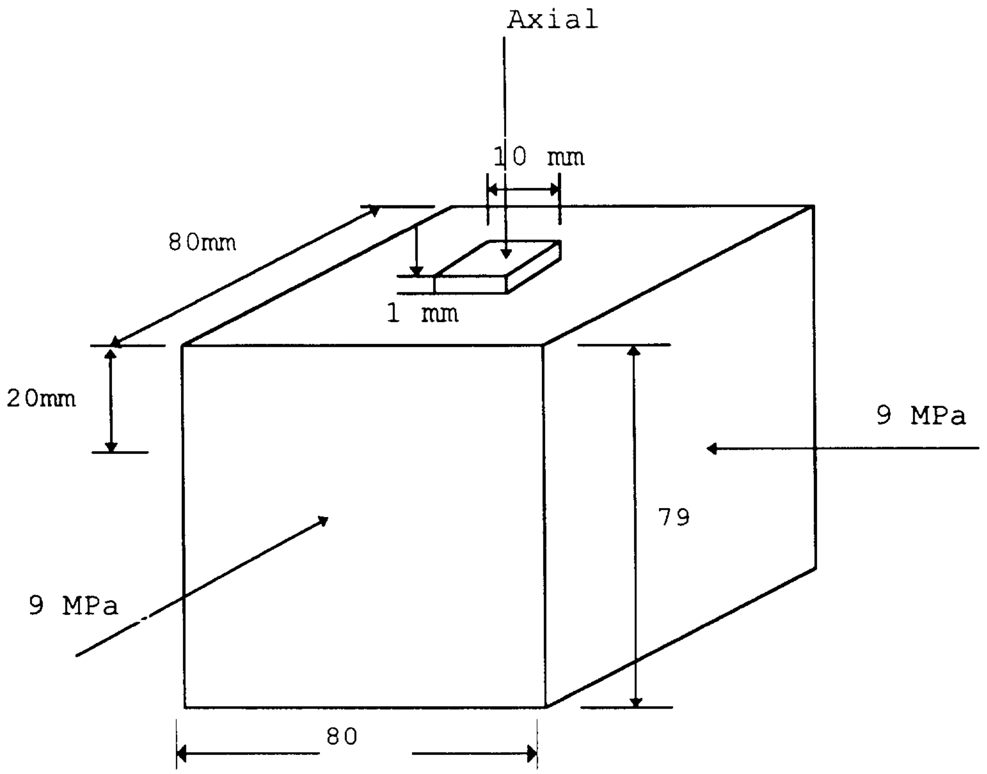

Figure 3.3.1.17 Dimensions of the square punch tests specimen

Strip punch in layered medium

Three types of tests were carried out to study the effect of an interface on the fracture development. In the first test, stearic acid was used between the layers (Figure 3.3.1.18). The failure stress was 412 MPa, compared to 490 MPa for the solid case. In the layered case, although the cone development was obstructed by the interface, the tensile fracture formed fully (Figure 3.3.1.19).

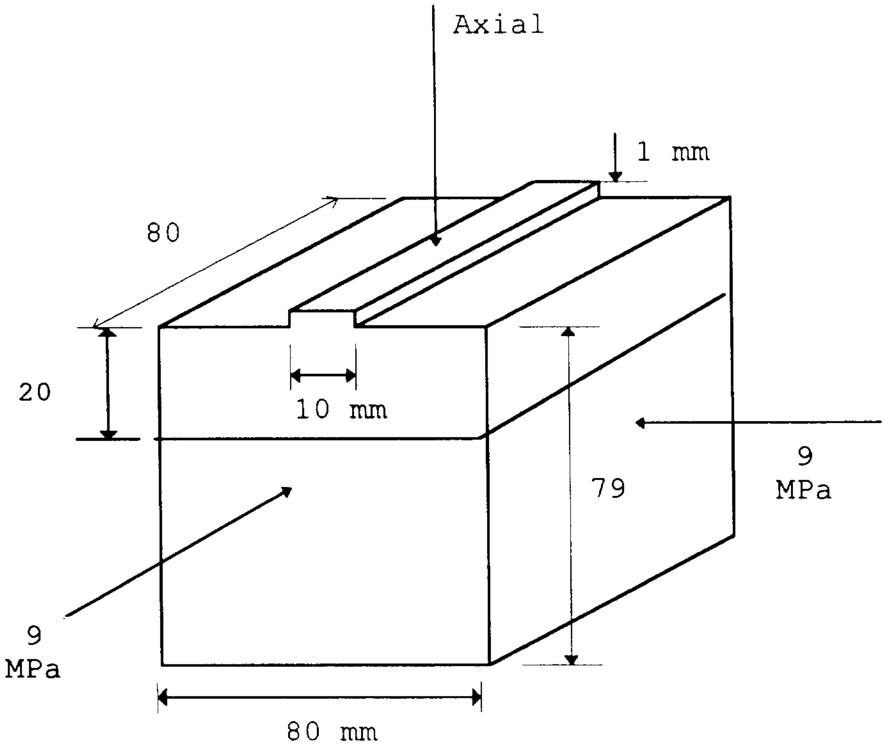

Figure 3.3.1.18 Dimension of the specimen used in the strip punch tests in layered case.

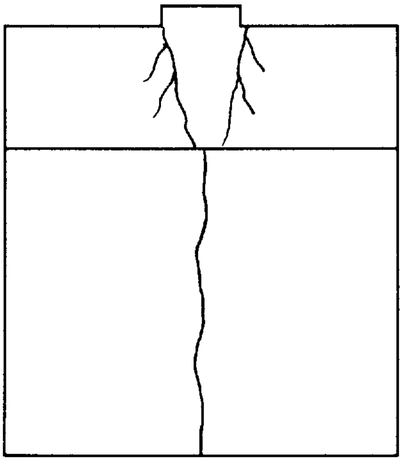

Figure 3.3.1.19 Fracture pattern of strip punch test in layered case with stearic acid

Tests were also carried out without using friction reducers at the layer interface. The failure stress was around 530 MPa, and greater than the stearic acid case. More intense fracturing was observed around the cone, but these fractures were terminated at the interface (Figure 3.3.1.20). The tensile fracture was similar to those observed in the previous tests.

Lastly, one test was carried out using a model with a natural discontinuity The failure stress was recorded as 530 MPa and the resulting fracture pattern is shown in Figure 3.3.1.21.

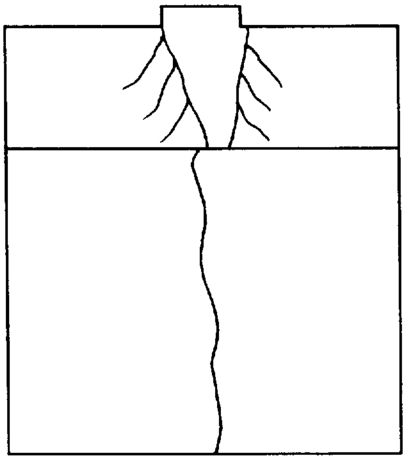

Figure 3.3.1.20 Fracture pattern of strip punch test in layered case without stearic acid

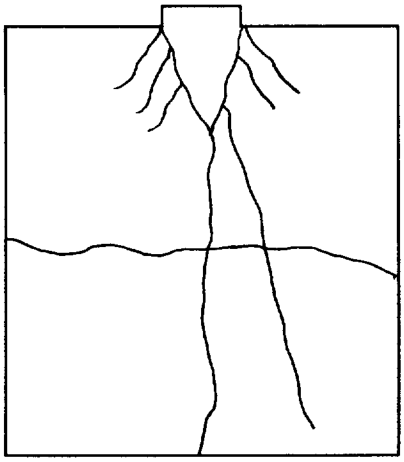

Figure 3.3.1.21 Fracture pattern of strip punch test in layered case with natural discontinuity

Conclusions

- In both confined and unconfined tests, an inverted cone forms under the punch. In the unconfined test, the cone wedges into the sample, axially splitting it into two pieces. This tensile splitting is suppressed in the confined test and the failure stress is increased.

- In the confined tests, surface parallel cracks initiate along the punch edge and these repeat themselves deeper into the specimen.

- The layer interfaces tend to halt the progression of surface parallel fractures

- Numerical simulations of the experimental observations using plane strain geometrical configurations have shown broad similarities to the experimental observations but the detailed orientation of shear bands and extension fractures were not clearly reproduced. It is apparent that it would be easier to model rectangular physical geometries such as the 3-D tests carried out using the biaxial cell or, more challenging, to develop the capability of modeling three dimensional crack growth procedures.

-Accurately scaled models of mining geometries are difficult to prepare and test in the laboratory. However, the models should not be isolated from the actual cases. The most common mine layout configuration includes the stope face and pillars and therefore the model geometry selected was biased towards pillar and advancing stope cases.

Modifications have been made to increase the maximum confinement from 10 MPa to 25 MPa in the triaxial test cell. Numerical modelling is being carried out to simulate the above mentioned tests using DIGS and FLAC computer codes.

3.3.2. PROPAGATION OF FRACTURES FROM AN INTERFACE

In an attempt to understand better the fracture pattern observed in mines, the effect of parting planes on the initiation and propagation of extensional fractures was investigated. An indirect physical method that can be used to study this interaction is to use Brazilian test specimens with a horizontal slit cut in the sample beforehand. In the Brazilian test a circular disc is compressed in a diametral plane between surfaces that apply concentrated loads. A detailed description of the Brazilian test and why it is possible to test the described interaction in this manner can be found in Malan et al. (1994). The computer code DIGS was used to model the observations to gain a better understanding of the underlying mechanisms. However, only the propagation of fractures from an interface was modelled. No attempt was made to model the problem of a fracture approaching an interface.

The experimental tests were conducted on footwall quartzite samples from the Doornfontein gold mine. To examine the effect of an interface, a saw cut was made initially through the slab of rock from which the specimens were obtained. The surfaces of the cut were ground flat and the two pieces of rock were then held together and the circular disc cut. This resulted in a Brazilian sample with a slit running trough the centre of the disc. Various samples with the interface inclined at different angles were tested. Both smooth and irregular interfaces were used. Figure 3.3.2.1 shows a typical fracture pattern for an uneven interface where slip took place. It was found that interface slip is an important mechanism with respect to the violence of the induced fracturing. Samples in which significant slip took place showed much smaller peak failure loads and less rapid load shedding (See Malan et al 1994).

In the DIGS model, the unstressed circumference was specified by a series of crack elements joined end to end in which the crack faces were stress free. The bottom element was fixed and a displacement boundary condition was applied to the top element. The inclined interface was simulated by elements assigned a specific friction angle. Extensile fractures were allowed to initiate from the ends of the interface elements. Figure 3.3.2.2 illustrates the fracture pattern for a sample with an irregular interface at a 20° friction angle. The important point revealed by the modelling was that if slip occurs on discontinuities, local asperities might form nucleation centres for possible fracture initiation.

Conclusions

When using the Brazilian test to examine the interaction between parting planes and fractures, two important observations were made. When slip occurs on the interface, a perturbed stress distribution is induced adjacent to the interface, causing a different fracture pattern to those observed in specimens with no slip. Secondly it was observed experimentally that progressive slip on the interface reduces the amount of stored energy and the recorded stress drop magnitudes. This has important implications for the stability of mining induced fractures ahead of the stope face. For example, artificial loosening of the parting planes could constitute a form of preconditioning leading to improved stoping conditions. The importance of this point warrants further experimental testing and numerical modelling.

References

Malan D.F., Napier J.A.L. and Watson B.P., (1994) Propagation of fractures from an interface in a Brazilian test specimen. *Int. J. Rock Mech. Min. Sci & Geomech. Abstr.* vol. 31. no. 6 pp. 581-596.

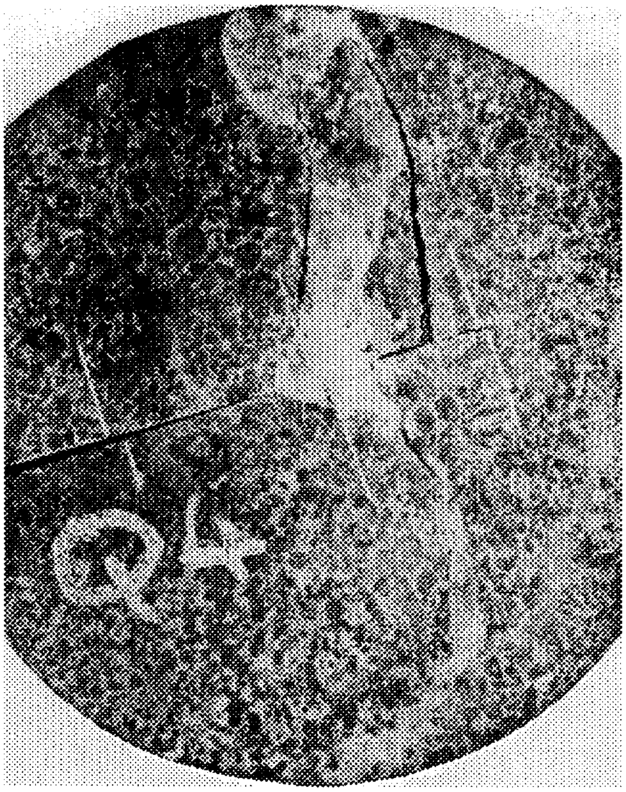

Figure 3.3.2.1 Typical fracturing in a Brazilian test with an inclined interface in the specimen.

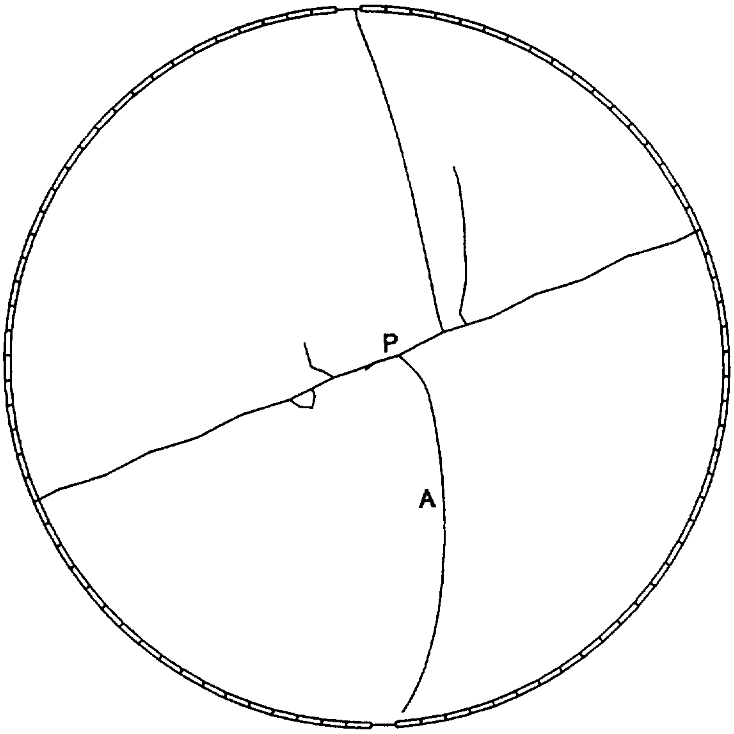

Figure 3.3.2.2 DIGS modelling of fracture growth from an inclined interface in a Brazilian specimen

3.4 NUMERICAL SIMULATION OF PHYSICAL FRACTURING PROCESSES

This section is related to objective 2.2.: "Characterise using physical and numerical modelling, the mechanisms controlling the failure of rock in a stable manner or as a violent release of seismic energy in relation to both the fundamental properties of the rock type and to the geometric characteristics of an excavation and its geological environment" and objective 2.4: "Identify the rock mass and geometric mechanisms controlling the spacing and orientation of fractures near stopes, the stability of the overall fracture zone that is generated and the effects of support and face advance increment size".

Fracturing around highly stressed openings in rock and artificial materials has been investigated previously by many researchers (Carter et al. 1991, Chen and Kemeny 1992, Shen 1993, Gay 1976, Ozbay and Ryder 1989). One issue which is always addressed in one way or another in these investigations is that of the occurrence of so called "secondary" fracturing in rock. Artificial materials such as glass and PMMA do not show these secondary fractures, but only contain the primary, direct tensile fractures.

Fractures around underground excavations have been classified as types I and type II fractures (Brummer 1986). Type I fractures are defined as extension fractures which have aligned themselves perpendicular to the minor principal stress direction during their formation, whereas type II fractures typically show evidence of shear movement along their surface. These type II fractures can therefore be interpreted as shear fractures which are initiated in an all compressive stress field and which assumed an inclination with respect to the major principal stress direction during their formation, or they can be explained as type I fractures which have experienced shear movement due to a rotation of the stress field in reponse to mining processes. Gay and Ortlepp (1979) mention the existence of fracture bands with widths up to 500mm. These fractures are often associated with violent failure and may in fact be related to shear bands as observed in uniaxial and triaxial laboratory experiments. They are not fractures in the true sense of the word, but are localised zones of deformation which, in a bonded granular material, can only occur after sufficient softening in the form of bond breakage.

Secondary fractures which have been observed in laboratory experiments are sometimes referred to as mode II fracturing (Shen 1993) or cracks as having orientations of both type I and type II fractures (Gay 1976). Chen (1992) compares them with 'inclined shear faults', but does not dwell further upon the subject. Referring to previous work of Hoek (1964), Carter et al. (1991) identify a particular class of secondary fracture as remote (extension) fractures. After the formation of primary tensile fractures from an opening in compressed rock, further fracture growth is initiated from areas which are located away from the opening. Ingraffea and Heuze (1980) analysed this first by means of appropriate numerical modelling and found that this type of secondary fracture was effectively an extension fracture which originated from an area where the minor principal stresses are tensile, due to stress redistribution resulting from primary tensile fracture growth. The fact that this type of fracture is not observed in artificial materials such as glass and plastic is explained by the absence of critical flaws in the nucleation zone inside the specimen. Flaws are in fact only present at the surface, due to the process of preparation of artificial materials, while natural rock contains natural flaws which are distributed throughout the volume as envisaged by Griffith. In fact, Griffith postulated that glass would also contain internal flaws, but this is presently doubted based on evidence such as described above.

Vertical splitting of uniaxially loaded rock can also be explained by the unstable growth of secondary fractures from a single flaw, rather than by coalescence of stable primary cracks. This is demonstrated in figure 3.4.1 where primary and secondary fracturing are simulated with DIGS. The primary fracture ceases to grow at a certain distance from the flaw, whereas the secondary fracture becomes unstable and continues to propagate.

This is only valid for an unconfined situation since any confining stress would stabilise the secondary fracture growth. It may be for this reason that experimental results are somewhat inconclusive. As the confining stress is directly controlled by boundary conditions, the slightest imperfection can result in some confinement which could result in a different fracturing pattern. For this reason, the issue of vertical splitting may be somewhat of an academic issue; the very fact that the presence of a minute amount of confining stress can prevent the formation of splitting fractures, indicates that for all practical purposes the formation of (large scale) extension fractures in an all compressive stress field is impossible. This leaves two explanations for the occurrence of large scale fractures in an all compressive stress field. The first is to accept and explain the existence of shear fracturing and the second is to identify mechanisms for the generation of tensile stresses and the subsequent formation of extension

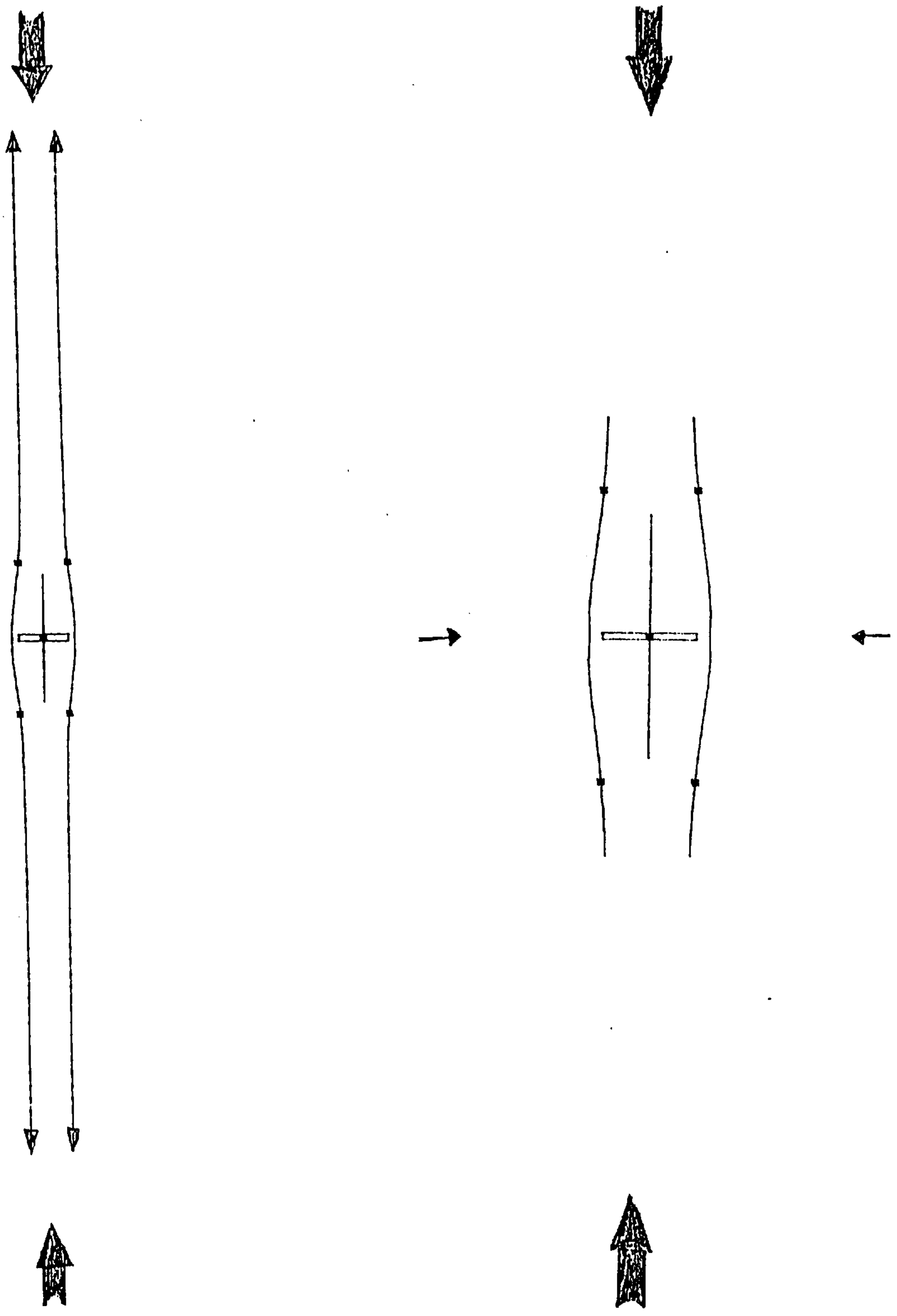

(a) Vertical load = 60MPa
Horizontal load = 0

(b) Vertical load = 60MPa
Horizontal load = 1MPa

Figure 3.4.1 Formation of an unstable axial splitting crack without confinement (a) and formation of a stable crack with a minimum amount of confinement (b) fractures. Tensile stresses are often assumed to be absent and are therefore also assumed to be irrelevant in a typical (deep level) mining environment. The presence of (closed) extension fractures, and especially their spacing, is therefore difficult to explain and is in fact in contradiction with an all-compressive stress field. Attempts to generate shear fractures in laboratory experiments, other than the localised failure zones in a uniform stress field in typical triaxial tests, are inconclusive. The purpose of these experiments is to generate a (shear) fracture from an area of high stress concentrations, similar to a mining excavation. Most experiments of this kind deal with the failure of a bridge zone between openings in specimens which are compressed (Chen et al. 1992, Shen 1993) and are probably associated with an accumulation of damage in a confined zone. Moore and Lockner (1995) analysed the process zone ahead of a shear fracture in a cylindrical specimen of Westerly granite and concluded that after an initial fracturing process, resulting in a uniform distribution of micro fractures with roughly an axial and vertical orientation, a shear fracture is initiated, which generates a process zone of additional microfracturing around its propagating tip. Microfractures within this zone are inclined with respect to the vertical axis and are associated with the stress distribution around the fault tip. Potential linking of earlier formed micro-cracks by these inclined cracks could produce a network of cracks that eventually leads to propagation of the shear fracture. On a macro scale this could be considered a mode II (shear) fracture, although the fracture is formed in a uniform stress field. How the shear fracture initiated without having a fracture tip to enable the formation of a network of micro-cracks is also not raised by Moore and Lockner (1995), but it could be that the additional micro fracturing ahead of the shear fracture tip is just a consequence of the shear fracture propagation rather than a requirement for its formation.

Vardoulakis et al. (1990) constructed a surface instability apparatus in which a cubical specimen of rock is loaded so that one surface is uniaxially loaded while the rest of the specimen is subjected to a (slowly) increasing confinement. A typical result is shown in figure 3.4.2. and it is obvious that some form of shear failure must be present. Stravropoulou (1982) found that the angle of shear fractures with respect to the cylinder axis decreases with decreasing confining pressure. Similar observations have been made by other researchers as well (e.g. Paterson 1958, Tullis and Yund 1977 and Moore et al. 1990). An explanation for these observations may be found in the work of Martin (1993); initial formation of microcracks, which are preferably aligned with the direction of the major principal stress, results in a stable process of tensile (micro) cracking without the introduction of permanent strains. At a stress level which is referred to as 'crack damage stress', residual strains can be

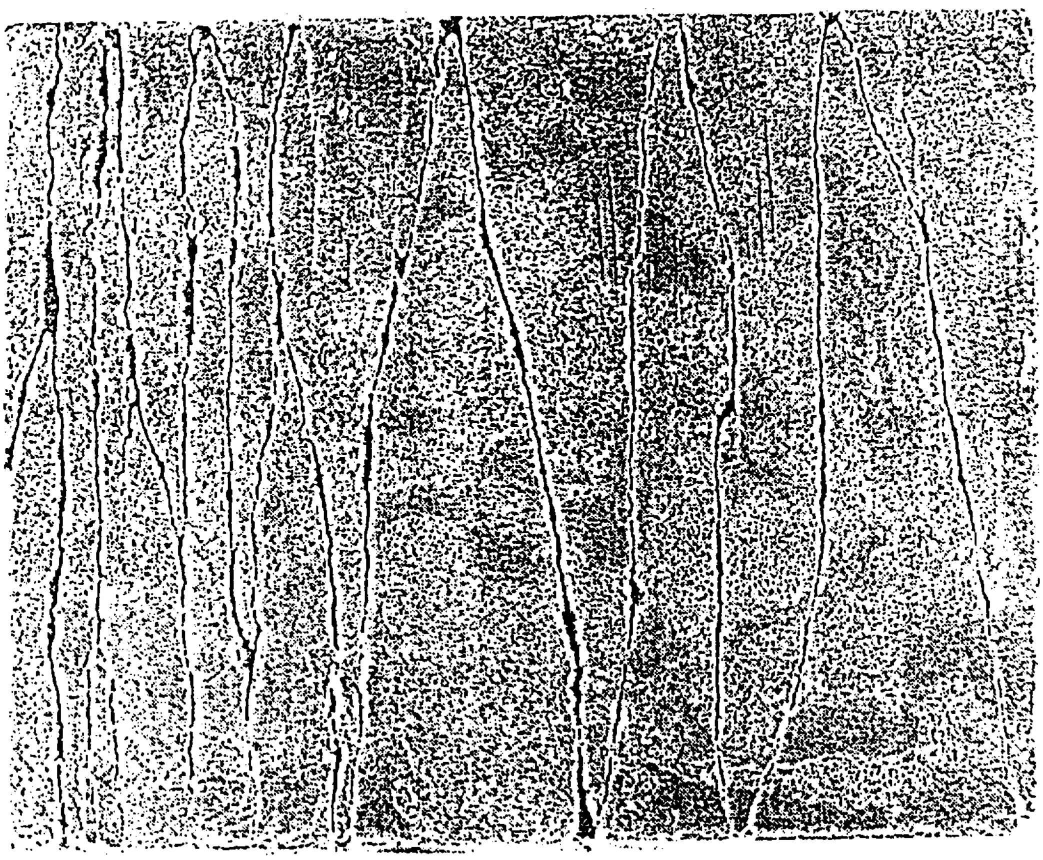

Figure 3.4.2 Fractures observed in the 'surface instability apparatus' (after Vardoulakis et al.)

recorded upon unloading and internal sliding processes, associated with unstable crack growth, can be initiated. At this point friction is mobilised while cohesion is lost. The frictional component is made up of a residual component, which is typical for a particular rock type, and a roughness, or interlocking component. As friction is mobilised, the interlocking is at a maximum and as damage accumulates, the residual friction and minimum cohesion must be approached. This is shown in figure 3.4.3. Typical values of the 'crack damage stress' are around 70% of the short term peak strength as recorded in standard laboratory tests. Very slow loading processes can reduce the peak strength of rock in theory to the 'crack damage stress' and in fact Martin (1993) observed not only a reduction of peak strength in a uniaxially loaded specimen, but also noticed that axial splitting of the specimens did not occur if the loading was applied extremely slowly. Instead characteristic shear planes, formed by the processes of internal sliding, developed. Fast loading apparently does not allow sufficient time for the accumulation of damage necessary to complete the process of shear fracture formation.

The most favourable orientation of a shear band, in terms of the difference between the shear stress and the frictional resistance, is equal to $45^\circ - \phi/2$, with respect to the direction of the maximum principal stress (the Coulomb angle). This equation is still very useful, provided that the appropriate value for the internal friction angle can be obtained. However, the effective friction angle is not a constant, but is directly associated with accumulated damage (figure 3.4.3a). The final orientation of the macro shear fracture will thus strongly depend on the amount of damage and the associated internal friction angle at the time of fracture initiation. The application of a confining stress will probably result in a reduced internal friction angle which could explain the effect of the confining stress on the shear fracture orientation. It should be possible to establish a correlation between damage and internal friction angles for different values of confining stress in a similar way to figure 3.4.3b.

Examples of shear fracturing are demonstrated in figures 3.4.4 and 3.4.5. Both are the resulting fracture patterns from shear fracture growth ahead of an advancing stope face. Figure 3.4.4 was generated with DIGS while figure 3.4.5. was modelled with FLAC (Mohr Coulomb, strain-softening).

Laboratory experiments, designed to reproduce the typical fracture pattern around underground openings, have not been able to produce results similar to the ones in figures 3.4.4 and 3.4.5. which are associated with the wedge pattern of inclined shear fractures initially observed by Roering (1979) and later proposed as a failure mechanism by Brummer (1986).

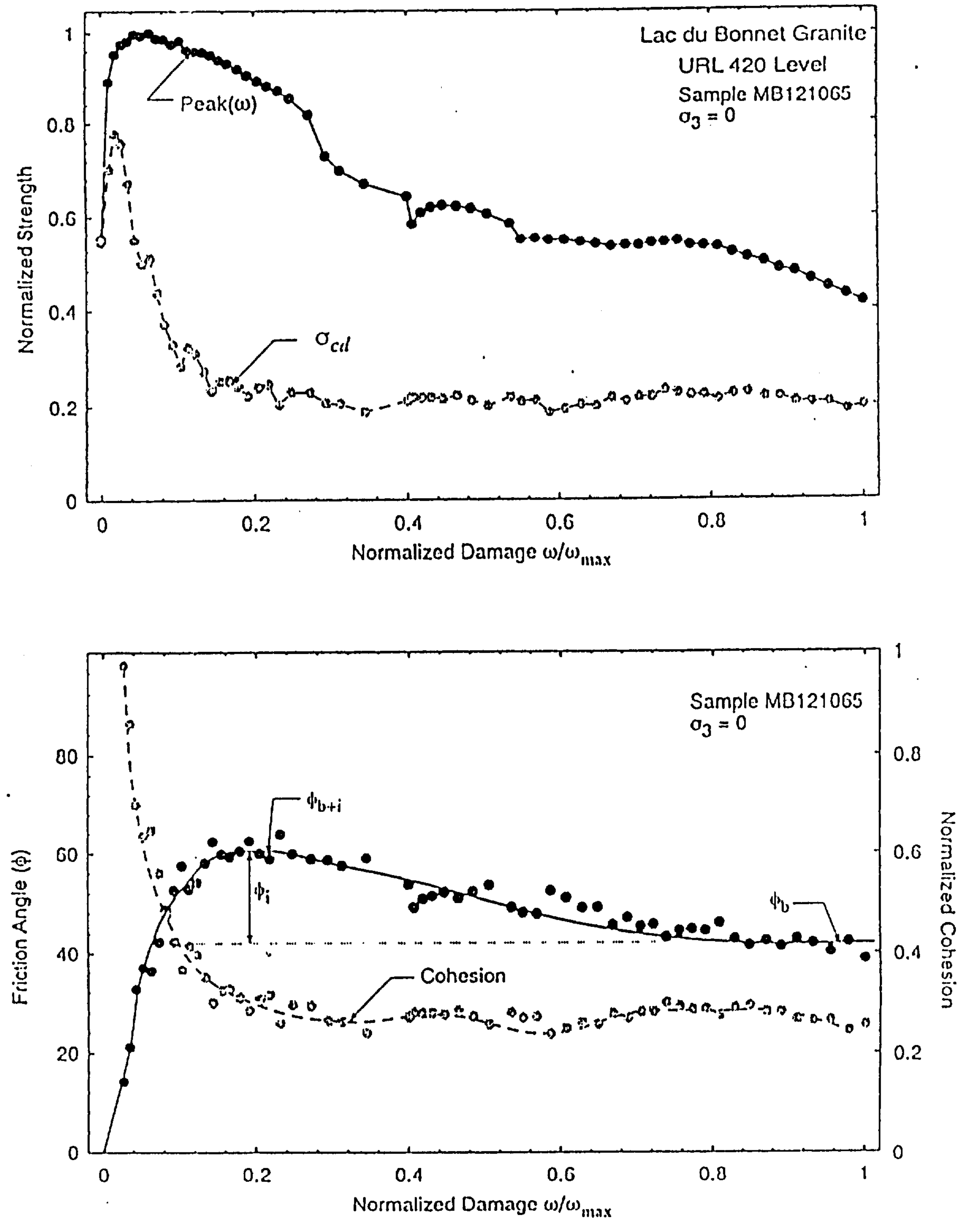

Figure 3.4.3a Mobilisation of friction and cohesion as a function of damage (After Martin 1993)

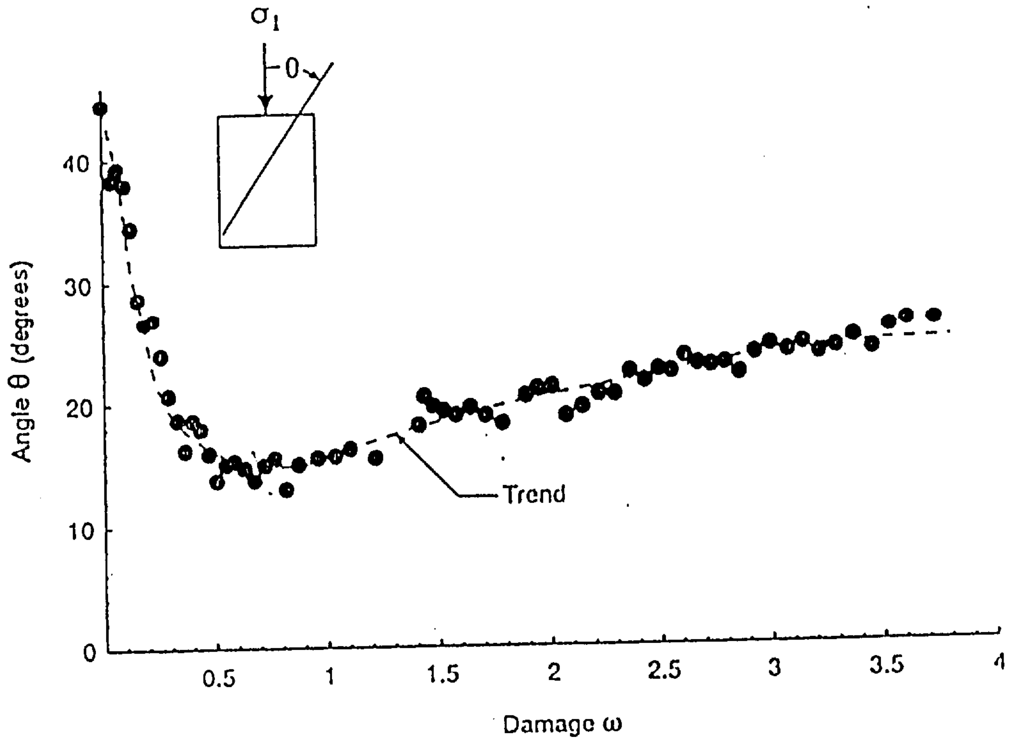

Figure 3.4.3b The angle between the failure surface and the applied stress (σ_1) as a function of damage (After Martin 1993)

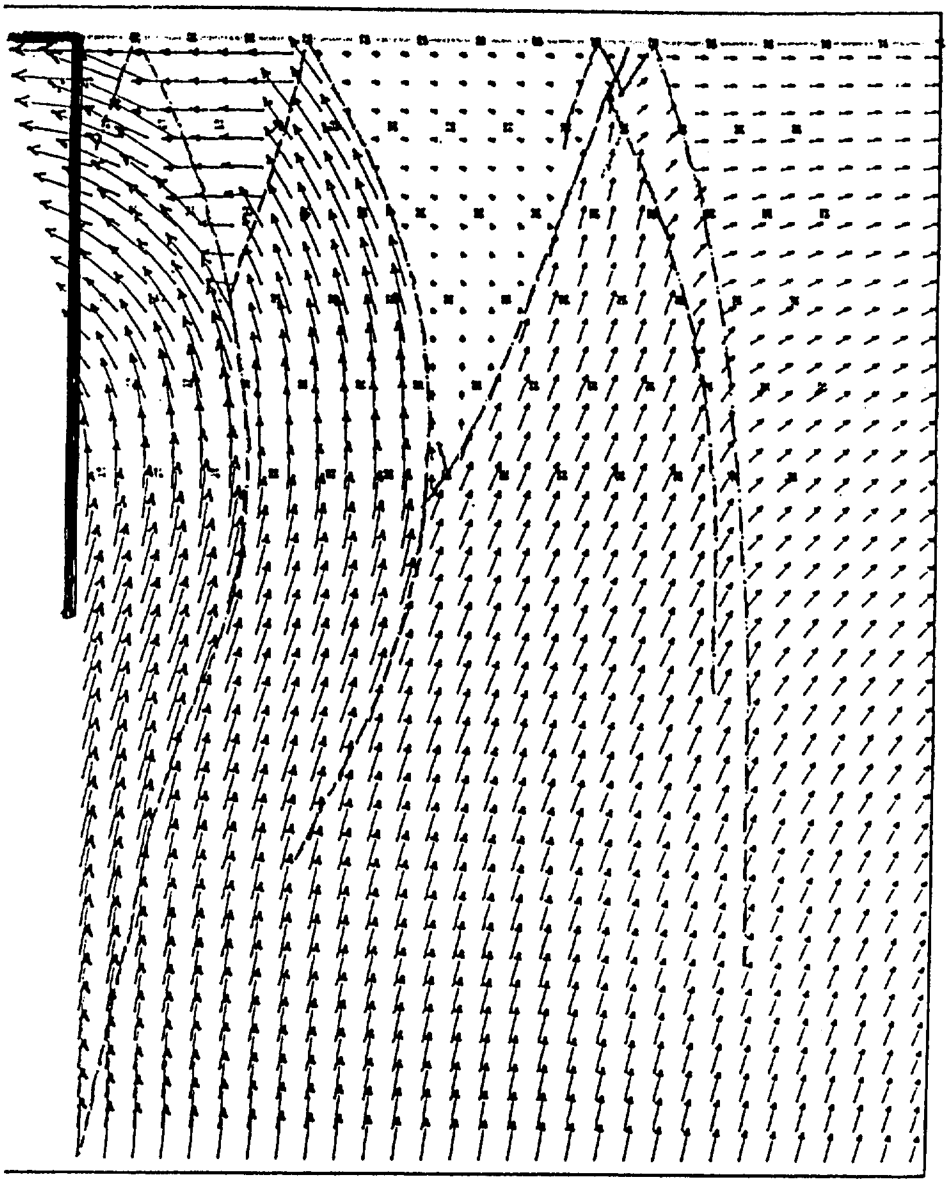

Figure 3.4.4 Pattern of shear fractures ahead of an advancing stope face generated by DIGS

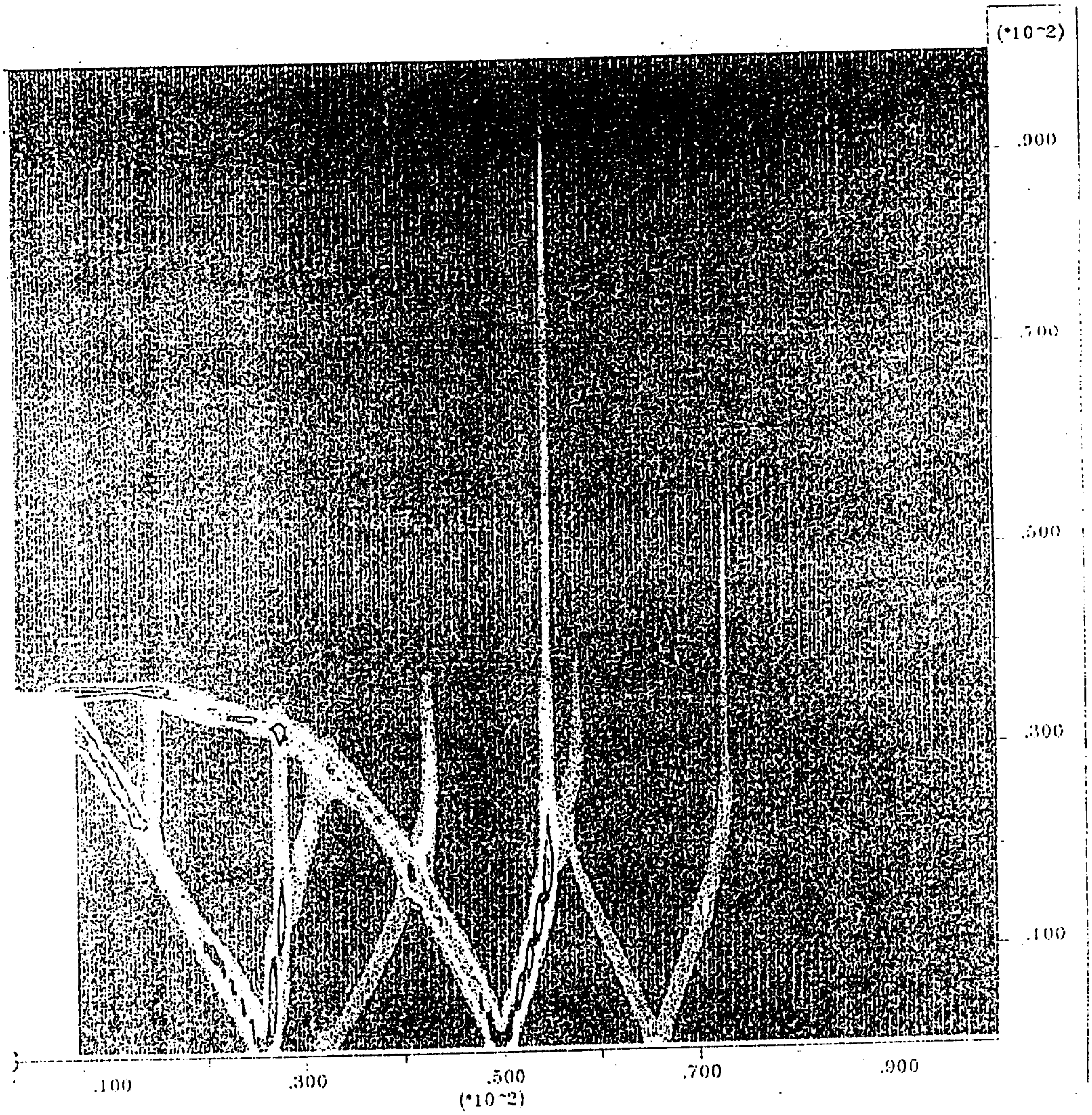

Figure 3.4.5. Pattern of shear fractures ahead of an advancing stope face generated with FLAC

Relevant laboratory experiments on cubical specimens have been conducted by Gay (1976) and Ozbay and Ryder (1989). The height of the openings in their specimens was too small however to observe anything other than 'crushing' near the edges of the openings and shear fractures associated with the openings could not be observed. Shear fractures splitting the complete specimen could be observed towards the end of the tests, but were related to the ultimate failure of the specimen as a whole, rather than controlled by the stress concentrations around the openings. The only large scale fractures which formed in these experiments and which could be related to the influence of the openings, were primary and secondary extension fractures. Figure 3.4.6 shows typical laboratory results and figure 3.4.7. shows modelling results from DIGS. From the modelling results it can be appreciated that the fracture pattern is very sensitive with respect to the ratio of horizontal to vertical stresses (K-ratio). Most of the laboratory experiments were conducted under uniaxial stress conditions, while those which were subjected to biaxial stress conditions only experienced maximum effective K-ratio's of approximately 0.4. As typical K-ratio's in deep level South African goldmines range between 0.5 and 1.0, the resulting fracture patterns may not be representative, because the maximum confining stress which could be applied was limited to approximately 40 MPa. In all these experiments no out of plane load was applied and fractures splitting the specimen perpendicular to the out of plane (minor principal stress) direction could be observed. To avoid these limitations in future a loading rig which allows for true polyaxial loading with a minimum pressure in any direction of 120 Mpa has been constructed.

To explain the formation of large scale fractures that result from tensile stresses it is necessary to identify the origin of such tensile stresses. Around a rectangular opening in unfractured material, tensile stresses are readily formed in a zone above and below the opening. This is similar to the situation in figure 3.4.7. Microflaws are responsible for the generation of microcracks in the same way as are macro flaws for the formation of macro fractures. The stope itself is a macro flaw, but additional flaws in the form of joints, faults and bedding planes are also often present. These form natural weaknesses which will initiate the failure (fracturing) process by offering the least resistance. The formation of extension fractures and associated widening of the effective stoping width is demonstrated and described under 4.4. Another potential candidate for the induction of tensile stresses is the formation of a

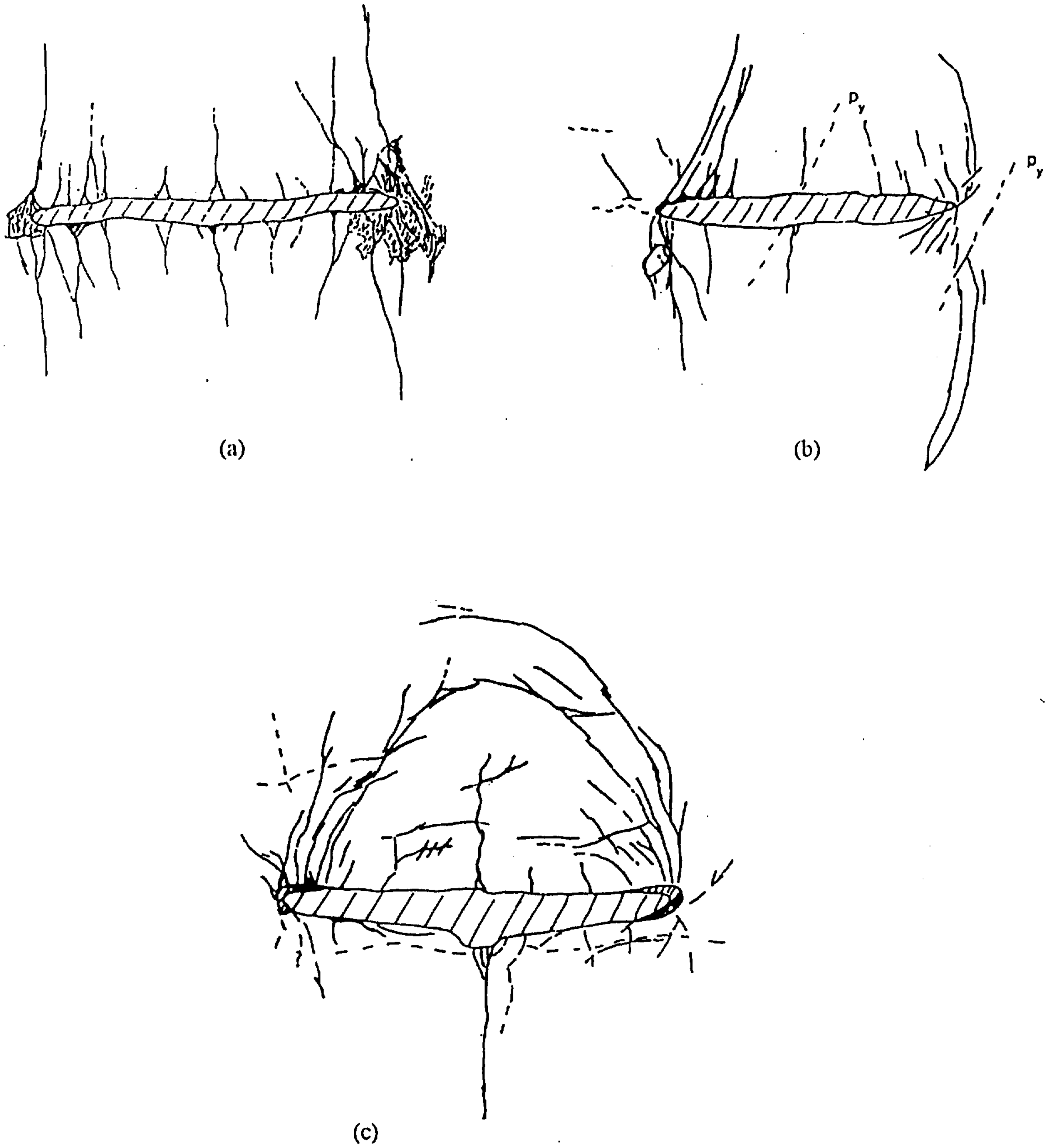

Figure 3.4.6 Fractures around opening in sandstone blocks subjected to biaxial loading (After Gay 1976)

a) uniaxial loading (surface of specimen)

b) $\sigma_H/\sigma_V \approx 0.2$ (surface of specimen)

b) $\sigma_H/\sigma_V \approx 0.5$ (centre of specimen)

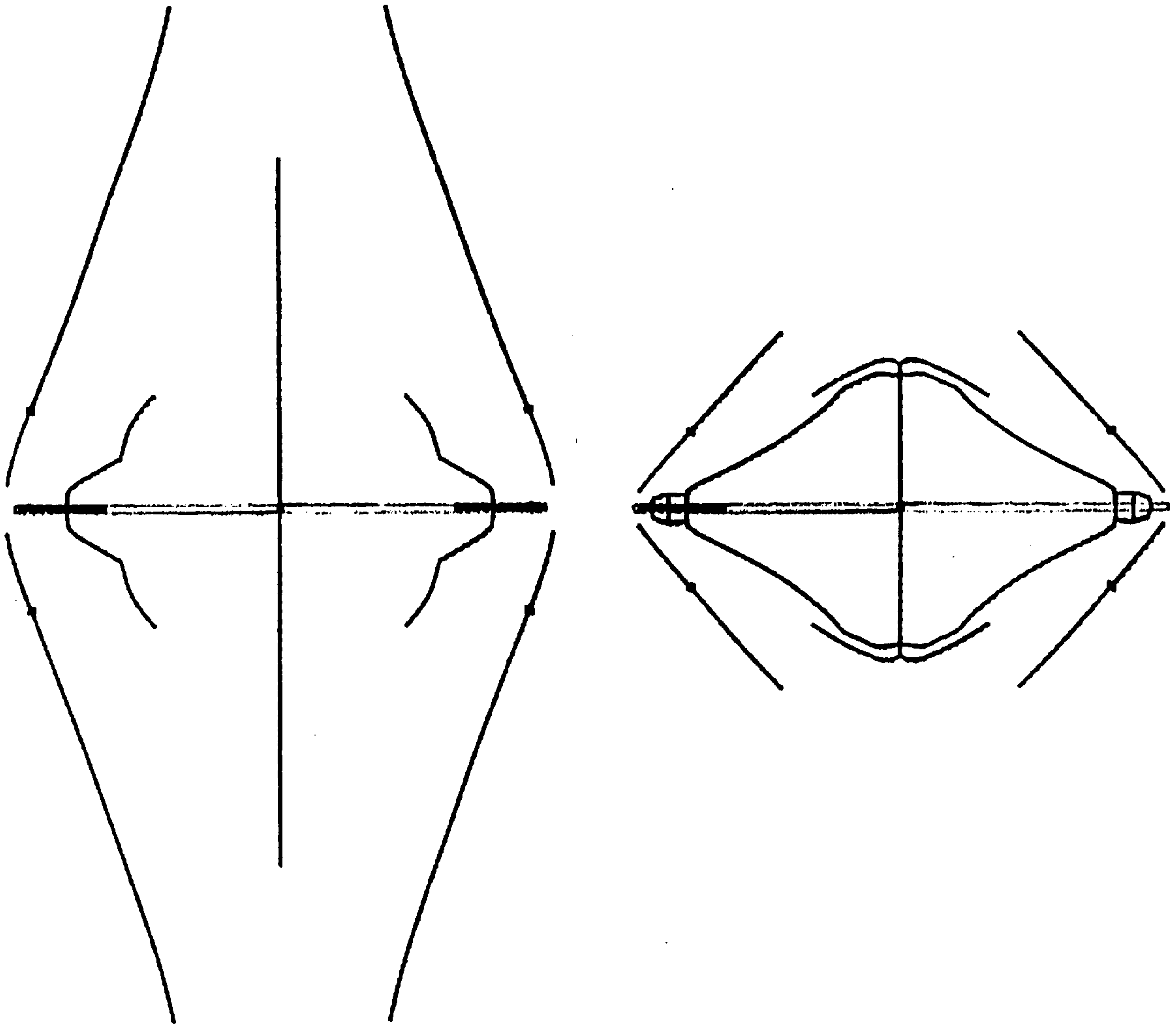

(a) K = 0.1

(b) K = 0.4

Figure 3.4.7. Pattern of tensile fractures around an opening simulated with DIGS

localised 'crushing' zone. The formation of crushing fractures was first observed by Lajtai (1974) and although that may have been an exceptional case, the presence of crushing zones is often observed in laboratory experiments. Figure 3.4.8 shows the fractures around a hole in a uniaxially loaded specimen of Timeball Hill quartzite. The primary and secondary fractures, which have been described earlier, can be observed, as well as an area of intense fracturing in the sidewall of the hole. This 'spalling' zone contains large scale fractures and a small zone of intense damage, conveniently referred to as a crushing zone. This crushing zone is assumed to have a reduced resistance against deformation and affects the stress distribution in such a way that tensile stresses are induced which allow for the generation of the large scale extension fractures in the side wall. This process has been modelled and is also described in section 4.4. Crushing (failure in compression) is not considered to be a failure mechanism in fracture mechanics but the influence of crushing on fracturing in rock is extremely relevant.

Another mechanism which could result in the induction of tensile stresses is plastic shear deformation. Figures 3.4.9a and b and 3.4.10 show two examples of the formation of a tensile region within a shear band. The formation of an en echelon set of extension fractures within the shear band is demonstrated in figure 3.4.10. This last mechanism is based on a ductile-brittle transition of the material. Evidence for these features can be found in the shear test on concrete by Davies (1991) for instance (figure 4.2.9b), and in the literature on faults, where the echelon fractures are referred to as Riedel fractures.

Figure 3.4.8 Fracturing around a hole in a large specimen of Timeball Hill Quartzite

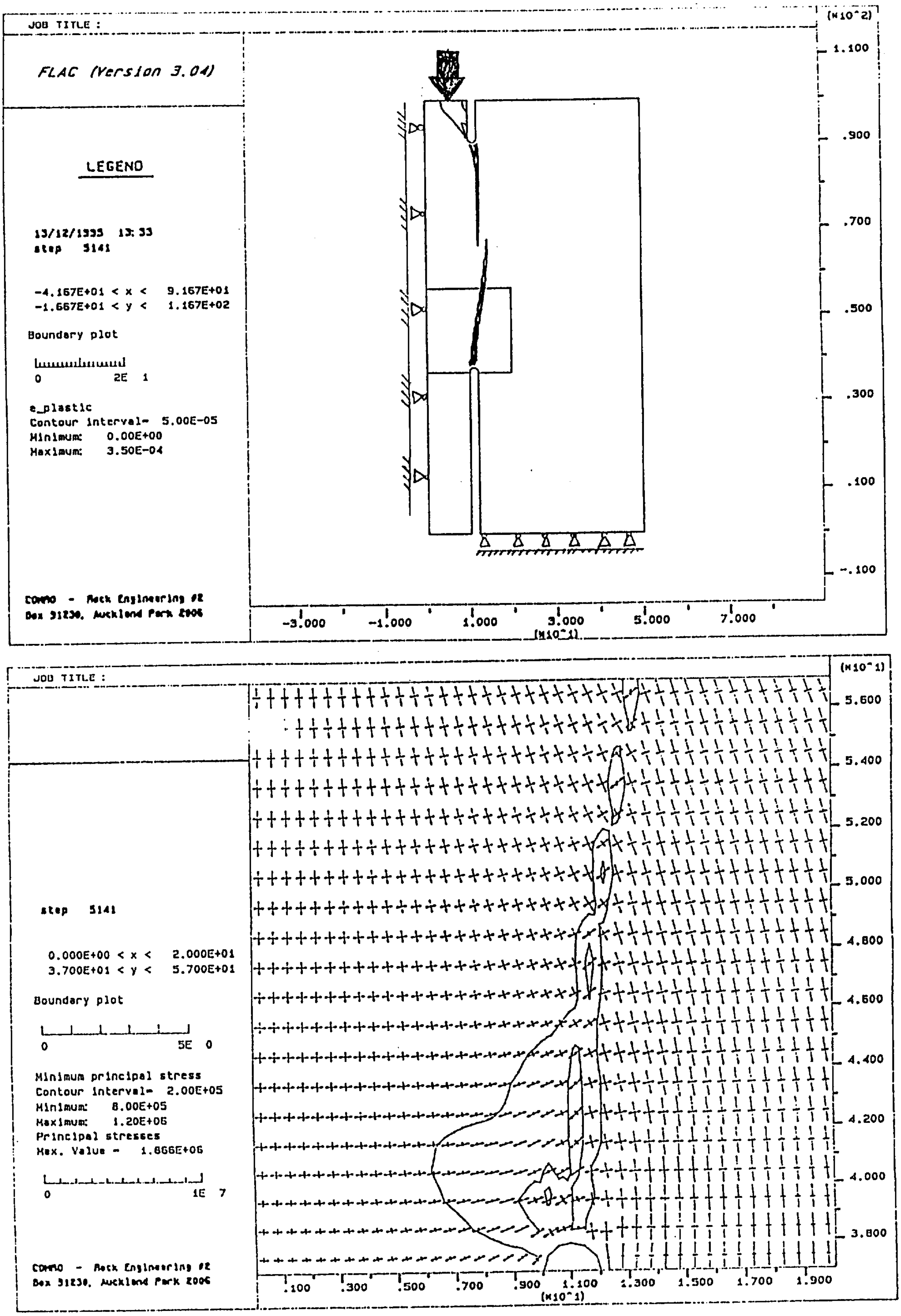

Figure 3.4.9a Development of a shearband with internal tensile stresses developed due to plastic straining (FLAC)

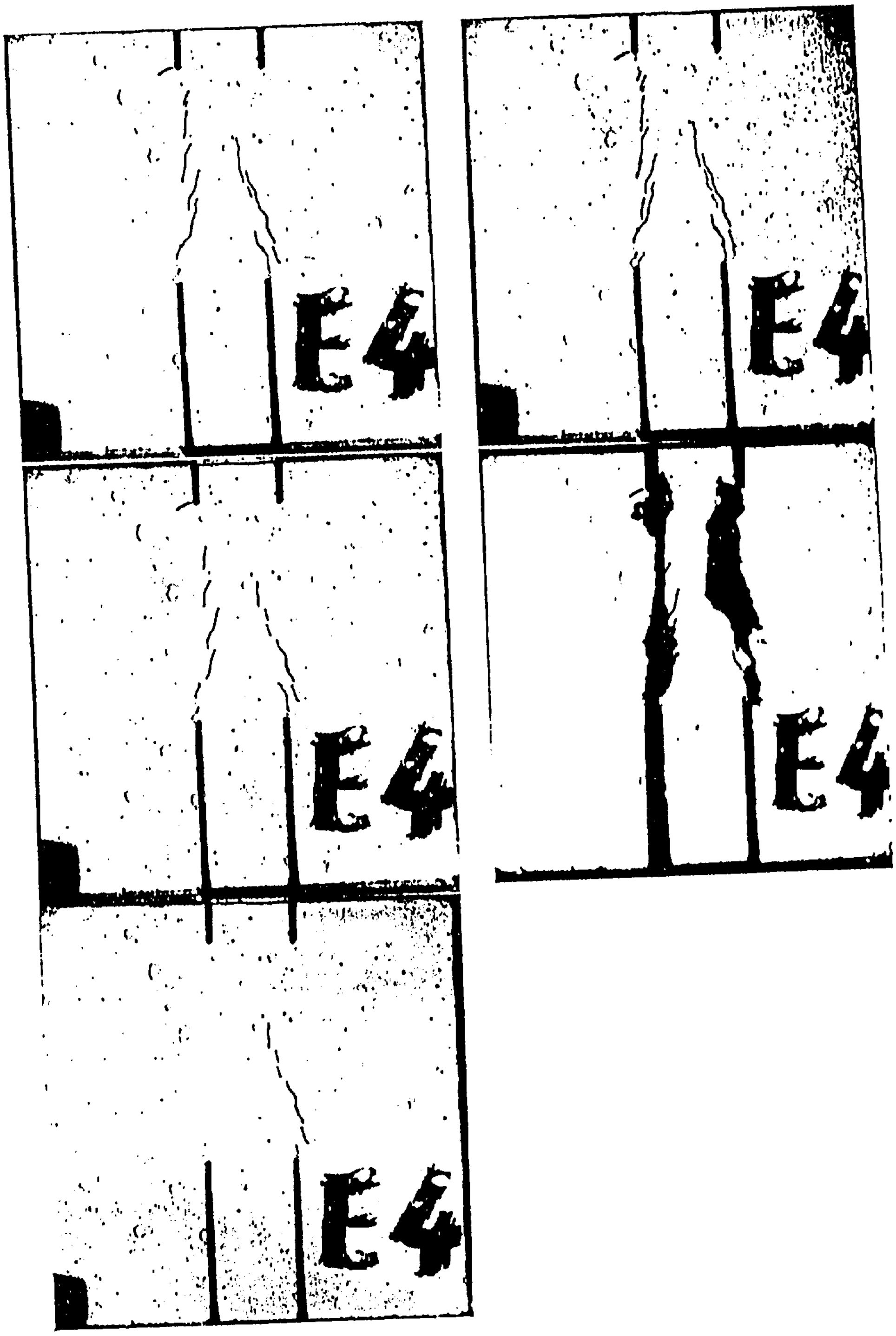

Figure 3.4.9b Fractures in a shear experiment on concrete (after Davies)

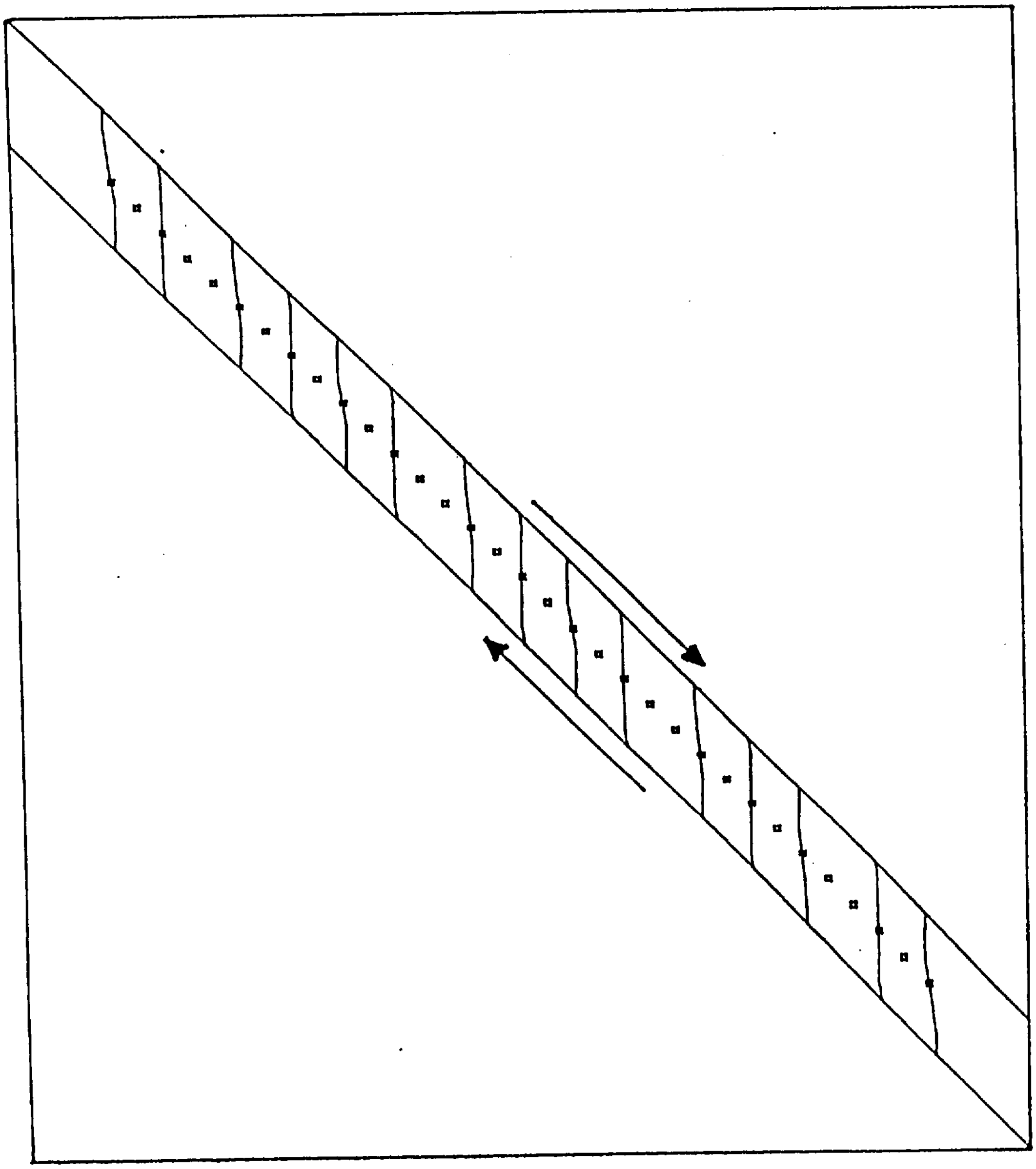

Figure 3.4.10 En echelon formation of tensile fractures due to shear deformation of a shear band; ductile - brittle transition (DIGS)

Conclusions

Internal flaws are resposible for the initiation of fractures inside natural rocks; artificial materials such as glass and plastic only contains surface flaws and can therefore not produce so called 'secondary ' fractures.

Large scale extension fracturing is impossible in an all-compressive stress field, but is in theory possible in a perfect uniaxial stress field in rock containing micro flaws.

The orientation of a shear fracture depends on the amount of damage and the associated internal friction angle at the time of fracture localisation. Internal friction angle is not a constant material property, but is related to internal damage.

A localised crushed zone induces tensile stresses, which subsequently initiate tensile fracturing. Slabbing and spalling are simulated as a result of this combined mechanism.

A ductile-brittle transition has been used as a mechanism for the formation of en echelon tensile fracturing.

References

Brummer R.K. (1986) Fracturing and deformation at the edges of tabular gold mining excavations and the development of a numerical model describing such phenomena. PhD Thesis, Rand Afrikaans University, Johannesburg

Carter B.J., Lajtai E.Z. and Petukhov A. (1991) Primary and remote fracture around underground cavities. Int. J. Numerical and Analytical Methods in Geomechanics, Vol. 15, pp. 21-40

Chen G., Kemeny J.M. and Harpalani S., (1992) Fracture propagation and coalescence in marble plates with pre-cut notches under compression. Proceedings of fractured and jointed rock masses, Lake Tahoe, California

Davies J. (1991) Study of shear fracture. Proceedings .... pp. 438-447

Gay N.C., (1976) Fracture growth around openings in large blocks subjected to uniaxial and biaxial compression. Int. J. Rock Mech. Min. Sci., Vol. 9, pp. 231-243

Gay N.C. and Ortlepp W.D. (1979) Anatomy of a mining-induced fault zone. Bull. Geol. Soc. Am., Vol. 90, pp. 47-58

Hoek E., (1964) Rock fracture around mining excavations. Proceedings fourth international conference on strata control and rock mechanics, Colombia University, New York, pp. 334-348

Ingraffea A.R. and Heuze F. (1980) Finite element models for rock fracture mechanics. Int. J. Numerical and Analytical Methods in Geomechanics, Vol. 4, pp. 24-43

Lajtai E.Z., (1974) Brittle fracture in compression. Int. J. of Fracture, Vol. 10, pp. 525-536

Martin C.D., (1993) The strength of massive Lac du Bonnet granite around underground openings. PhD Thesis, University of Manitoba, Winnipeg, Canada

Moore, D.E. and Lockner, D.A., (1995) The role of microcracking in shear fracture propagation in granite. *J. Struct. Geol.*, vol. 17, no. 1, pp. 95-114.

Ozbay M.U. and Ryder J.A., (1989) Investigations into foundation failure mechanisms of hard rock squat rib pillars. Proceedings Rock at great depth, Balkema, Rotterdam, pp. 527-535.

Paterson M.S., (1958) Experimental deformation and faulting in Wombeyan marble. Bull. Geol. Soc. Am., Vol. 69, pp. 465-476

Roering C., (1979) Annual report for the Chamber of Mines of South Africa in fulfillment of research grant GTI Po4, Rand Afrikaans University, Johannesburg

Shen B., (1993) Mechanics of fractures and intervening bridges in hard rock. PhD Thesis, Royal Institute of Technology, Stockholm

Stavropoulou V., (1982) Constitutive laws for brittle rocks. PhD Thesis, University of the Witwatersrand, Johannesburg

Tullis J. and Yund R.A. (1977) Experimental deformation of dry Westerly granite. J. Geophys. Res., Vol. 82, pp. 5705-5718

Vardoulakis I., Labuz J. and Papamichos E. (1990) Surface Instability Apparatus. U.S. Patent application pending.

4. APPLICATION OF MODELLING CONCEPTS TO MINING STRATEGIES

The application of modelling concepts to proposing novel mining strategies requires a synthesis of known deformation mechanisms that are characteristic of given geotechnical situations. A number of specific issues have been investigated which will determine the characteristics of the fracture zone. These influences include the effects of blast induced or blast assisted fracturing, the tectonic environment, the effect of creep movements on discontinuities and the mining depth. A basic understanding of the nature of these influences and their mutual interactions is required to allow any form of engineering intervention in the manipulation or control of the stope fracture zone.

The project plan objectives corresponding to enabling output 3 are as follows. Objective 3.1 has been dropped from the work plan for project GAP029 since this is covered by project GAP032, Stope and Gully Support.

Objective 3.1 *Determine important deformation characteristics associated with the interaction of local support units and a blocky hangingwall structure in static and dynamic conditions.*

Objective 3.2 *Explore blast-induced fracturing and preconditioning modelling using fracture propagation and interaction simulations and energy release patterns.*

Objective 3.3 *Investigate simple geological models to gain insight into tectonic stress distributions or variations near geological structures and the potential impact of these on rockbursts and fracture propagation in particular cases.*

Objective 3.4 *Simulate combinations of support and mining strategies that can be used to "engineer" the fracture zone to behave in the most inherently stable manner in particular geological environments.*

Objective 3.5 *Evaluate field observations to confirm potential strategies which could be used to control the characteristics of the fracture zone.*

Objective 3.6 *Investigate qualitative changes in fracture zone stability and extent as the mining depth is increased.*

4.1 GEOLOGICAL MODELS

A significant proportion of rockbursts in South African gold mines are associated with geological structures such as faults and dykes. For instance, in the Carletonville district, 40% of mining is found to take place within 20m of a geological structure and results in 60% of the rockburst activity (Gay 1986). The prediction of the response of a rockmass to a planned mining excavation can be undertaken using numerical analyses, however, the interpretation of the numerical results should take into account that the rock is subject to an initial, possibly complex, stress state.

A study was undertaken for objective 3.3 to investigate the role of geology in altering the tectonic stress field and to determine the implications of non-uniform initial stress fields in numerical analysis procedures (Sellers 1995). A literature review uncovered many numerical models for the formation of rock fabric, sedimentary basins, tectonic movements, faults, joints, dykes and folds although few models placed any emphasis on describing the effect of the geological processes on the initial stress state. Quantitative information about the magnitudes and points of application of the loadings cannot be easily determined or estimated, because of subsequent disturbances.

The geology of the Witwatersrand basin is complex and has been affected by tectonic forces accompanied by sedimentation, erosion, faulting, dyke intrusion, and folding. A proper numerical investigation of the manner in which these processes alter the in-situ stress would involve consideration of elastic - plastic material behaviour, including softening and localisation. The identification of long term changes in the in-situ stress field would require consititutive models for the creep behaviour of the rocks. A complete model to evaluate the stresses within dykes requires a coupled thermo-mechanical analyses of the intrusion processes and consideration of the development of fractures in the surrounding rock.

Measurement of the in-situ stress state is the best means of determining the initial conditions for a numerical analysis. The stress state should be measured in undisturbed ground and variations arising from geological structures must also be determined. The measurement can be accomplished with a variety of devices, although most are based on either the overcoring or the hydraulic fracturing technique. Overcoring techniques actually measure strain changes and are therefore sensitive to the magnitude and anisotropy of the elastic properties of the surrounding material. Hydrofracturing measures stresses directly, but the theoretical assumptions necessary for calculation of the stress magnitudes generally require that the major principal stress is vertical.

In-situ stress results for South Africa suggest that there is significant anisotropy of the horizontal stresses. The measured k ratios vary from 0.3 to 1.0, with an average of about 0.5. The directions of the principal stresses can be estimated from consideration of the existing geological structures or from the direction of breakout in tunnels and orepasses. In the Witwatersrand basin, the major horizontal stress tends to be oriented in a northerly direction. Faulting due to tectonic processes has altered the stress state and the major principal stress is seldom vertical. In the vicinity of a normal fault, the major principal stress will be up to 30° from the vertical. Near reverse and strike-slip faults, the major stress will be approximately horizontal. The intermediate principal stress will lie in the plane of the fault.

A number of 2-D plane strain analyses of a simplified geological situation were performed with FLAC to investigate the effect of different procedures for specifying the in-situ stress state in a numerical analysis. The model consisted of a dense, stiff, elastic, dyke dipping at an angle of 80^0 through a 1km square extent of elastic, rock. The equilibrium stress state, and the horizontal to vertical stress ratio, k, strongly depend on the specification of the initial stress state, the boundary conditions and the dyke interface. The most reasonable estimate of the initial stresses is a linear variation with depth. In an analysis with multiple materials and containing dyke interfaces and faults which can slip, an initial stress state should be specified which is close to equilibrium. In cases where a good estimate of the equilibrium stress state is not easy to calculate, the best approach would be to obtain equilibrium with a uniform material and introduce the other material in subsequent steps, provided that the facility for changing the material properties exists in the analysis package. This procedure has not been investigated for a model containing elastic-plastic materials which may behave differently due to their path dependence.

Stress boundary conditions should not be used when it is expected that the interaction of different material types can introduce additional horizontal stresses. Displacement or velocity boundaries must be placed far from the region of interest. At least five times the largest dimension of the excavation is suggested.

The boundary element analysis of a stope adjacent to a fault using the DIGS boundary element code demonstrated the effect of the k-ratio on the excess shear stress. Lower values of the k-ratio result in higher ESS values and hence a greater potential for seismicity. The conventional estimate of the ratio of horizontal to vertical stress of 0.5 can lead to misleading results. Inclusion of a geological history causing locked-in stresses due to fault displacement significantly increases the ESS values.

Some simple models of a plate of strain softening material with random properties were analysed to investigate fault formation in extensional and compressive tectonic regions. Localised regions of the plastic strain tended to form suggesting patterns of faulting. The major principal stress was rotated about 30° from the vertical by the faulting. The results are however mesh dependent and conclusive analyses should be based on a more rigorous parametric investigation of the material properities.

Conclusions

These analyses have demonstrated that the geological processes can have a significant effect on the in-situ stress state existing in rock. In addition, the boundary conditions and specified initial stress state can cause significantly different results in numerical analyses with path dependent materials and nonlinear joints and interfaces. Thus, in any mining analysis, the in-situ stress state should preferably be obtained from measurements in the region of interest. Special consideration should be given, in numerical modelling, to the anisotropic horizontal stress state in the Witwatersrand basin where the major stress is oriented in a northerly direction. The average horizontal to vertical stress ratio is about 0.5, but the ratio can be as low as 0.3 in the direction of the minor stress. However, more in-situ experimentation is required to provide estimates for the stress state in and around geological features, such as dykes and faults, to assist in numerical analyses where in-situ measurements are not available, or are impractical.

References

Gay, N.C. (1986) Mining in the vicinity of geological structures - an evaluation of the problem. *Mining in the vicinity of geological and hazardous structures,* SAIMM, 1-32.

Sellers E.J. (1995) Modelling of the influence of geology on the in-situ stress state. *CSIR mining technology report.*

4.2 BLAST INDUCED FRACTURING AROUND MINE OPENINGS

This section deals with objective 3.2: 'Explore blast-induced fracturing and preconditioning modelling using fracture propagation and interaction simulations and energy release patterns."

Tunnels developed in highly stressed rock have long been recognised as having an envelope of so-called 'bow wave' fractures around them (figure 4.2.1). Because such fractures are not observed around tunnels in areas which are subjected to lower stresses, it is often argued that these fractures are induced by the static stress concentrations around the tunnel face.

Stacey (1981) and Stacey and de Jongh (1977) analysed the stress distribution around a tunnel face and concluded that the stress levels would be too low to result in fracturing if the Mohr failure criterion was assumed. In order to explain the observed fractures Stacey assumed a criterion which is based on a critical extension strain. Typical values for critical extension strain correspond to stress levels of around 30% of the Uniaxial Compressive Strength (U.C.S.) of rock. It is well known that micro fracturing in brittle rock, loaded in compression, initiates at stress levels far below the final strength, but the macro fracturing as observed around underground tunnels can hardly be associated with such micro fracturing. In fact the extension strain as used by Stacey is equivalent to a criterion based on stresses. Since

$$\varepsilon_3 E = \sigma_3 - \nu(\sigma_1 + \sigma_2) \tag{4.2.1}$$

it follows that:

$$\sigma_1 = -\frac{\varepsilon_3 E}{\nu} + \frac{1-\nu}{\nu}\sigma_3 \qquad if\ \sigma_2 = \sigma_3 \tag{4.2.2}$$

$$\sigma_1 = -\frac{\varepsilon_3 E}{2\nu} + \frac{\sigma_3}{2\nu} \qquad if\ \sigma_2 = \sigma_1 \tag{4.2.3}$$

In the first case the effective friction angle ϕ as used in the Mohr-Coulomb failure criterion can be found from:

$$\sin\phi = 1 - 2\nu \tag{4.2.4}$$

In the second case the effective friction angle is

$$\sin\phi = \frac{1-2\nu}{1+2\nu} \tag{4.2.5}$$

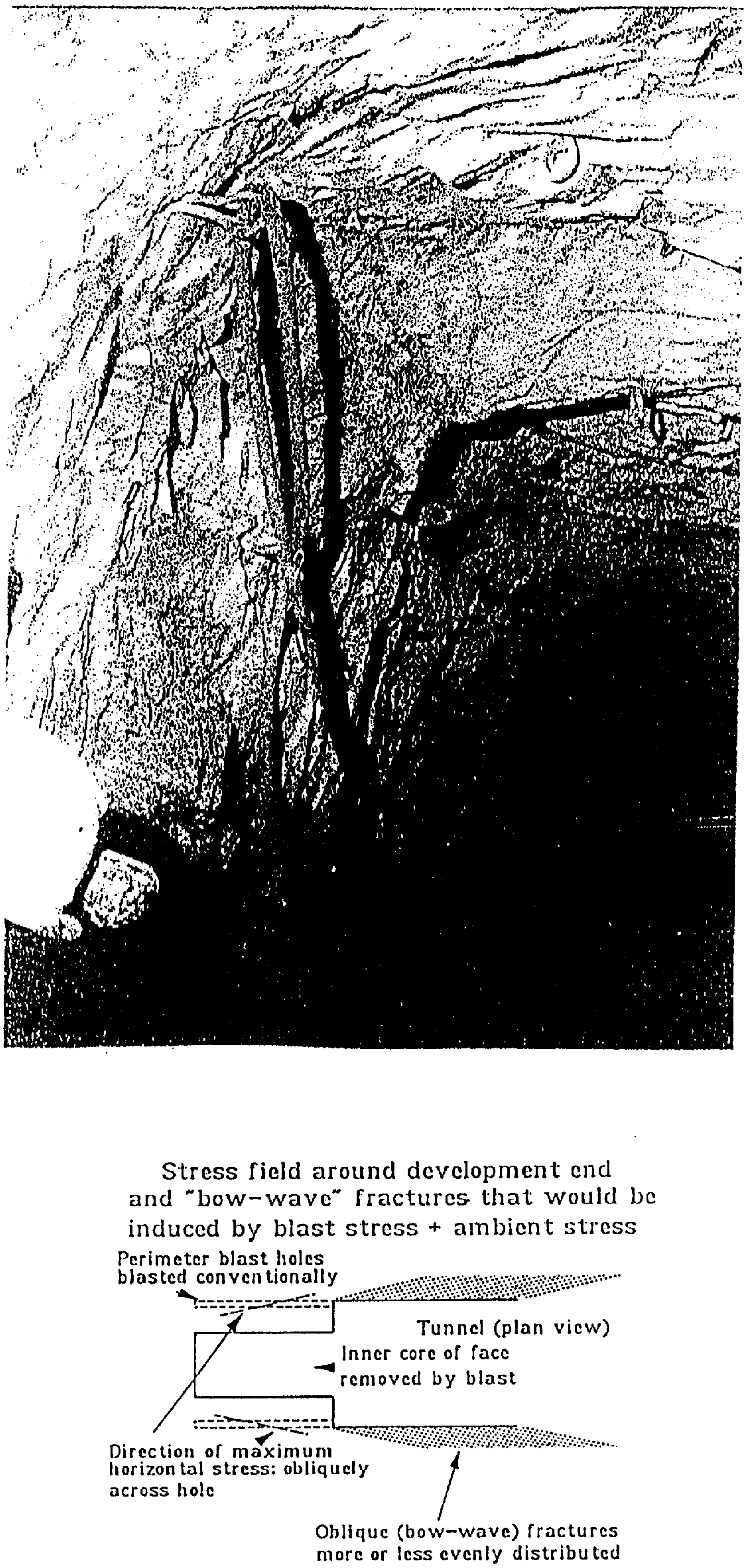

Figure 4.2.1 Bow wave fractures around an advancing tunnel in highly stressed rock

For values of ν between 0.1 and 0.3 ϕ ranges between 53° and 23° for the first case and between 42° and 15° for the second case. The extension strain criterion therefore is in essence not different from the conventional Mohr-Coulomb criterion, except for the fact that the influence of the intermediate principal stress σ_2 is grossly overestimated by the extension strain criterion (and perhaps slightly underestimated in the Mohr-Coulomb criterion?).

In related experiments Carter (1991) found that the initiation of sidewall spalling in laboratory experiments was only observed when the theoretical stresses in the sidewall exceeded the uniaxial compressive strength of the rock by approximately 50%. Such observations are quite common and are explained as scale effects using, for example, a Weibull distribution of weaknesses and/or due to the different influence of the stress gradient on different scales.

An alternative explanation offered by Martin (1993) proposes that stress rotations during the excavation process can be responsible for the onset of failure at stress levels which are far below the laboratory strength of the rock. Although Martin's explanation is specifically related to the process of 'dog-earing' as analysed by his team around the Mine by Experimental Tunnel, it might be of relevance to the fracturing observed around deep level gold mine tunnels and stopes as well. Martin's proposal will be tested and analysed by reproducing stress rotations in a newly designed laboratory experiment which allows for stress rotations in cylindrical specimens. An additional mechanism for reduced strength may be found in the storage of residual elastic strains in rock. This has been proposed by Friedman (1970) who analysed various rock types and demonstrated that the residual elastic strains tend to control the orientation of induced fractures for certain directions of loading.

Although it might be possible that these theories could justify a reduction of critical stress levels to a certain extent, it seems unlikely that such reductions would be as substantial as suggested by Stacey. The results from computer modelling indicate that the (static) stress distribution along a tunnel side wall is as shown in figure 4.2.2. The maximum stress which theoretically can be reached near the tunnel side wall is $3\sigma_1 - \sigma_3$. The maximum stress which can be reached near the corner of the tunnel face and the tunnel wall is close to this value, but values ahead of the tunnel face are much lower and peak values in the tunnel side wall are only reached at a certain distance from the tunnel face. It must be emphasized that these values are reached only at two critical points along the tunnel circumference when the radial stress

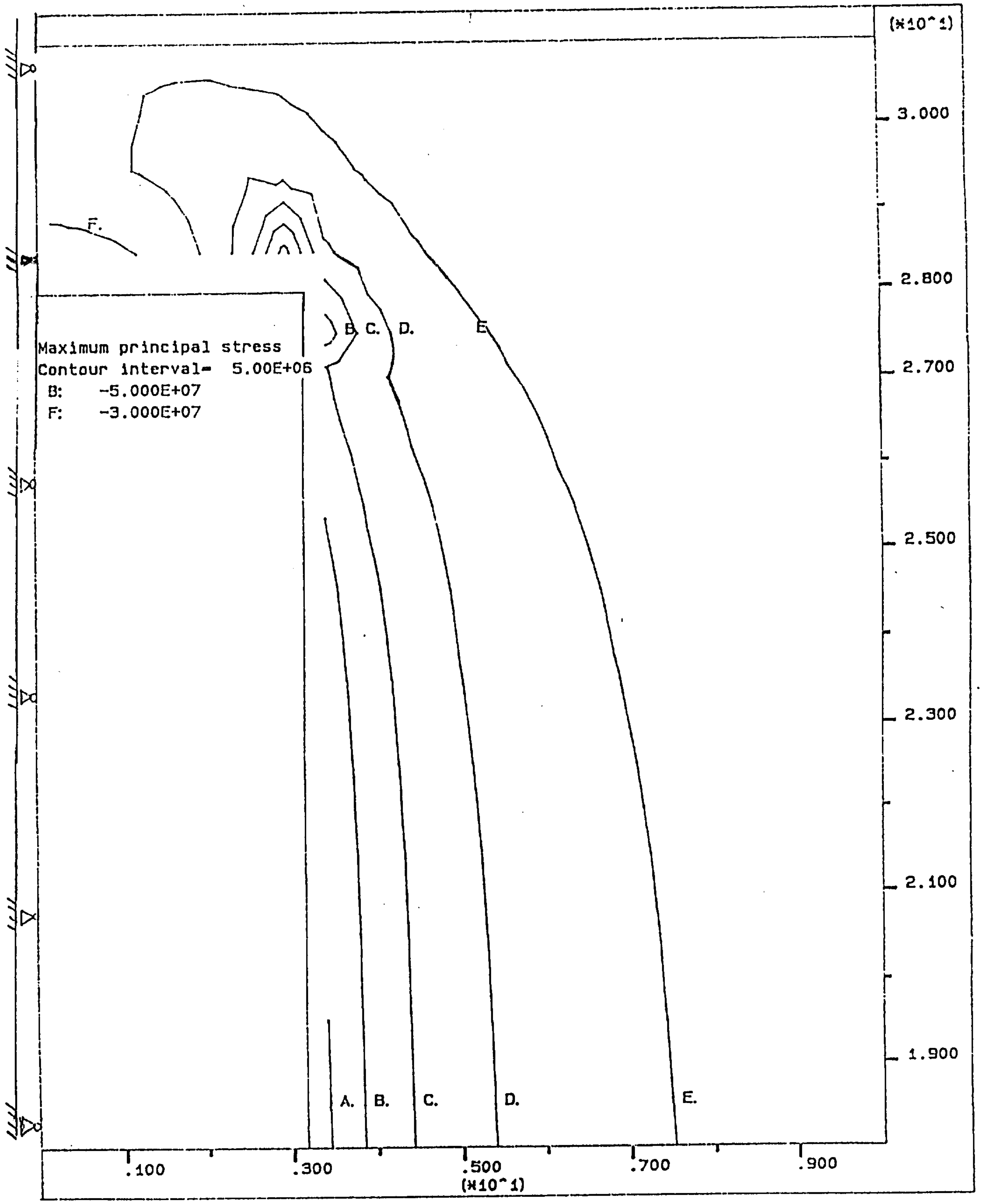

Figure 4.2.2 Maximum priciple stresses around a axisymmetrically loaded tunnel face

distribution around the tunnel is not hydrostatic. These points are stress maxima and are associated with the onset of that type of spalling which is commonly known as 'dog-earing'.

Bow wave fractures are not parallel to the tunnel walls, but intersect them at a small angle. For this reason they are inferred to have initiated near the tunnel face where the local static stress orientations are in accordance with those fracture planes.

Recent laboratory experiments using Timeball Hill quartzite resulted in fracturing as shown in figure 4.2.3. In the experiments a confining stress was applied in the direction of the borehole axis in order to suppress fracturing of the specimen in a direction perpendicular to the borehole axis. Previous experiments have featured fractures perpendicular to the hole because the minor principal stress acts in the out of plane direction, parallel to the opening being analysed. Interference of such fractures with the fracturing directly induced by the stress concentrations near the wall of the opening could lead to misinterpretation of the resulting fracture pattern. However, in this case it was considered of more importance that the global fracturing and subsequent failure of the body of the specimen be delayed and suppressed. This would allow the local fracturing around the borehole to develop further, as a higher stress level could be reached before complete failure of the specimen.

The confining stress which was applied in the direction along the borehole axis was approximately 15 MPa and the vertical stress reached more than 200 MPa before the specimen started to fail. At this stage the U.C.S. of the rock must have been approached. If a true poly-axial compressive stress field could have been applied, local stresses around the borehole could have been allowed to increase even further, but this was not possible at the time. New equipment is available now and experiments allowing for increased local fracturing around openings will be conducted in the near future. The results from this experiment did not indicate any fracturing of the rock ahead of the tunnel face, while extensive fracturing occurs in the side walls in the form of 'dog-earing' and secondary (remote) extension fracturing. No fracturing that could be related to bow wave fracturing was observed.

Typical observations around underground tunnels show that 'dog-earing' is not always present in tunnel side walls which do contain the shallow angle bow wave fractures. Boreholes drilled into tunnel walls containing bow wave fractures also do not always indicate the presence of excessive stresses, as core disking and dog-earing do not necessarily manifest themselves in

Figure 4.2.3. Fracturing around a 60 mm hole in a 300x300x300 mm specimen of Timeball Hill quartzite, loaded in the vertical and out of plane direction.

these boreholes. This is an indication that the formation of bow wave fractures does not require (static) stress levels which are normally associated with failure initiation. The static stresses near the tunnel face are equal or lower than the stresses around the tunnel walls and can for that reason also not account for the formation of bow wave fractures.

It appears that the shallow angled bow wave fractures are not solely associated with the level of static stresses. This is confirmed by experience with the smooth shaping of tunnel walls by the excavation process of 'post-splitting'. In conventional blasting the blast hole spacing is relatively large, the blast holes are charged with large amounts of explosives to completely fillthe holes and the time intervals between detonations are also relatively large. With the post-splitting technique all these parameters are reduced and in fact the time interval is supposed to have completely vanished. All this results in fracture surfaces between the perimeter shot holes only. No bow wave fractures are formed, even in highly stressed environments. (figure 4.2.4.)

Observations of fracture processes associated with a typical blast in a tunnel or a stope face in highly stressed rock can be summarised as follows: Initial fracturing around a shot hole, after the explosive has detonated, is contained within an annulus of densely fractured and crushed rock; this is a result of the shock wave radiating from the explosion. Sometimes several circumferential fractures can be observed around the shot hole as well. From the damaged annulus axi-radial cracks develop preferentially in the direction of the maximum principal stress and curving towards that direction. This process is mainly controlled by the gas under pressure which pressurises the shot hole and which may even enter the radial cracks. (Jaeger and Cook, 1976) At about 0.1 - 0.2m. away from the shot hole, axi-radial fractures can be observed to segment into fractures which twist away from the axi-radial orientation into planes which have the minor principal stress acting normal to it. These are the fractures which are referred to as bow wave fractures. (figure 4.2.5)

In order to analyse this phenomenon, blast experiments in prestressed specimens of PMMA have been conducted. Some of the resulting fractures could be interpreted as fractures twisting away from the axi-radial fractures (figure 4.2.6.), but these experiments can be critisised since boundary reflections of stress waves may have had some influence. In order to avoid such unwanted effects, the experiments were repeated with hydrofracturing of prestressed

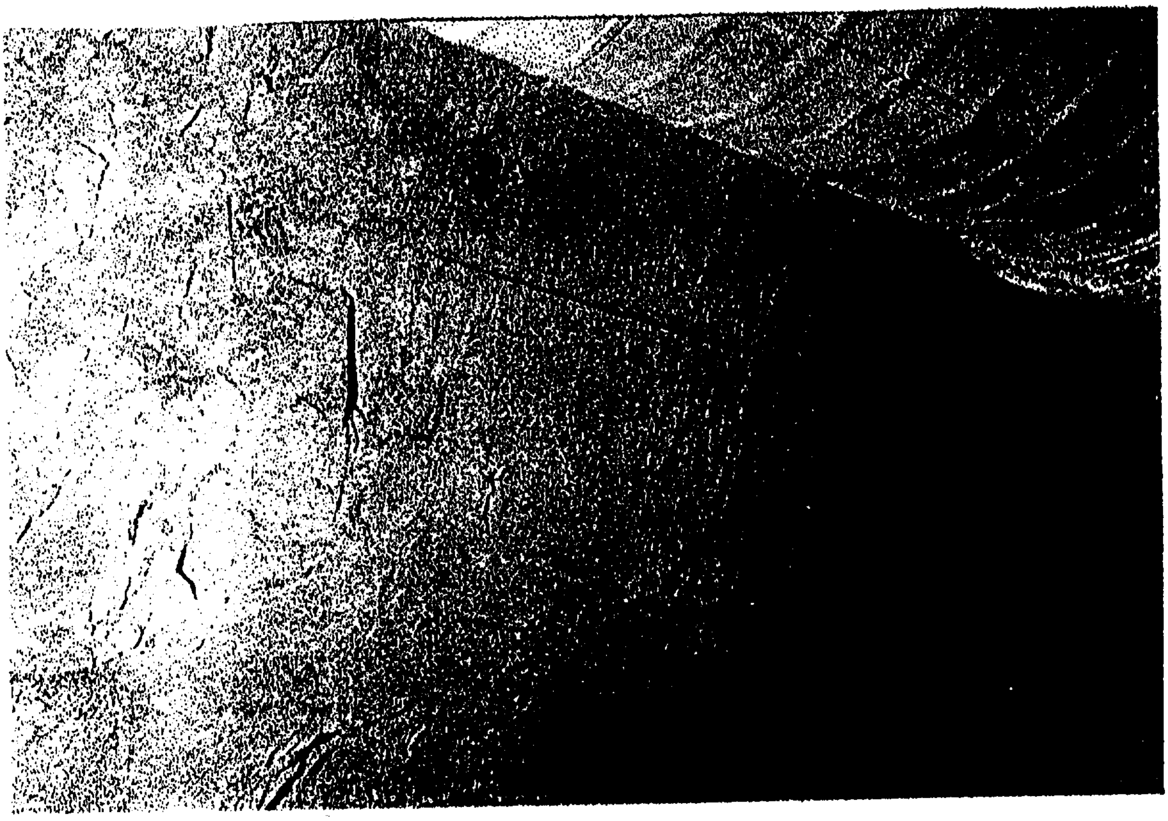

Figure 4.2.4 "Smooth" blasted tunnel

Figure 4.2.5 Segmentation of an axiradial blast fracture from a shot hole into a series of bow wave fractures.

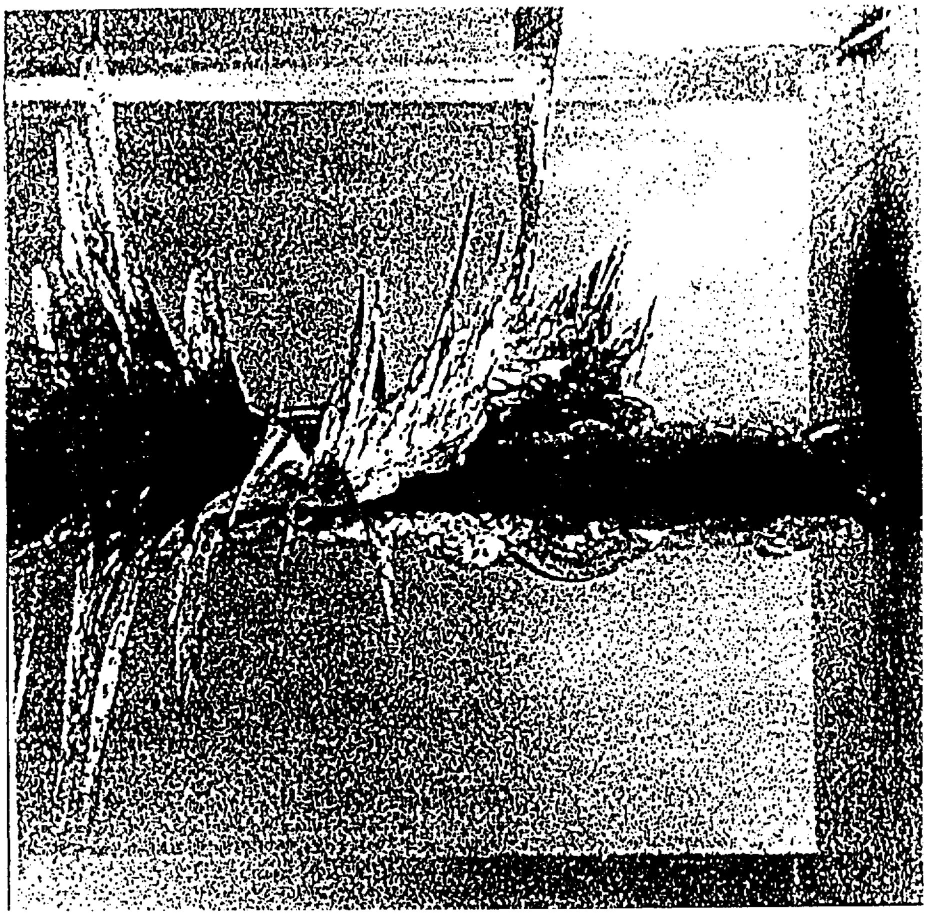

Figure 4.2.6 Segmentation of axiradial blast fractures in a biaxially loaded PMMA specimen.

PMMA specimens. No segmenting or twisting could be reproduced in this case. The fracture process could however not be controlled. Fracturing occurred violently, probably due to the fact that the driving force could not be reduced rapidly enough due to the 'softness' of the hydraulic system. Improvements are required for future experiments.

Although fracture theory requires that evolving cracks in brittle solids cannot twist, Hull (1995) found and explained that apparent twisting of fractures can occur. Although the 'no-twist' rule means that a crack does not necessarily follow a path which is controlled by a maximum stress or energy criterion, it is possible for a fracture to break up into segments which can individually assume the direction of the major principal stresses. Hull's experiments were carried out on cylindrical specimens which were subjected to a dynamic impact in the axial direction and a static torsion in such a way that the principal stresses at the crack tip would increasingly rotate with crack expansion. Similar experiments could be designed to analyse the mechanism of bow wave fracturing.

In order to appreciate the influence of a static stress field on the formation of blast induced fracturing in a three dimensional geometry, as is the case with the bow wave fractures, it is useful to look at the two dimensional case first. In figure 4.2.7a the axi- radial fracture pattern from a pressurised hole in a non-stressed medium is shown. Figure 4.2.7.b shows the fracture patterns from the same pressurised hole in a medium which is subjected to an increasing vertical stress. Larger fractures, concentrated in a smaller area, are formed with increasing (static) loads. The formation of bow wave fractures is assumed to be controlled by a similar mechanism. If the stress field is small in relation to the driving pressure and the strength of the rock, it will hardly have any influence on the fracture geometry, which will consist of a multitude of small fractures which are widely dispersed and which will absorb the gas pressure relatively easily. However a relatively large static stress field will result in the concentration of a few fractures in a confined area similar to figure 4.2.7.b. The gas pressure will only have an effect on those fractures, which will subsequently extend into relatively large fractures compared to the case where a static stress field is absent.

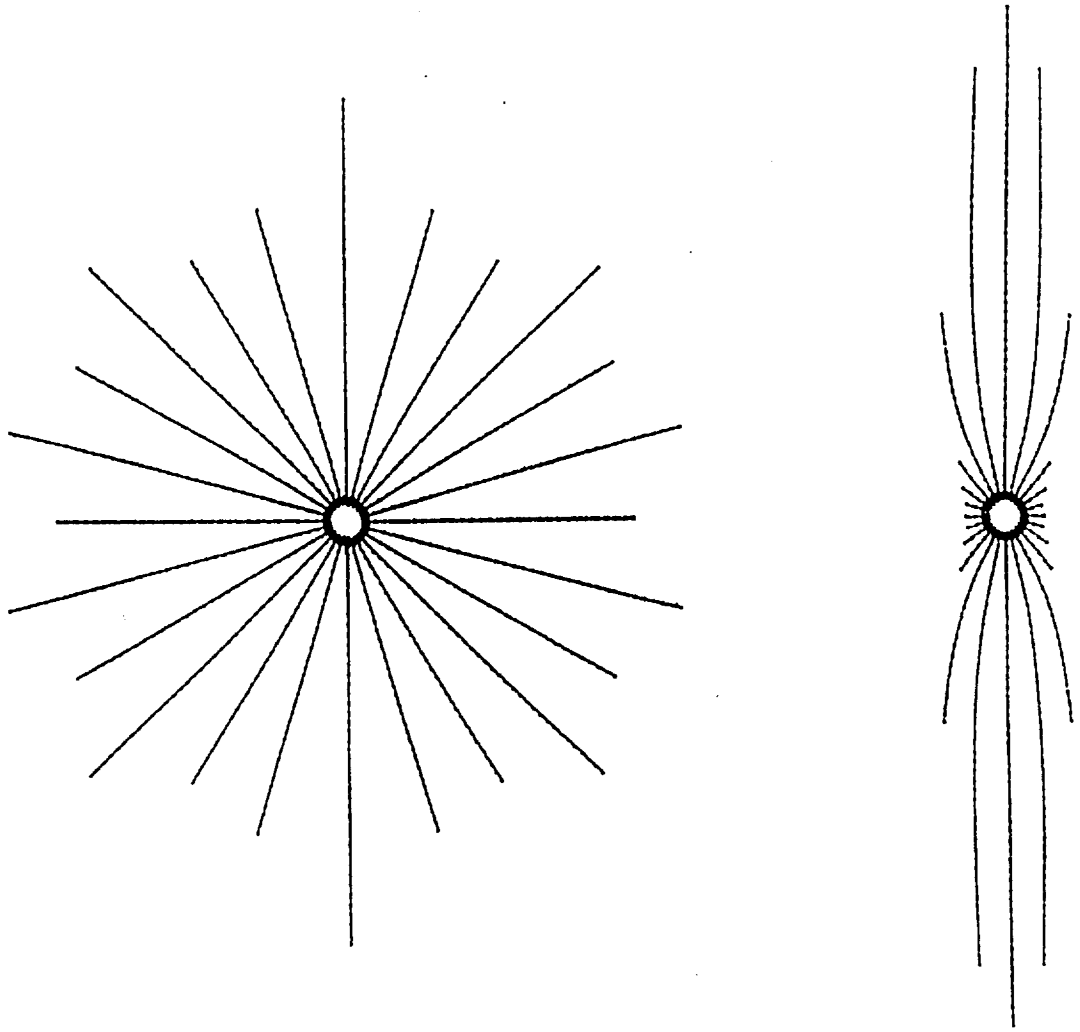

(a) Vertical load = Horizontal load = 1 MPa

(b) Vertical load = 10MPa
Horizontal load = 1MPa

Figure 4.2.7 Simulation with DIGS of the formation of axi-radial fractures from a pressurised hole under the presence of an increasing static far field stress (uniaxial) (a) vertical pressure = horizontal pressure = 1 MPa (b) vertical pressure = 10 MPa and horizontal pressure = 1 MPa

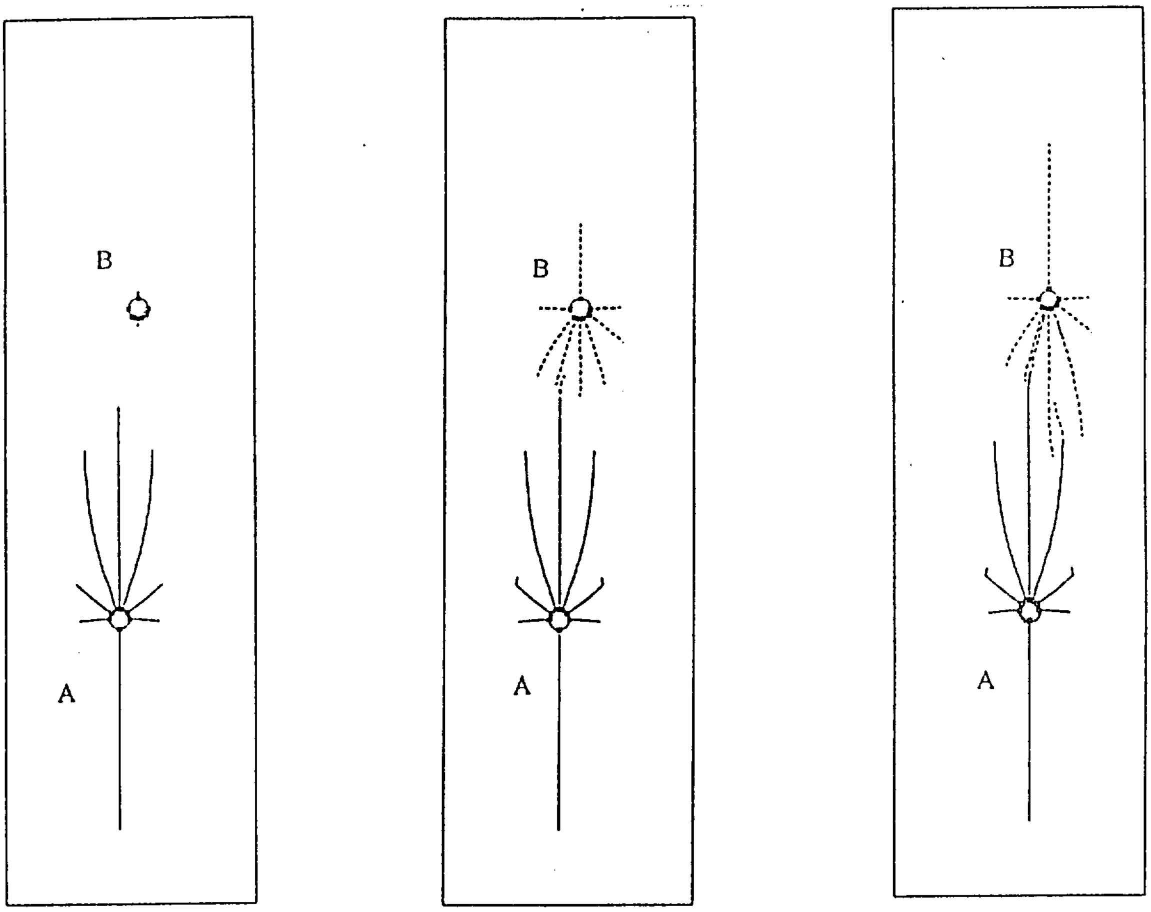

Figure 4.2.8. The interaction between two subsequently pressurised bore holes with respect to the formation of axi-radial fractures (DIGS)

The influence of the pressurisation of one borehole on the fractures around a neighbouring borehole which has lost its pressure has also been analysed in two dimensions and could have similar effects in three dimensions. Figure 4.2.8 shows how an initial pattern of axi-radial fractures is formed around borehole A which is subjected to an internal pressure and which is situated in a stressed medium. Subsequently borehole B is subjected to the same pressure and the pressure in borehole A is switched off. Not only is an axi-radial fracture pattern generated which is similar to that around borehole A, but the axi-radial fractures around borehole A which previously terminated, are initiated again by the effect of the pressure in borehole B and the fractures radiating from it. This effect can also be observed around underground openings and may have a profound effect on the final appearance of blast induced fractures.

When tunnels are excavated by tunnel boring machines, the bow wave fractures can also be observed in highly stressed rock. These fractures have not been studied in detail yet, but they are arguably formed in a similar way as the blast induced fractures, namely a driving force for fracture formation is supplied by the excavation technique (in this case the normal and shear forces of the machine against the tunnel face) and the fractures are confined to a limited area in which they can extend further, due to the effect of the static stress concentrations. As higher stress concentrations are present around stopes, stress induced fracturing is also more frequent than around tunnels. However, a certain percentage of these fractures will be associated with the blast energy in a similar manner to the observations around tunnels.

Conclusions

Bow wave fractures, initiating from the area near the tunnel face and following a direction normal to the static minor principal stress and in such a way assuming a small angle to the tunnel walls are commonly observed around tunnels in highly stressed rock.

Similar (blast induced) fractures are also observed around stopes.

The static stress distribution itself is not sufficient to account for the formation of bow wave fractures around tunnels.

Stresses induced by the excavation process i.e. blast pressure, boring machine forces, etc. are required for the initiation of bow wave fractures and the effect of the static stress concentrations is to confine those fractures in a limited area where they grow more extensively than in the case where a static stress field would be absent and the fractures would be widely dispersed.

Bow wave fracturing can be prevented by using an appropiate technique, such as smooth blasting, which does not provide sufficient 'driving force' for the initiation of those fractures.

Blast induced bow wave fractures, combined with stress induced fractures around stopes, can contribute to the formation of keyblocks in stope hangingwalls. Since keyblocks determine the stability of hanging walls and the potential for rockfalls from hangingwalls, it is of importance to avoid or minimise any process that may cause their formation.

Additional and improved experiments are required to establish in detail the formation processes which lead to the formation of bow wave fractures.

Implications for tunnel and even stope support design could be considerable.

REFERENCES

Carter B.J., Lajtai E.Z. and Petukhov, (1991) Primary and remote fractures around underground cavities. Int. J. Num. Anal. Meth. Geom., Vol.15, pp. 21-40

Friedman M. and Logan J.M., The influence of residual elastic strain on the orientation of experimental fractures in three quartzosesandstones. J. Geophys. Res., vol. 75, pp.375-405, 1970

Hull D., (1995) The effect of mixed mode I/III on crack evolution in brittle solids. Int. J. Fract. vol. 70, pp. 59-79.

Jaeger, J.C. and Cook, N.G.W. (1976) Fundamentals of Rock Mechanics. Chapman and Hall, London

Martin C.D., (1993) The strength of massive Lac du Bonnet granite around underground openings. PhD. Thesis, University of Manitoba, Winnipeg, Canada

Stacey T.R. and de Jongh C.L.,(1977) Stress fracturing around a deep level bored tunnel. J. S. Afr. Inst. Min. Metall., Vol. 78, pp. 124-133.

Stacey T.R.,(1981) A simple extension strain criterion for fracture of brittle rock. Int. J. Rock Mech. Min.Sci., Vol. 18, pp. 469-474.

4.3. SIMULATION OF CREEP-LIKE ROCK MOVEMENTS

4.3.1. Introduction

The work reported under this section contributed towards objective 3.5. One strategy that may be useful to control the stability of the fracture zone is the rate of stope face advance which may affect the accompanying time dependent stope closure and the recurrence of seismic activity. Therefore a study of the mechanisms controlling creep-like behaviour is necessary to gain a better understanding of stope closure. The speed of extraction combined with an appropriate viscous constitutive law should lead to some generalisations to determine safe values of extraction rate and better control of the fracture zone.

Most studies directed at the rock mechanics aspects of tabular excavations have assumed that the surrounding rockmass can be represented by a linear elastic medium (Salamon 1974). This assumption also forms the basis of several mining simulation programs used throughout the South African mining industry (Ryder and Napier 1985, Crouch 1979). This assumption is based on early investigations and does indeed provide an acceptable description of the behaviour of the rock in certain situations (Cook et al. 1966, Ortlepp and Cook 1964, Ryder and Officer 1964). It is however well known that there are discrepancies between elastic theory and the actual rock behaviour which are especially noticeable in the immediate vicinity of the excavation. This is caused partly by the inelastic behaviour of the broken rock and partly by time-dependent properties of the rock. The term 'time dependency' is understood to mean deformation that is not related to geometric changes in the excavation dimensions and which occurs on a time scale of hours or days: i.e. it is not related to elastodynamic seismic behaviour.

The time-dependent behaviour of the rockmass was largely neglected in past analyses due to the difficulty of incorporating time effects in models. This problem needs to be addressed to enable engineers to predict long term stability of service excavations. A knowledge of time-dependent components will also lead to more accurate closure prediction in stopes. In this study the transient closure (which is a function of all the components described above) in stopes after blasting is investigated. The term *transient closure* is understood to mean the closure as a function of time observed between successive blasting operations. It must therefore be emphasised that there are no changes in the excavation geometry when studying transient closure behaviour. A number of workers (Gürtunca et al. 1989, Gürtunca 1989) have studied closure in stopes as a function of face advance or number of days. These studies included the complicating effect of changes in geometry and will not be considered in this study. Note however that the closure observed for a face left standing can be considered as transient behaviour as no changes in the geometry takes place after the last blasting operation. The following noteworthy studies of transient closure behaviour are described in the literature.

Leeman (1958) used closure recorders to measure transient closure profiles in a tabular stope at East Rand Proprietary Mines. He observed profiles similar to figure 4.3.1.1 where the rate of closure suddenly increases just after blasting time. This high rate of closure decreases within hours to give a gradual asymptotic closure until the next blast occurs and the pattern repeats. Similar closure profiles are observed at other mines in the South African mining industry (Kersten 1994, Güler 1994). However, Leeman did not give any explanation for the observed closure profiles although he did note that the amount of closure caused by blasting diminishes with distance from the working face. The rate of closure also varied greatly from one point to the next and was affected by the position of the measuring point in relation to the support in the stope.

Hodgson (1967) also took closure measurements in East Rand Proprietary Mines. He explained the gradual asymptotic closure as being caused by the time-dependent migration of the fracture zone ahead of the face resulting in the effective span becoming bigger. Hodgson predicted that if the face advanced faster than the migration of the fracture zone, less energy would be released in a stable manner thereby increasing the incidence of rockbursts. This is in agreement with the statistical analysis of Cook et al. (1966) which indicated an increase in rockbursts for a face advance rate of more than 4 metres a month for small abutments to 8 metres a month for large abutments.

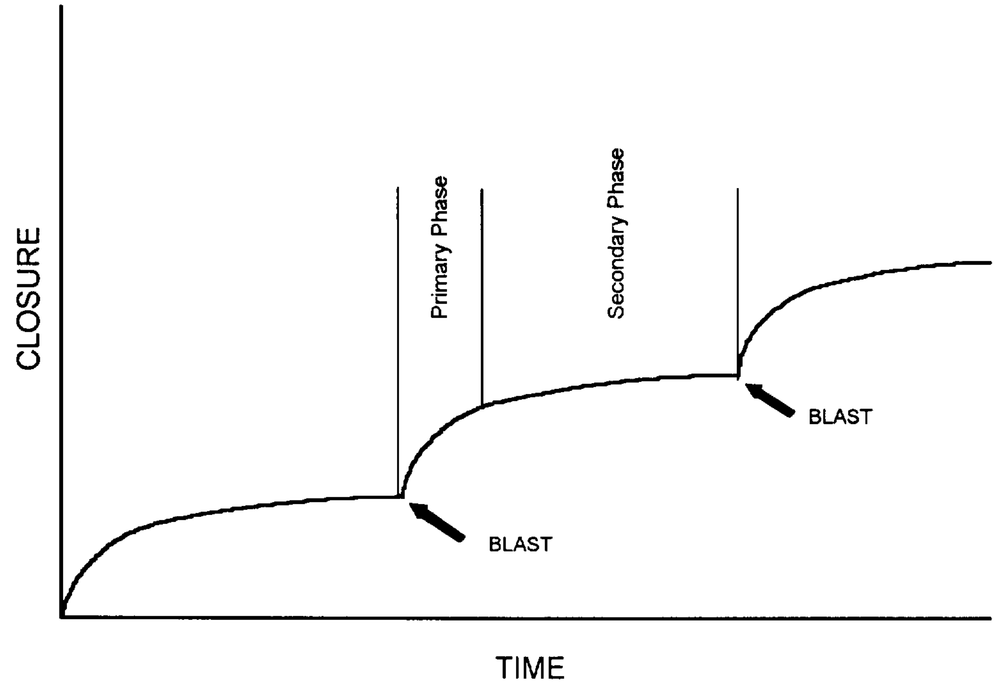

Figure 4.3.1.1 Typical profile of continuous stope closure as a function of time.

The first quantitative attempt to analyse transient closure profiles of tabular stopes was made by McGarr (1971) using data from East Rand Proprietary Mines. He achieved some success by using an empirical approach to represent the closure. McGarr suggested that the relaxation time constant τ in the equations could be used as a parameter to describe the ability of the rock mass to form a fracture zone in response to face advance. High values of τ might be associated with mines that are prone to rockbursts.

Following the above discussion, the transient closure of any tabular excavation is a function of the superposition of the following factors:

1. Elastic convergence of the rock.
2. Inelastic closures caused by existing discontinuities (fractures, joints and bedding planes).
3. Creep of the intact rock.
4. Creep along existing discontinuities.
5. Time-dependent formation of new fractures and resulting inelastic movements.

It is very difficult to quantify the amount of closure contributed by each component. This study investigated the feasibility of representing the rockmass surrounding tabular excavations as an equivalent viscoelastic medium which includes all the components mentioned above. Although the contributions of the individual components cannot be distinguished, this approach enables time-dependent effects which occur independently of the geometrical changes to the stope, to be modelled. It must however be borne in mind that the contribution of inelastic movements and creep along discontinuities is more pronounced in the skin of the excavation than in the intact rock further away from the excavation. The first order assumption of a continuum viscoelastic medium ignores this effect. If the viscoelastic parameters are calibrated using skin to skin closure measurements , the calibrated values are only valid in this region.

4.3.2. Viscoelastic convergence in a parallel sided panel without contact between the hanging- and footwall

Currently no analytical solution for the viscoelastic convergence of a tabular stope is available in literature. Therefore a solution was derived using the correspondence principle of viscoelasticity (Flügge 1975) and two building blocks namely a known elastic solution and a certain viscoelastic model.

When looking at the closure profiles of tabular stopes, the closure approaches an asymptotic value after the excavation is enlarged (See figure 4.3.1.1). This behaviour can therefore be modelled by both the viscoelastic Kelvin model and the viscoelastic three parameter solid (Malan 1995). McGarr (1971) provided data and analysis illustrating that the instantaneous closure at the time of face advance is negligible and that the eventual closure is associated almost entirely with the time-dependent migration of the fracture zone ahead of the face. Data supplied by Güler (1994) and closure profiles published by Leeman (1958) confirm the statement that the instantaneous closure at the time of face advance is negligible compared to the eventual closure. Therefore when deriving the viscoelastic convergence equation for this study, the Kelvin model consisting of an elastic element in parallel with a viscous dashpot giving no instantaneous strain components is used. It is however important to emphasise that it is unknown whether this Kelvin assumption is applicable to all geotechnical areas throughout the mining industry. More experimental work is necessary to address this question.

Salamon (1968) derived the elastic solution for the convergence in a parallel sided panel where there is no contact between the hanging- and footwall. Applying the correspondence principle to Salamon's elastic solution for a parallel sided panel without total closure and by making the assumption that the rock behaves elastically in hydrostatic compression and as a two parameter

Kelvin substance in distortion, leads to the following viscoelastic convergence equation (Malan 1995).

$$S_z(x,t) = -4W_z\sqrt{l^2 - x^2}\,(1+\frac{dx}{2})g\left[1 + c_1 e^{-\alpha_1 t} - (c_1 + 1)e^{-\alpha_2 t}\right] \tag{4.3.2.1}$$

where

$$W_z = \frac{-\gamma H}{2}\left[(1+k)+(1-k)\cos 2\alpha\right] \tag{4.3.2.2}$$

$$d = \frac{\sin\alpha\cos\beta}{H} \tag{4.3.2.3}$$

$$g = \frac{3K + 2q_0}{q_0(6K + q_0)} \tag{4.3.2.4}$$

$$\alpha_1 = \frac{q_0}{q_1} \tag{4.3.2.5}$$

$$\alpha_2 = \frac{6K + q_0}{q_1} \tag{4.3.2.6}$$

$$c_1 = -\frac{6K + q_0}{6K + 4q_0} \tag{4.3.2.7}$$

S_z = viscoelastic convergence

l = half span of the stope

x = distance from the centre of the stope (origin of co-ordinate system)

γ = specific weight of the rock

H = depth below surface

k = ratio of horizontal to vertical stress

α = dip of the reef

β = angle between x-axis and the dip

K = bulk modulus

$q_0 = 2G$ where G is the shear modulus

q_1 = viscosity coefficient of the viscous element in the two parameter Kelvin model

The z-axis is perpendicular to the plane of the excavation and points toward the footwall. The two-dimensional section is taken parallel to a plane normal to the y-axis (see Salamon et al. (1964) p. 117).

It is clear from equations 4.3.2.4 to 4.3.2.7 that the viscoelastic parameters g, c_1, α_1 and α_2 are not fundamental material constants but functions of the bulk modulus, shear modulus and viscosity coefficient. These parameters are grouped together as g, c_1, α_1 and α_2 to simplify parameter calibration when using experimental closure data. The bulk and shear modulus can be obtained from the calibrated parameters by solving the two simultaneous equations 4.3.2.4 and 4.3.2.7 to give

$$K = \frac{4c_1 + 1}{12gc_1(1 + c_1)} \tag{4.3.2.8}$$

$$G = \frac{-1}{4gc_1} \tag{4.3.2.9}$$

This can be written in terms of Young's modulus E and Poisson's ratio ν as

$$E = \frac{4c_1 + 1}{-4gc_1^2} \tag{4.3.2.10}$$

$$\nu = \frac{2c_1 + 1}{2c_1} \tag{4.3.2.11}$$

The viscosity coefficient q_1 can be obtained by substituting equation 4.3.2.9 in 4.3.2.5 to give

$$q_1 = \frac{1}{-2gc_1\alpha_1} \tag{4.3.2.12}$$

As the viscosity coefficient can be obtained from either equation 4.3.2.5 or 4.3.2.6, it follows that the time constants α_1 and α_2 are not independent. Equation 4.3.2.5 and 4.3.2.6 can be combined by eliminating q_1 and substituting equations 4.3.2.8 and 4.3.2.9 to give the relationship between the time constants as

$$\alpha_1 = \alpha_2 \frac{(1 + c_1)}{-3c_1} \tag{4.3.2.13}$$

When $t \to \infty$, the viscoelastic convergence approaches an asymptotic value given by

$$S_z(x) = -4W_z g\sqrt{l^2 - x^2}\left(1 + \frac{dx}{2}\right) \tag{4.3.2.14}$$

The only viscoelastic parameter present in equation 4.3.2.14 is g. It follows from the definition of g in equation 4.3.2.4 that it is only a function of the bulk and shear modulus. The magnitude of the viscoelastic convergence when $t \to \infty$ is therefore not dependent on the viscosity coefficient. It can easily be shown that when $t \to \infty$, the viscoelastic solution is identical to the elastic solution by substituting equation 4.3.2.4 in equation 4.3.2.14 and by rewriting the bulk and shear modulus in terms of Young's modulus and Poisson's ratio.

The length of span L_c at which there is contact between the hanging- and footwall at the centre of the stope (x = 0) at time $t \to \infty$ is

$$L_c = 2l = \frac{S_z}{-2W_z g\left(1 + \frac{dx}{2}\right)} \tag{4.3.2.15}$$

with S_z set equal to the stoping width.

4.3.3. Incremental face advance

Equation 4.3.2.1 is applicable to situations where the total length of the stope is excavated instantaneously. This is not the case in practice where the face is incrementally advanced. Assume that the first mining increment is created suddenly at time τ_1 giving a stope of half span L. Equation 4.3.2.1 will give the viscoelastic convergence for this step as $S_z(l = L, x, t - \tau_1)$. At time τ_2 the face is advanced on both sides of the stope by Δl giving a half span of L + Δl. Using equation 4.3.2.1 with a half span of L + Δl at time τ_2 results in the total span being created in one step which is clearly wrong. At time $\tau_2 + \Delta\tau$ the total viscoelastic convergence is the sum of the viscoelastic convergence caused by a half span of L (excavated at time τ_1) plus an incremental viscoelastic convergence caused by the incremental length Δl, excavated at time τ_2. The incremental viscoelastic convergence is the difference between the viscoelastic convergence of a stope with half span L + Δl created at time τ_2 and the viscoelastic convergence of a stope with half span L also created at time τ_2 . Therefore at time $\tau_2 + \Delta\tau$ the viscoelastic convergence is given as

$$S_z = S_z(l = L, x, t - \tau_1) + S_z(l = L + \Delta l, x, t - \tau_2) - S_z(l = L, x, t - \tau_2) \quad for \quad x \le L \tag{4.3.3.1}$$

and

$$S_z = S_z(l = L + \Delta l, x, t - \tau_2) \quad for \quad L < x \leq L + \Delta l \qquad (4.3.3.2)$$

This principle can be extended for any number of increments (Malan 1995).

4.3.4. Parameter calibration from stope closure data

Instruments to measure closure are usually installed in stopes where the span has already reached a significant length. Although an appreciable amount of closure has taken place up to the time of installation, the amount is unknown and therefore the closure is taken to be zero at this point for a reference level. It is therefore not possible to calibrate the model with the number of steps, since the incremental advance for every step and the increase in closure for every step is unknown. However, if the span is increased by blasting, the incremental closure can be used to calibrate g, c_1, α_1 and α_2. The incremental viscoelastic convergence can be obtained from equation 4.3.3.1 by setting the first term equal to zero.

$$\Delta S_z = S_z(l = L + \Delta l, x, t - \tau_2) - S_z(l = L, x, t - \tau_2) \qquad (4.3.4.1)$$

Substituting equation 4.3.2.1 and assuming that the stress before and after the blast stays the same gives

$$\Delta S_z(x,t) = -4W_z\,(1 + \frac{dx}{2})g\left[1 + c_1 e^{-\alpha_1 t} - (c_1 + 1)e^{-\alpha_2 t}\right]\left[\sqrt{(L + \Delta l)^2 - x^2} - \sqrt{L^2 - x^2}\right]$$

(4.3.4.2)

for $x \leq L$. In figure 4.3.4.1 the incremental viscoelastic convergence ΔS_z (equation 4.3.4.2) is plotted as a function of the distance from the original face for a stope with a half span of 50 m and a face advance of 1 m (arbitrary values for the parameters $t, W_z, g, c_1, \alpha_1, \alpha_2$ were used with x ranging from L to 0). It follows from figure 4.3.4.1 that the further the point of measurement is from the face, the less the incremental viscoelastic convergence becomes following every blast. This is in agreement with Leeman's (1958) observation that the effect of blasting upon closure becomes progressively less, the further the point of measurement become from the working face. Ideally the measurement station should therefore be installed close to the face to obtain large incremental closure for more accurate parameter calibration.

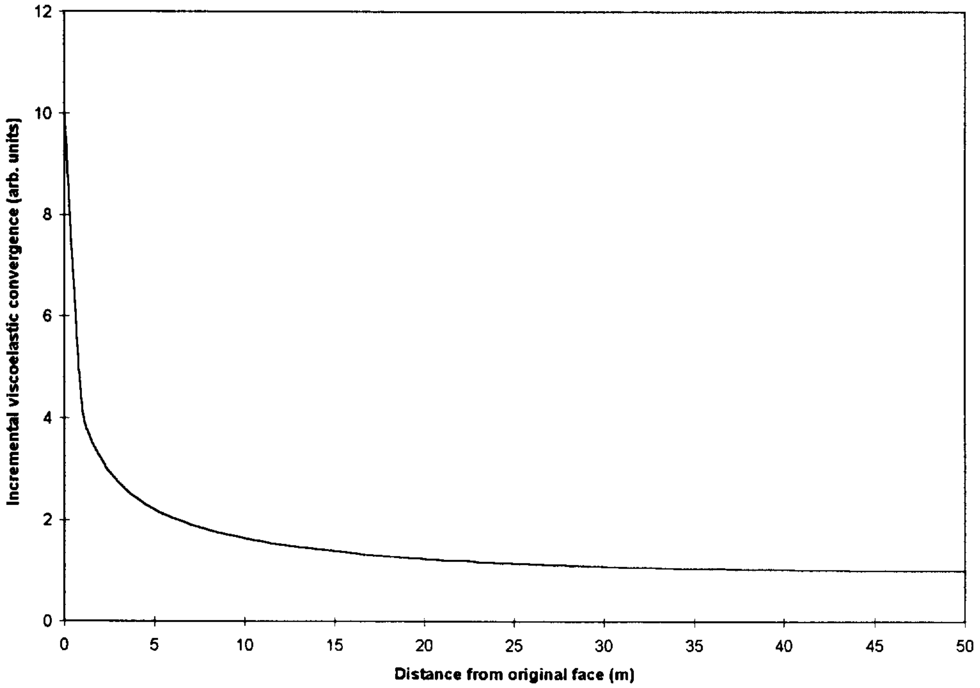

Figure 4.3.4.1 Incremental viscoelastic convergence as a function of the distance from the face.

Equation 4.3.4.2 assumes that both sides of the stope are blasted simultaneously giving an advance of Δl at both faces. This is however seldom the case in underground workings where often only one side of the panel is blasted. This problem is solved by introducing an equivalent stope principle. Equation 4.3.4.2 is based on both linear elasticity theory and linear viscoelasticity theory and therefore an advance of Δl on one side only (figure 4.3.4.2(a)), can be represented by an equivalent stope with a simultaneous advance of $\Delta l/2$ on both sides, provided that the measuring point is shifted by a distance $\Delta l/2$ away from the blasted face to keep the original distance to the face (length a) the same (figure 4.3.4.2(b)). For a stope with a face advance Δl at one side only, equation 4.3.4.2 can therefore be written as

$$\Delta S_z(x,t) = -4W_z\,(1+\frac{dx}{2})g\left[1+c_1e^{-\alpha_1 t}-(c_1+1)e^{-\alpha_2 t}\right]\left[\sqrt{\left(L+\frac{\Delta l}{2}\right)^2-\left(x-\frac{\Delta l}{2}\right)^2}-\sqrt{L^2-x^2}\right]$$

(4.3.4.3)

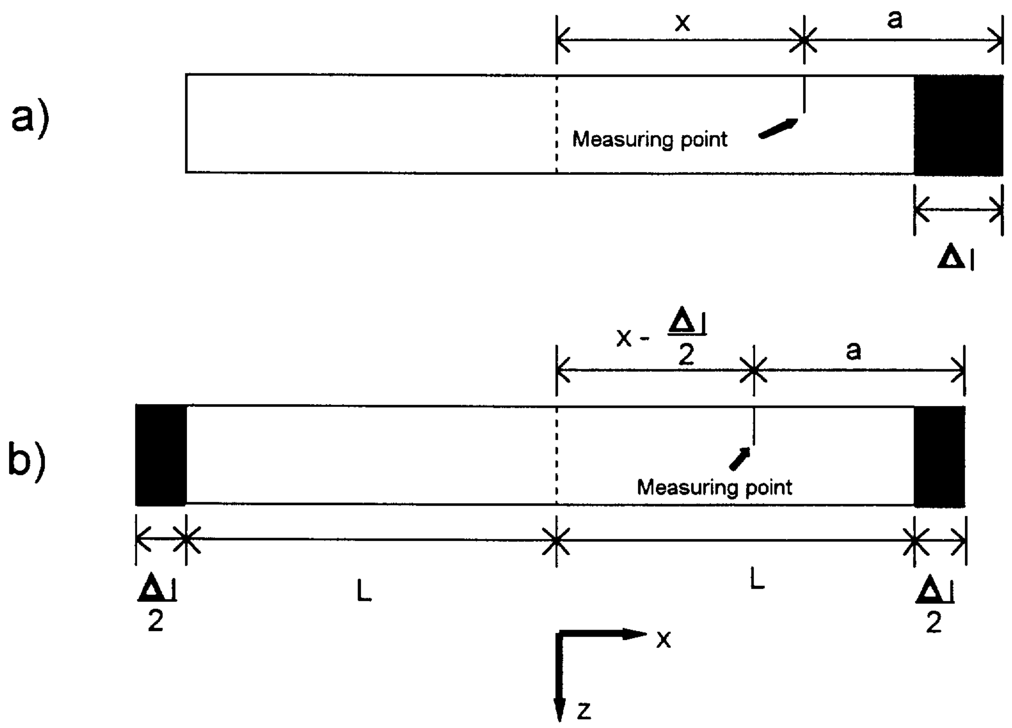

Figure 4.3.4.2 The equivalent stope principle.

To illustrate the method of parameter calibration, data from a longwall stope with a span of 200 m was used (Güler 1994). The depth of excavation was 2700m, the dip was 25° and the closure instrument was installed 16,6m from the face. After the blast (one side only), the increase in span was 1,4 m. To illustrate the viscoelastic approximation, equation 4.3.4.3 was fitted to the data using the method described in Malan (1995). Figure 4.3.4.3 gives the experimental data (incremental part after blast only) and the fitted viscoelastic model. It is clear that a good fit can be obtained. The calibrated values for this stope are $g = 1{,}42 \times 10^{-5}$ MPa^{-1}, $c_1 = -0{,}69$, $\alpha_1 = 0{,}06$ h^{-1} and $\alpha_2 = 0{,}4$ h^{-1}. Equations 4.3.2.10, 4.3.2.11 and 4.3.2.12 can be used to obtain values for Young's modulus, Poisson's ratio and viscosity coefficient as $E = 65$ GPa, $\nu = 0.27$ and $q_1 = 850$ GPa.h.

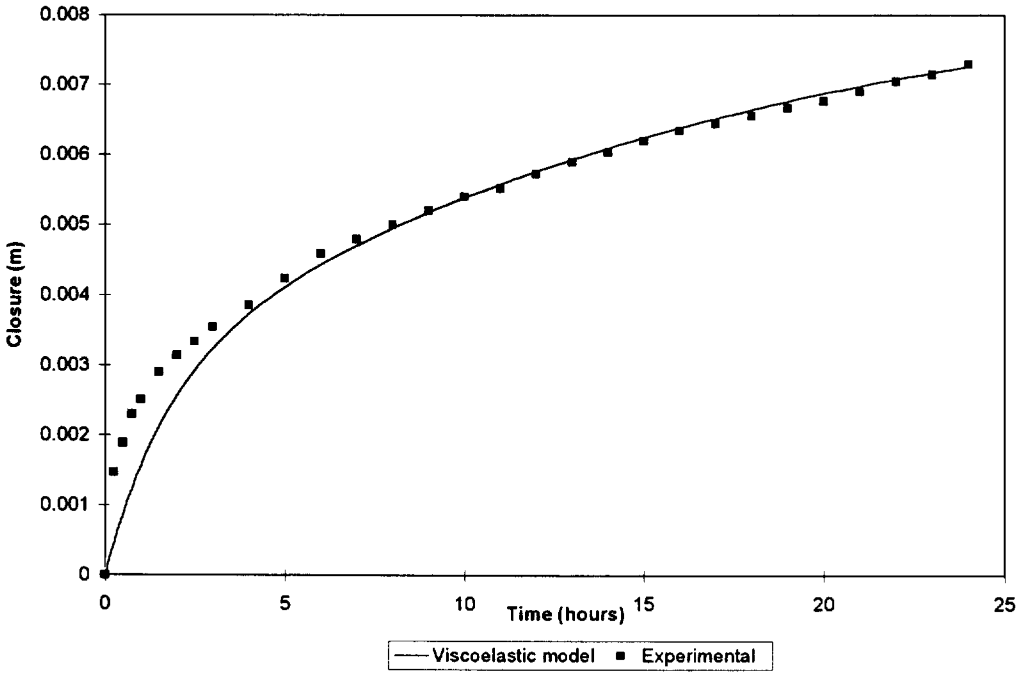

Figure 4.3.4.3 Comparison between experimental stope closure (Güler 1994) and best fit obtainable from the derived viscoelastic model.

Although it is therefore possible using this approach to represent transient stope closures, further work is necessary to quantify the contributions of the inelastic and time-dependent components to the closure. The different components contributing to the time-dependent component need to be separated to distinguish the relative importance of each. It was mentioned that various workers suggested that the gradual asymptotic closure in the secondary phase is caused by the time-dependent migration of the fracture zone ahead of the face. Further work is necessary to quantify this possible mechanism.

Conclusion

The advantage of the viscoelastic approach is that more accurate closure prediction is possible since the time-dependent components are included in the analysis. This preliminary study showed that the assumption of representing the rockmass as a Kelvin material is adequate. The use of more elaborate viscoelastic models must be weighed against the increased complexity of more parameters that need to be calibrated. Care also needs to be exercised when applying the derived viscoelastic model as it is not valid for stopes where total closure takes place and if the geometry is such that plain strain assumptions are impossible. As most configurations in practice can not be simplified to a two dimensional approximation, further work is necessary to allow for three dimensions. This will have to take the form of numerical analyses to solve complex geometrical configurations. The following section describes the numerical technique developed to solve two-dimensional problems. Ultimately this will be extended to three dimensions.

4.3.5 Modelling of incremental viscoelastic problems using the displacement discontinuity approach

To model the creep-like behaviour of rock, Crawford and Curran (1983) used an extended displacement discontinuity technique to solve problems in linear viscoelasticity. The advantage of the method is that the solution can be obtained explicitly as a function of time and hence a time stepping procedure becomes unnecessary. However, when modelling a mining excavation developed in several steps, the time when each of these increments was mined becomes important. Therefore a further extension of the technique is required. Such an extension is developed below using a superposition principle proposed by Salamon (1974).

When solving a linear elastic problem using the displacement discontinuity approach, the relationship between stresses and displacement discontinuities are given by

$$\{\sigma\} = [k]\{D\} \tag{4.3.5.1}$$

where $\{\sigma\}$ is the stresses in the discontinuities, $\{D\}$ denote the displacement discontinuity components and $[k]$ is the matrix of influence coefficients which depends on the geometry of the problem and the material properties.

Applying the correspondence principle to equation 4.3.5.1 (for two dimensional problems using constant elements) and assuming a Kelvin model in distortion gives

$$\{D(t)\} = \left(4\pi g\left(1 + ce^{-\alpha_1 t} - (c+1)e^{-\alpha_2 t}\right)\right)\left[k^*\right]^{-1}\{\sigma\} \tag{4.3.5.2}$$

Postulate that the first increment is created at time τ_1, and that it is represented by K displacement discontinuity elements. The displacement discontinuities components will be represented by $D_i(t-\tau_i)$ where the subscript denotes the step number. E.g. $D_2(t-\tau_2)$ implies the solved displacement discontinuities at time $t-\tau_2$ for the complete problem geometry after the elements of the second step have been added. The 2K time-dependent displacement discontinuity components $\{D_1(t-\tau_1)\}$ for the first increment can be obtained from equation 4.3.5.2 for any time $t > \tau_1$. However if the second step is developed at time τ_2 (L elements added), the method of superposition must be applied to give the time-dependent displacement discontinuity components at time $t > \tau_2$ as

$$\{D(t)\} = \{D_1(t-\tau_1)\} - \{D_1(t-\tau_2)\} + \{D_2(t-\tau_2)\} \qquad (4.3.5.3)$$

After the second increment the total number of elements is K+L. Note that $\{D_2(t-\tau_2)\}$ contains 2(K+L) components whereas $\{D_1(t-\tau_1)\}$and $\{D_1(t-\tau_2)\}$contain only 2K components. When doing the summation the 2L extra components for the second increment is going to be zero for $\{D_1(t-\tau_1)\}$and $\{D_1(t-\tau_2)\}$. This is trivial as the displacement discontinuity components for any element which does not yet exist must be zero! For n number of steps

$$\{D(t)\} = \sum_{i=1}^{n-1}\left[\{D_i(t-\tau_i)\} - \{D_i(t-\tau_{i+1})\}\right] + \{D_n(t-\tau_n)\} \qquad (4.3.5.4)$$

This expression is valid for time $t > \tau_n$.

Equation 4.3.5.4 implies that to obtain a numerical solution for a viscoelastic problem consisting of n increments at time $t > \tau_n$, (2n-1) DD solutions needs to be calculated. For two-dimensional constant displacement discontinuity elements this can however be reduced to finding just n solutions. This is possible because the material properties can be separated from the kernel table as a multiplier when the problem is linear with respect to the boundary conditions (e.g. no closure). From equation 4.3.5.2

$$\frac{\{D(t)\}}{\left(4\pi g\left(1+ce^{-\alpha_1 t}-(c+1)e^{-\alpha_2 t}\right)\right)} = \{D_{ml}\} = [k^*]\{\sigma\} \qquad (4.3.5.5)$$

Therefore only one $\{D_{ml}\}$ needs to be solved for every step and multiplied with the correct time-dependent multiplier to obtain $D_i(t-\tau_i)$ and $D_i(t-\tau_{i+1})$for the particular step. This is however not possible for three dimensional displacement discontinuity kernels and (2n-1) DD solutions will have to be calculated. The individual solutions need not be stored as the summation can be done in a temporary array as soon as each solution is calculated.

The same principle applies when calculating displacements in the field. A similar procedure can therefore be used. As the creep problem is solved, the stress is not a function of time. The stress will therefore change in step-like fashion between different mining increments.

The convergence in a 2D horizontal slit where the slit is enlarged incrementally (figure 4.3.5.1) will be solved using the numerical technique. The surrounding material is assumed to behave elastically in dilatation and like a viscoelastic Kelvin model in distortion. It is postulated that increment 1 is a slit of 10 m created at time $\tau_1 = 0$ hours. This is followed by two increments at time $\tau_2 = 24$ hours and time $\tau_3 = 48$ when the length of the slit is each time increased by 1 m excavations at both sides of the slit. Other values used are Young's modulus = 70 GPa, Poisson's Ratio =0.2, Viscosity Coefficient = 500 GPa.h, and the vertical stress = 60 MPa. The convergence is calculated 0.125 m from the centre of the slit.

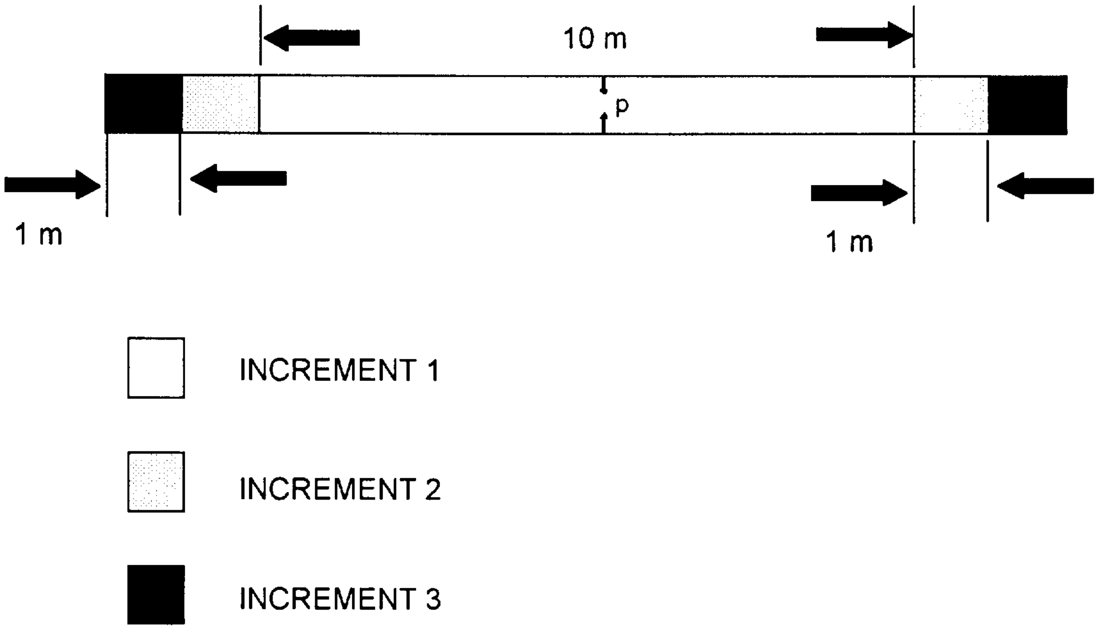

Figure 4.3.5.1 Incremental enlargement of a 2D slit.

The numerical problem was solved using a 40 element approximation for increment 1. This was extended by 4 elements on each side for both increments 2 and 3. Figure 4.3.5.2 illustrates both the analytical (Malan 1995) and numerical solutions for convergence 0.125m from the centre of the slit. It is clear that the numerical solution is a very good approximation. It does however slightly overestimate the analytical solution because constant displacement discontinuity elements are used. (See Ryder and Napier 1985).

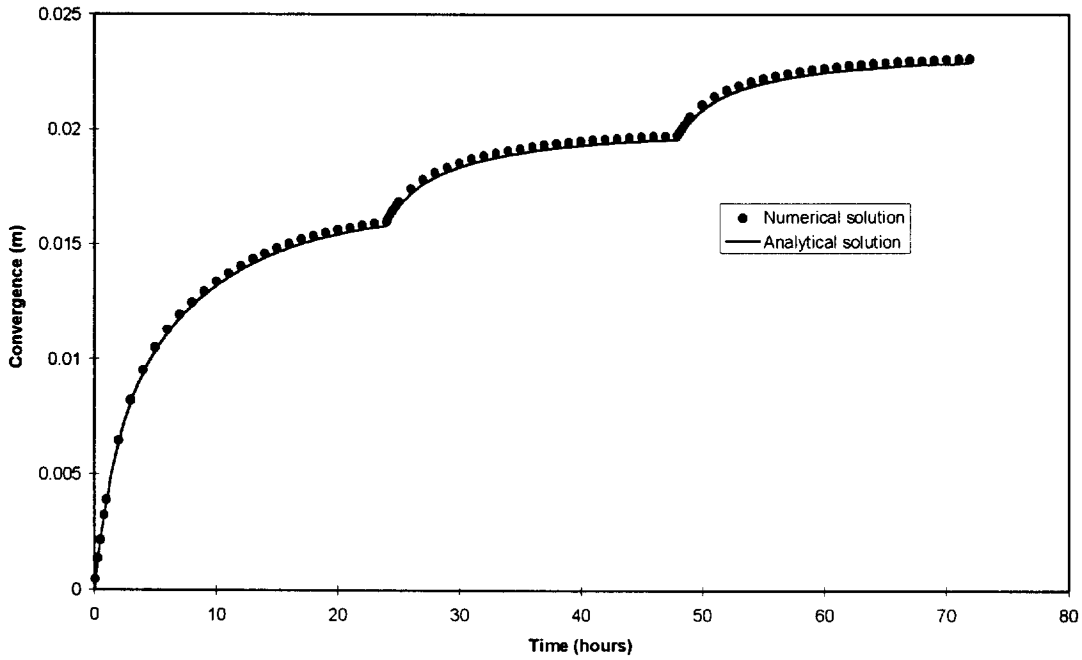

Figure 4.3.5.2 Numerical and analytical solution of the convergence 0.125 m from the centre of the slit for the problem illustrated in figure 43.5.1

Conclusion

The modified displacement discontinuity technique is a convenient method to solve incremental problems in viscoelasticity. The solutions can be obtained explicitly as a function of time and therefore there is no need for a time stepping procedure. The method however requires that (2n-1) solutions (or n solutions for two dimensional displacement discontinuities) be calculated for a viscoelastic problem consisting of n increments. If the number of increments and elements become very large, the method can become very time consuming. Further work is also necessary to make provision for total closure.

4.3.6. Creep testing of discontinuities: Evaluating fractal dimension as a parameter for describing surface roughness

As part of the study of time-dependent rock behaviour, it is planned to investigate the creep behaviour of joints. Since Barton (1976) illustrated the strong correlation between the shear strength and roughness of joints, a lot of interest has been generated to find suitable parameters to quantify joint roughness. Since there might also be a possible correlation between the creep behaviour and roughness of joints, a roughness parameter is required. In the literature three methods are described to obtain roughness parameters. Unfortunately all three methods are plagued by problems and therefore more work needs to be done to find a suitable method. The three methods are briefly described below

a) JRC

When Barton (1976) proposed a new shear strength criterion for joints, he showed the strength to be proportional to the so called joint roughness coefficient (JRC). JRC represents a sliding scale of roughness which can vary from approximately 0 to 20. Barton and Choubey (1977) then published typical roughness profiles with their associated JRC numbers. These profiles have become almost the standard for workers making visual estimates of JRC by comparing their own profiles with Barton's profiles. This method is however very subjective and Tse and Cruden (1979) pointed out that misjudgement of 1 JRC unit lead to over 10% error in shear strength calculations.

b) Spectral methods

Workers like Brown and Scholtz (1985) and Power et al. (1987) computed power spectral densities of various natural surfaces. What they found was that profiles of the fracture surfaces have decreasing power law spectra of the form

$$G(k) = Ck^{-\alpha} \qquad (4.3.6.1)$$

where k is the wavenumber. The roughness can therefore be described by two parameters namely

1) the slope of the power spectrum on a log-log plot (parameter α) and

2) the intercept of the power spectrum line on a log-log plot (parameter C).

There are however practical problems associated with this method. If the spatial sampling rate of the equipment used to obtain the roughness profile is not high enough, significant aliasing can take place, distorting the power spectrum at the higher frequencies. Incorrect roughness parameters will then be obtained.

c) Fractal methods

Because joint surfaces are irregular and the roughness profiles seems to be repeated at different scales, it seems possible to use fractal theory to described the degree of roughness. Various workers have then attempted to use the fractal dimension as a roughness parameter. The technique however contains many pitfalls and there is even doubt whether it can be used at all. In this study the fractal dimension of several discontinuities from rocks in the South African mining industry has been investigated. More information on the technique is given below.

Experimental determination of roughness profiles

To investigate the use of fractal dimension eleven discontinuity samples were collected from industry. Information on the samples is given in Table 1. The core yards of the various mines seemed to be a good source of material. Samples containing discontinuities parallel to the axis of the specimen can be cut to convenient sizes and on opening the specimen gives a sample with a square discontinuity surface.

SAMPLE	**DISCONTINUITY TYPE**	**MATERIAL**	**LOCATION**
S1	Fracture	Alberton lava	Elandsrand
S2	Fracture	Amygdaloidal Alberton lava	WDL
S3	Fracture	Amygdaloidal pillow lava	WDL
S4	Fracture	Fine grained argillaceous Main Bird quartzite	WDL
S5	Fracture	Kimberly/Elsburg quartzite	WDL
S6	Slickensided joint	Fine grained quartzite	WDL
S7	Rough joint	Medium grained quartzite. Sligthly argillaceous	WDL
S8	Chloritic joint	Alberton lava	WDL
S9	Serecitic joint	Medium grained argillaceous quartzite	Oryx
S10	Fracture	Main bird quartzite	Elandsrand
S11	Fracture	Kimberly/Elsburg quartzite (Moderately siliceous)	WDL

Table 4.3.6.1 Samples used in the fractal dimension study

As no equipment for roughness profile measurement is available at Miningtek, a laser scanner at Natal University was used. This allows 3D profiles of the surfaces to be obtained from various 2D scanlines. The mechanical setup however only allows a minimum distance between adjacent points or lines of 0.25 mm. The method to scan the surface (e.g. peel manufacture) has been described in Jermy (1995). The profiles obtained for sample S1 (a typical lava discontinuity surface) and S5 (a typical quartzite discontinuity surface) are illustrated in figure 4.3.6.1. Any 2D profile can be extracted from this data for analysis.

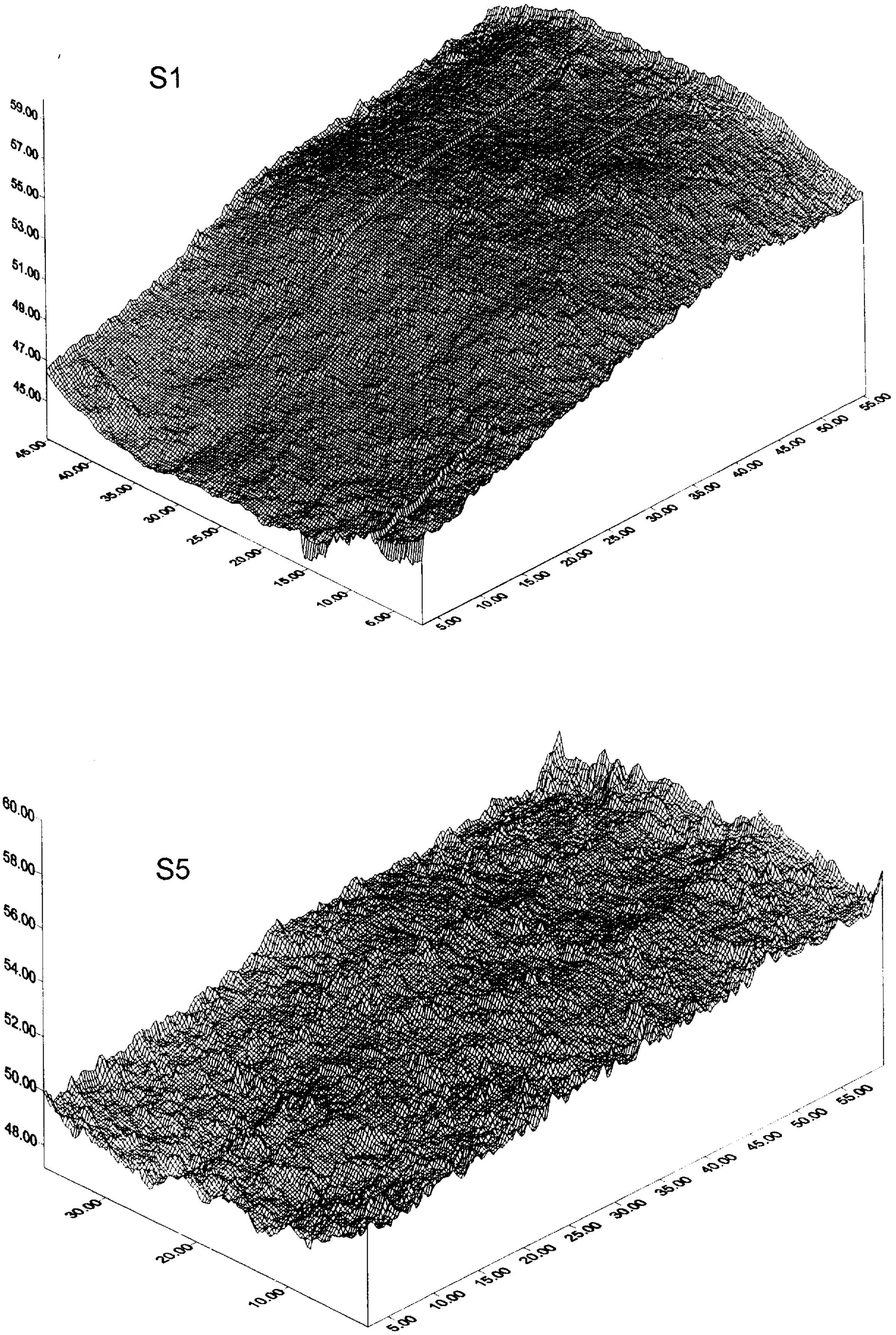

Figure 4.3.6.1 Typical 3D roughness profiles

Fractal analysis

A fractal set can be defined as

$$N = \frac{C}{r^D} \tag{4.3.6.2}$$

(Turcotte 1993) where N is the number of objects with a characteristic linear dimension r. C is a constant of proportionality and D is the fractal dimension. The length of the perimeter L of a fractal object is given by

$$L = rN \tag{4.3.6.3}$$

Substituting 4.3.6.2 in 4.3.6.3 gives

$$L = \frac{C}{r^{D-1}} \tag{4.3.6.4}$$

Taking the log on both sides leads to

$$\log(L) = I + (1 - D)\log(r) \tag{4.3.6.5}$$

Assuming the roughness profiles are self-similar the fractal dimension can be calculated by using equation 4.3.6.5 and the divider method. A divider is set to a particular span (r) and "walked" along the profile. The number of divider steps to cover the profile multiplied by the divider span gives an estimated profile length (L). This is repeated several times and the profile length as a function of divider length is plotted in log-log space. The slope of the curve is equal to $(1 - D)$. The intercept on the y-axis is equal to I.

The divider method used in this study is similar to the modified method used by Brown (1987) and McWilliams et al. (1995). This consists of using horizontal divider spans rather than walking the dividers along the profile. A computer program was written to ease the calculation of D. A least squares method is used in the program to obtain the straight line fit in log-log space.

If the profile is self-similar, the divider method will always give the correct value for D. The profiles obtained for the rock surfaces are however not self-similar but self-affine. This implies that when viewing the profile at different scales, the horizontal and vertical axis must be multiplied by different scaling factors for the profile to retain similarity. Caution however needs to be exercised when using the divider method for self-affine profiles. If the sampling interval is bigger than the so-called crossover length as defined by Brown (1987), the divider method will give a fractal dimension close to 1. The solution is to multiply the ordinate by a constant greater than 1 to increase the effective crossover length. The crossover length need not be known ahead of time. One can multiply the profile height repeatedly by increasing factors till a stable estimate of D is obtained.

To illustrate the method the fractal dimension for a 2D profile extracted from the S5 data file was calculated (figure 4.3.6.2).

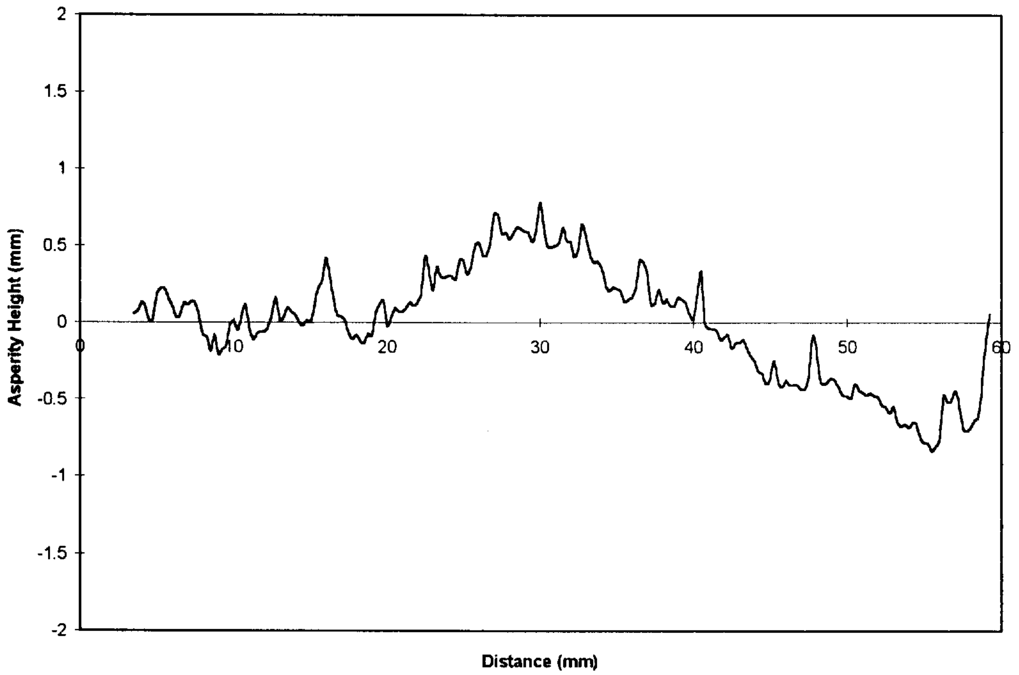

Figure 4.3.6.2 2D roughness profile (Sample S5)

The fractal dimension for this curve was calculated using the divider method with the vertical component multiplied by various factors. The calculated fractal dimension as a function of multiplier is displayed in figure 4.3.6.3. It is clear that a stable value is obtained for a multiplier of more than 300. Figure 4.3.6.4 illustrates the estimated profile length as a function of divider span in log-log space for a multiplier value of 500. The data points lie more or less on a straight line as is expected for the self-affine curve. The straight line was fitted using a least squares method.

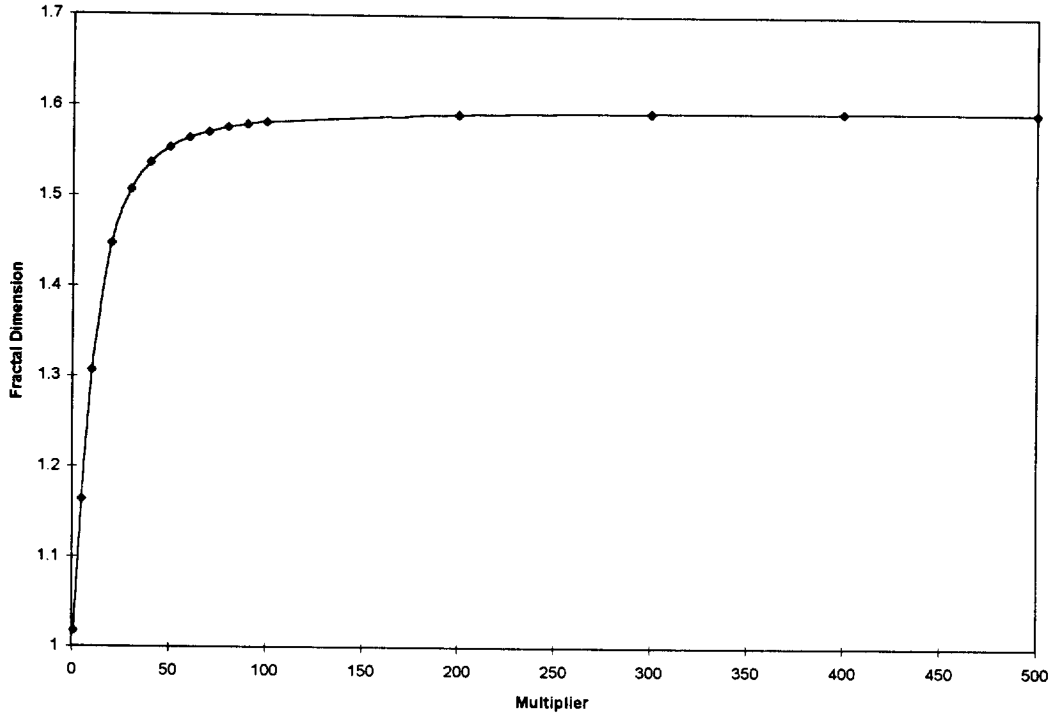

Figure 4.3.6.3 Fractal dimension calculated for various multipliers

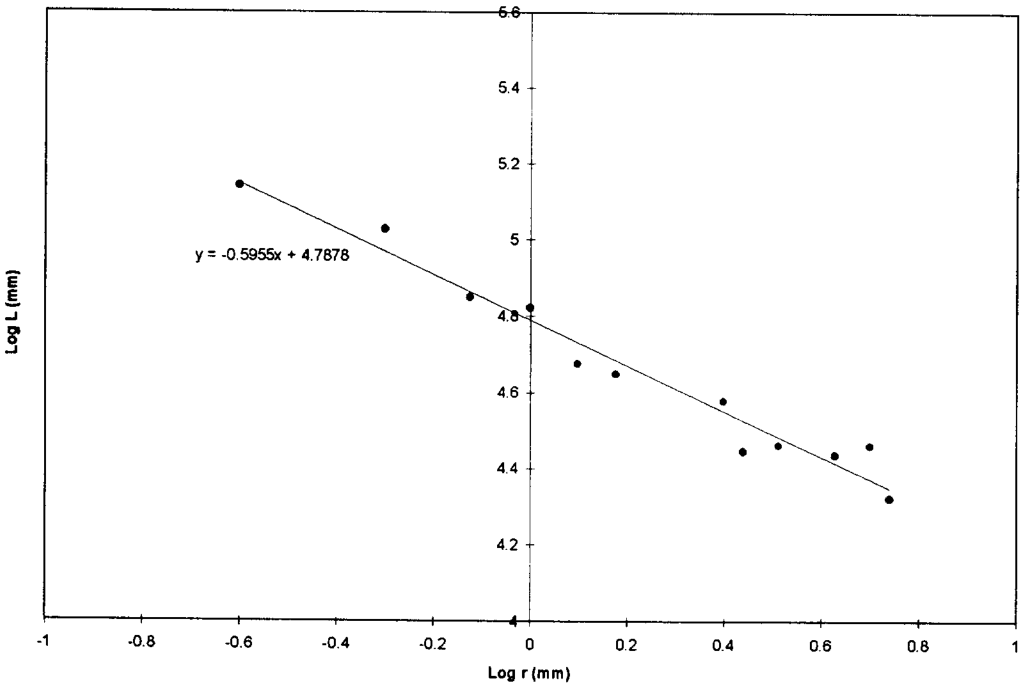

Figure 4.3.6.4 Trend of apparent length as a function of divider length.

An important question that remains however, is whether a single 2D roughness profile gives an accurate description of the overall 3D roughness. This is a fundamental problem and needs to be addressed no matter which technique of roughness determination is used. Unfortunately most of the work described in literature has concentrated on 2D roughness determination. For this study the problem was investigated by calculating the fractal values for all the 2D profiles making up a 3D surface. These values were plotted as a function of the spatial variable in the third dimension (the z-axis) to see if there is any significant deviation. Figure 4.3.6.5 illustrates the trends obtained for S5 (Figure 4.3.6.2).

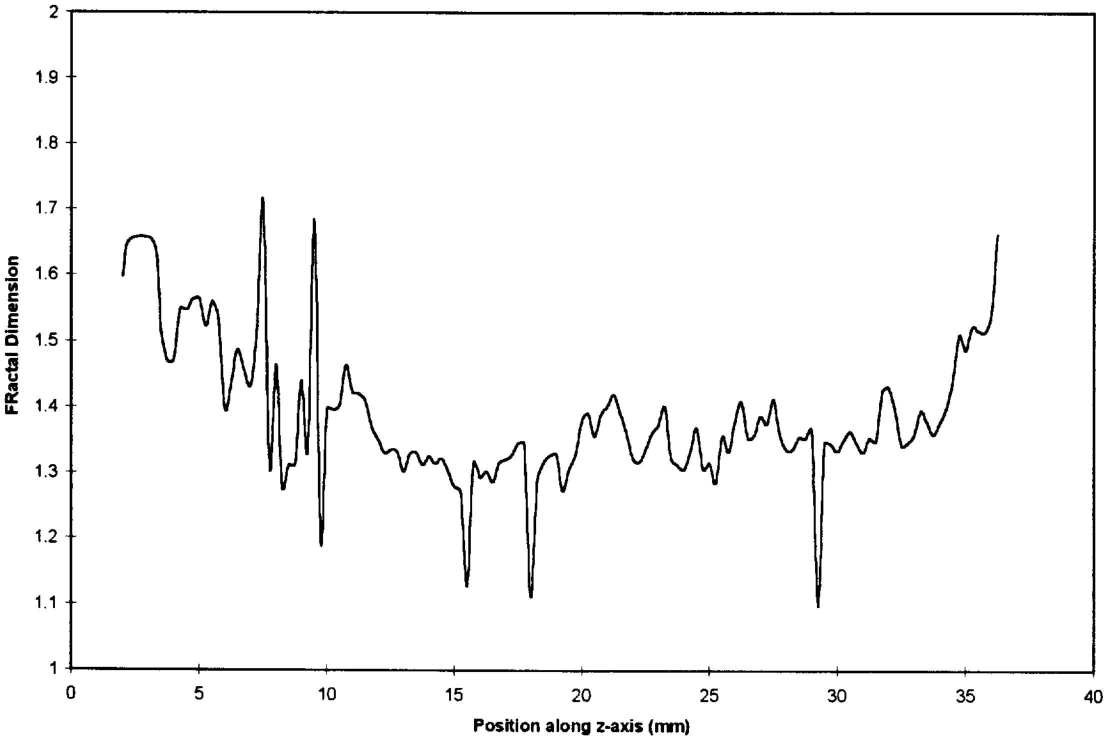

Figure 4.3.6.5 2D Fractal dimension as a function of position along the third axis

What is very noticeable is that there is a very big difference in the fractal dimension for 2D profiles from point to point along the third dimension. This was repeated for all the samples with a statistical summary given in table 4.3.6.2.

SAMPLE	AVERAGE D	AVERAGE I	STANDARD DEVIATION IN D
S1	1.1063	5.0537	0.04744
S2	1.1051	4.9417	0.06754
S3	1.1556	4.8832	0.05433
S4	1.1562	5.1437	0.05113
S5	1.1928	4.9725	0.07453
S6	1.3839	4.8422	0.07794
S7	1.2187	5.1966	0.062705
S8	1.2995	4.9781	0.067077
S9	1.2103	4.9373	0.05495
S10	1.2103	4.8888	0.07231
S11	1.2184	4.9734	0.07495

Table 4.3.6.2 Calculated fractal values for the different specimens

Conclusion

The work reported here demonstrates the use of fractal dimension as a roughness parameter for 3D discontinuity profiles. Currently the average fractal dimension of a number of 2D profiles is used as roughness parameter. Further work is however required to gain a better understanding of 3D joint roughness.

An important result illustrated in this preliminary study is the very noticeable difference in the fractal dimension for 2D profiles from point to point along the third dimension. Care should therefore be exercised when using single 2D roughness parameters to describe 3D behaviour.

References

Barton, N. (1976) *Int.J.Rock Mech. & Geomech. Abstr.*, vol. 13, pp. 255-279.

Barton, N. and Choubey, V. (1977) The shear strength of rock joints in theory and practice. *Rock Mech*, vol. 10, pp. 1-54.

Brown S.R.(1987) A note on the description of surface roughness using fractal dimension. *Geophys. Res. Lett.*, vol. 14, pp. 1095-1098.

Brown, S.R. and Scholz, C.H. (1985) Broad bandwidth study of the topography of natural rock surfaces. *J. Geophys. Res.*, vol. 90, pp. 12575-12582.

Cook, N.G.W., Hoek, E., Pretorius, J.P.G., Ortlepp, W.D. and Salamon, M.D.G. (1966) Rock Mechanics applied to the study of rockbursts. *J. S. Afr. Inst. Min. Metall.* vol. 66, pp. 435-528.

Crawford A.M. and Curran J.H. (1983) A displacement discontinuity approach to modelling the creep behaviour of rock and its discontinuities. *Int. J. Num. Anal. Meth. Geomech.*, pp. 245-268.

Crouch, S.L. (1979) Computer simulation of mining in faulted ground. *J. S. Afr. Inst. Min. Metall.*, pp. 159-173.

Flügge, W. (1975) *Viscoelasticity.* 2nd ed. New York, Springer-Verlag,

Güler, G. (1994) Personal Communication, Unpublished data, Deelkraal Gold Mine.

Gürtunca R.G. (1989) Results of a classified tailings monitoring programme at Vaal Reefs. *COMRO Int. Rep.*, no 614.

Gürtunca R.G., Jager A.J., Adams D.J. and Gonlag M. (1989) The in situ behaviour of backfill materials and the surrounding rockmass in South African gold mines. *Proc. 4th Int. Symp. of Mining with Backfill.* Montreal (Canada),

Hodgson, K. (1967) The behaviour of the failed zone ahead of a face, as indicated by continuous seismic and convergence measurements, *C.O.M. Res. Rep. 31/61*, Transvaal and Orange Free State Chamber of Mines Res. Org.

Jermy C.A., (1995) A laser scanning device to measure joint surface roughness. In: H.P. Rossmanith (ed), Mechanics of jointed and faulted rock. pp. 169-174.

Kersten, R.W.O. (1994) Personal Communication, Unpublished data, Hartebeesfontein Gold Mine.

Leeman, E.R. (1958) Some measurements of closure and ride in a stope of the East Rand Proprietary Mines. *Pap. Ass. Min. Mngrs., S.Afr.* vol. 1958-1959, pp. 385-404.

Malan, D.F. (1995) A viscoelastic approach to the modelling of the transient closure behaviour of tabular excavations after blasting. *J. S. Afr. Inst. Min. Metall.* pp. 211-220.

McGarr, A. (1971) Stable deformation near deep-level tabular excavations *J. Geophys. Res.* vol. 76, no 29, pp. 7088-7106.

McWilliams, P.C., Kerkering, J.C. and Miller, S.M., (1995) Fractal characterisation of rock fracture roughness for estimating shear strength., In: H.P. Rossmanith (ed), Mechanics of jointed and faulted rock. pp. 331-336.

Ortlepp, W.D. and Cook, N.G.W. (1964) The measurement and analysis of the deformation around deep, hard rock excavations. *Proceedings 4th International Conference on Strata Control and Rock Mechanics.* pp. 140-150.

Power, W.L., Tullis, T.E., Brown, S.R., Boitnott, G.N. and Scholz, C.H., (1987) Roughness of natural fault surfaces. *Geophys. Res. Lett.*, vol. 14, pp. 29-32.

Ryder, J.A. and Napier, J.A.L. (1985) Error analysis and design of a large scale tabular mining analyser. *Proceedings 5th International Congress on Numerical Methods in Geomechanics.* Nagoya, pp. 1549-1555.

Ryder, J.A. and Officer, N.C. (1964) An elastic analysis of strata movement observed in the vicinity of inclined excavations. *J. S. Afr. Inst. Min. Metall.* vol. 64, pp. 219-244.

Salamon, M.D.G. (1968) Two-dimensional treatment of problems arising from mining tabular deposits in isotropic or transversely isotropic ground. *Int. J. Rock Mech. Min. Sci.*, vol. 5, pp. 159-185.

Salamon, M.D.G. (1974) Mechanics of underground excavations. *Proceedings 3rd Congress of the International Society for Rock Mechanics*, pp. 951-1099.

Salamon, M.D.G., Ryder, J.A. and Ortlepp, W.D. (1964) An analogue solution for determining the elastic response of strata surrounding tabular mining excavations. *J.S. Afr. Inst. Mining Met.*, vol. 65, pp. 115-137.

Tse and Cruden, (1979) Estimating joint roughness coefficients, *Int.J.Rock Mech. & Geomech. Abstr* , vol. 16, pp. 303-307.

Turcotte, D.L., (1993) Fractals and chaos in geology and geophysics. Cambridge University Press.

4.4 SIMULATION OF LARGE SCALE FRACTURING AND FAILURE

A summary of practical applications of large scale fracturing and failure is presented in this section. It is closely related to objective 3.4: "Simulate combinations of support and mining strategies that can be used to engineer the fracture zone to behave in the most inherently stable manner in particular geological environments", objective 3.5: "Evaluate field observations which could be used to to control the characteristics of the fracture zone" and objective 3.6: "Investigate the qualitative changes in fracture zone stability and extent as the mining depth is increased".

4.4.1. Formation of a pattern of wedges ahead of a stope face

The formation of a pattern of fractures ahead of an advancing stope face in the form of wedges is demonstrated in figures 3.4.4 and 3.4.5. These are shear fractures and should be clearly recognised as such when exposed in hanging and footwalls. When these fractures are not observed regularly, this mechanism is not active. The presence of such wedges will result in a potential for crushing and horizontal dilation ahead of the stope face with subsequent consequences. This mechanism has been proposed by Roering (1979) and Brummer (1986) and may apply to particular geological areas and stress conditions; the absence of a regular set of shear fractures will exclude this mechanisms in other cases however.

4.4.2 Potential for locked in stresses due to inelastic shear deformations

This mechanism has been described in detail by Kuijpers and Napier (1991) and relies on the presence of discontinuities being subjected to shear slip during loading and unloading as a result of stope advancement. The formation of shear fractures ahead of a stope face would be a potential generator for this mechanism, but the presence of existing discontinuities such as suitably orientated joints and faults would also allow the mechanism to operate. Figure 4.4.1 shows the effect of locked in shear displacements on the convergence of a stope hangingwall. Except for the obvious additional inelastic deformations it can be seen that after a few mining steps the curvature in the closure profile is reversed as compared to the elastic or single step inelastic analysis. The curvature of the closure profile is directly related to the stress in the

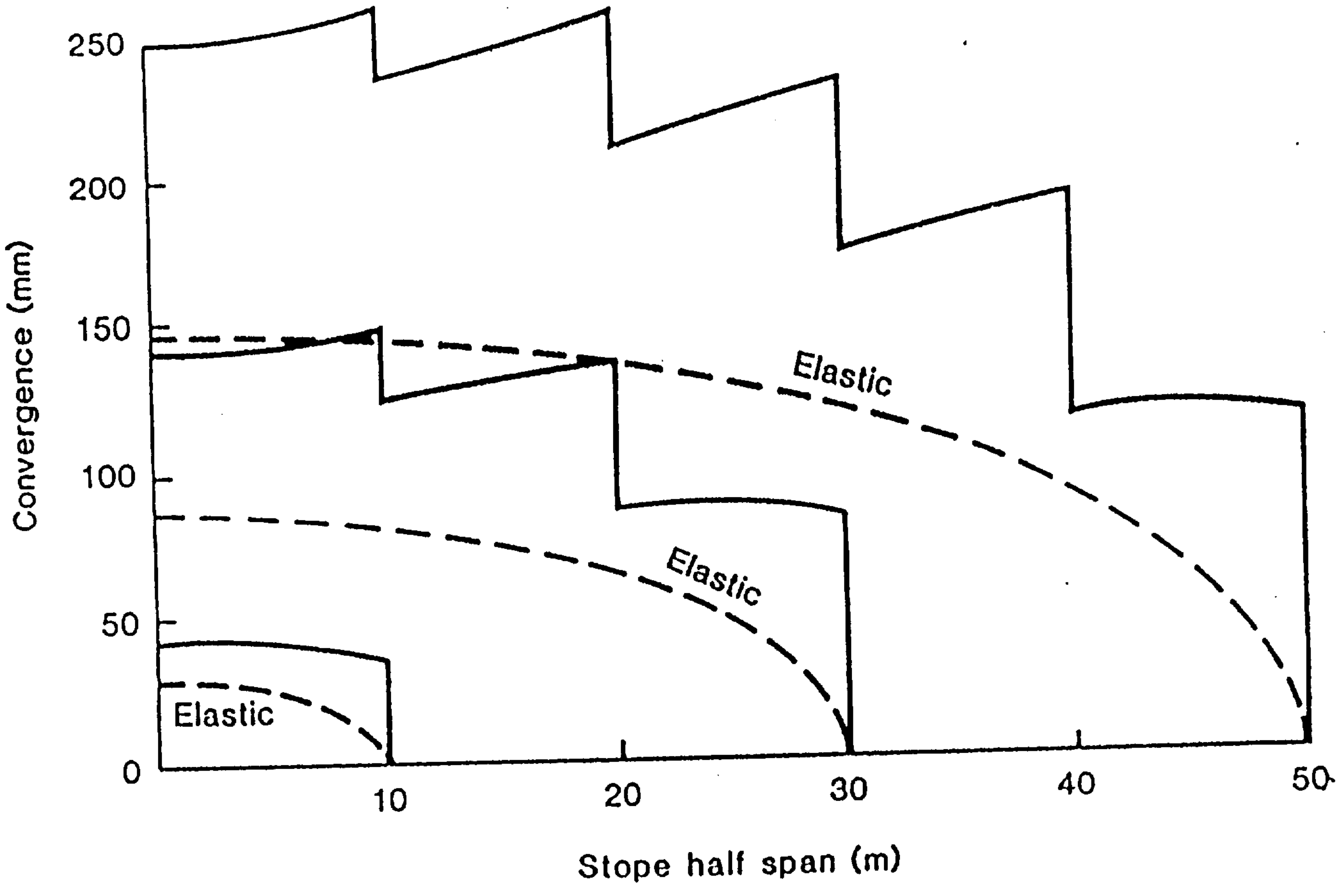

Figure 4.4.1 Vertical displacement of a stope hangingwall after various mining steps

skin of the excavation (in this case the stope hangingwall) and a reversal in curvature is thus associated with a reversal in hangingwall stresses from tensile to compressive.

4.4.3 Development of an increased effective stoping width due to extension fractures initiated from mobilised bedding planes (or other discontinuities).

Natural discontinuities such as bedding planes, joints and faults near an advancing stope face present potential initiation sites for mining induced fractures as tensile stresses can be induced due to shear slip along such discontinuities. Such large scale 'flaws' will always be the weakest link in the 'failure chain' and need to be identified before any other form of failure analysis is undertaken. Figure 4.4.2. shows the resulting tensile fracturing pattern due to the presence of bedding planes. Even though the ratio between the horizontal and vertical virgin stress is 0.5, the tensile fractures do assume an almost vertical inclination. This is due to the limited shear resistance of the bedding planes, which restricts the formation of a shallow arch, similar to the elastic situation, above the stope. Instead a higher arch, changing the stress orientations and affecting the fracture orientations, has to develop. If tensile fractures generated from bedding planes at various levels are joined, an additional and even more dramatic heightening of the arch takes place. Effectively the stoping width is increased by the vertical extent of the tensile fractures and the potential for failure ahead of the stope face is increased in response to this change in geometry. A similar mechanism is presented by Napier and Hildyard (1992). It can be appreciated that one of the consequences of this mechanism is the potential for the formation of an asymmetric fracture pattern around an advancing stope with a different geological structure in hanging- and footwall. The effective widening of the stope may in such a situation only take place in either hanging or footwall instead of affecting both equally. In such a case the actual stope will be located either at the bottom or the top of the “effective” stope and the stresses ahead of the stope will be inclined with respect to the vertical direction. Such a mechanism may explain the observation of different fracture patterns around stopes in various geological areas.

4.4.4. Combined effect of layered rock and 'crushing' ahead of a stope face.

The effect of crushing of rock ahead of a stope face or the sole effect of the presence of bedding planes does not appear to have a major influence on the behaviour of rock around a

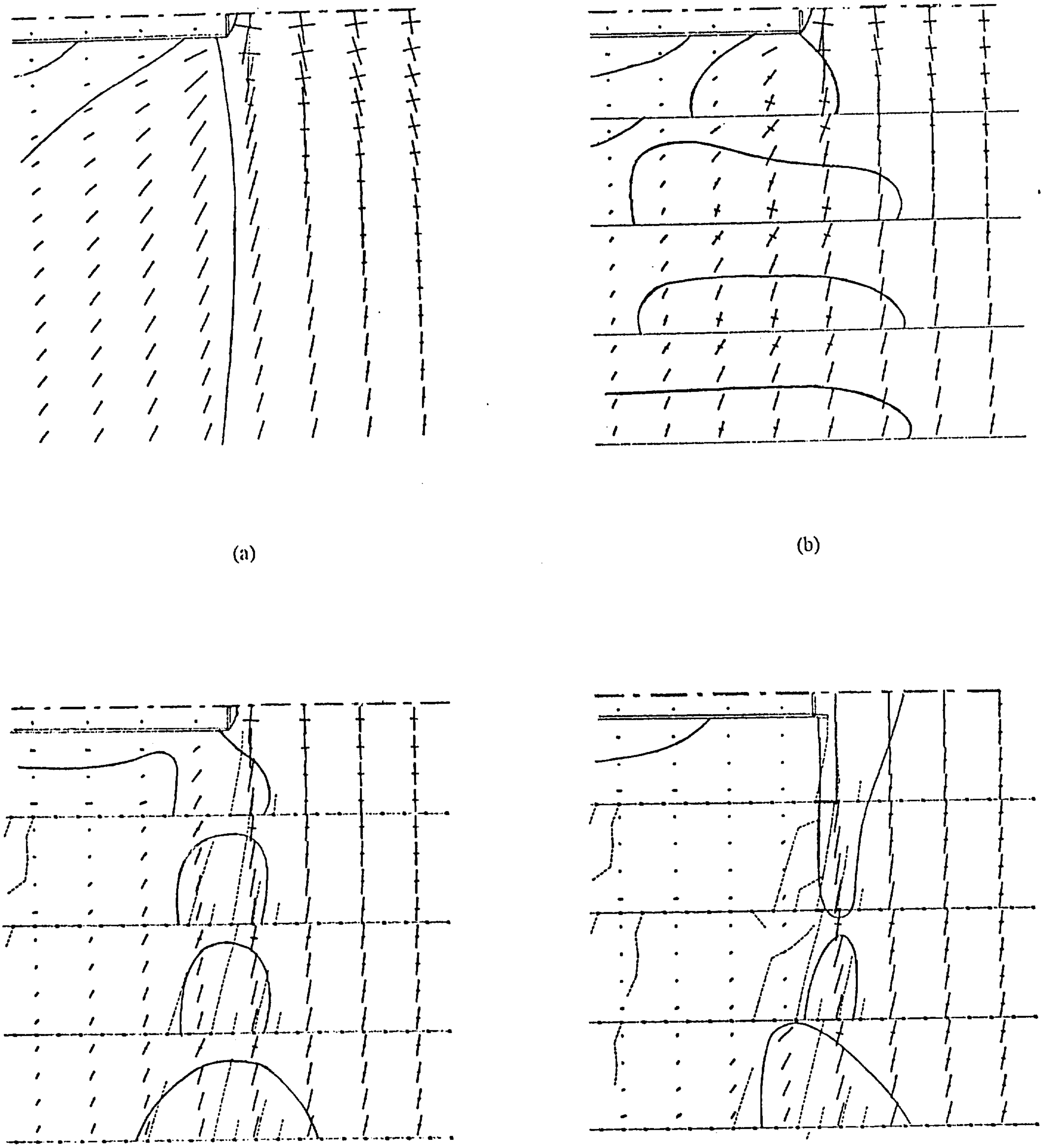

(a) (b)

(c) (d)

Figure 4.4.2 Stress distribution and potential failure around a stope (a) elasticand homogeneous medium , (b) elastic medium containing bedding planes (c) after the formation of extension fractures from the bedding planes (d) after the joining of the extension fractures stope, but the combination of these two mechanisms results in a confinement of dilatational movements within the layers close to the stope (Kuijpers, 1992). This is a mechanism for effective compression of the skin around a longwall stope and is also the basis for successful caving operations (Arnold, 1993). The success of the caving mining method is mainly associated with the stability of the hangingwall due to compressional horizontal forces induced by dilation. An absence of such forces would lead to unstable hangingwall conditions in the area between the stope face and the cave, as support is not designed to accommodate bedded rock without horizontal confinement. Figure 4.4.3. shows the resulting horizontal stress distribution from the described mechanism.

4.4.5 Potential for slabbing as a combined effect of localised damage (crushing) and secondary extension fracturing due to induced tensile stresses.

This mechanism is proposed as an alternative to shear fracturing. The basic assumption is the formation and existence of a narrow crushing zone. Crushing fractures, referred to as 'normal shear' fractures have been reproduced by Lajtai (1974) and Martin (1993) also indicates the potential for such features. Figure 4.4.4.a shows the resulting tensile fracture formation after the emplacement of a narrow crushing zone in the area with the highest potential for failure in the sidewall of a tunnel in a biaxial stress field. The tensile fractures are the secondary fractures as described in section 3.4. and initiate inside the rock. Figure 3.4.8. shows similar fractures around a hole in a quartzite specimen. The mechanism which is shown here represents the spalling process. If the crushing zone were to be extended further, the potential for (secondary) tensile fracturing becomes exhausted and the spalling process will not continue any deeper into the rock.. The strength of the narrow crushing zone will be strongly affected by the amount of confinement acting on it and since the width to height ratio of the crushing zone increases relatively rapidly as the spall becomes deeper, the effect of a (small) confining stress on the spalling process will be relatively large as well. Martin (1993) observed for instance that only the weight of a muck pile, acting as confinement on the spall of the experimental tunnel, reduced the depth of the spalled region considerably. Figure 4.4.4.b shows the formation of parallel slabs next to a tunnel sidewall due to the formation of a crushed 'notch' in the corner of the tunnel. Tensile stresses, as induced by this notch, are essential for the formation of these extension fractures. Their spacing is controlled by the tensile strength of a critical flaw in the side wall and the geometry and size of the opening. The

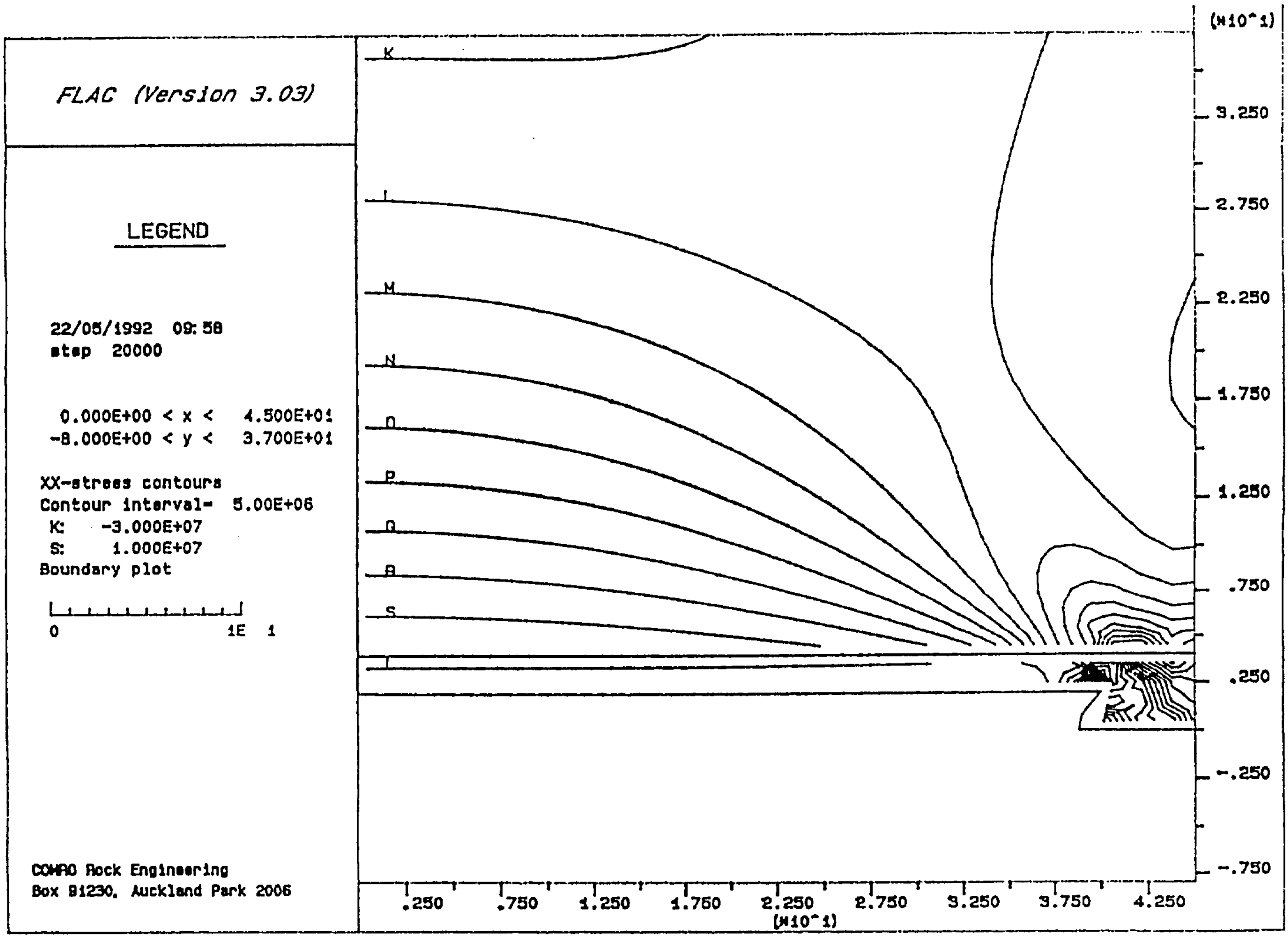

Figure 4.4.3 Horizontal stress distribution around stope with a layered hanging wall and an area ahead of the stope face which is plastically deforming (FLAC)

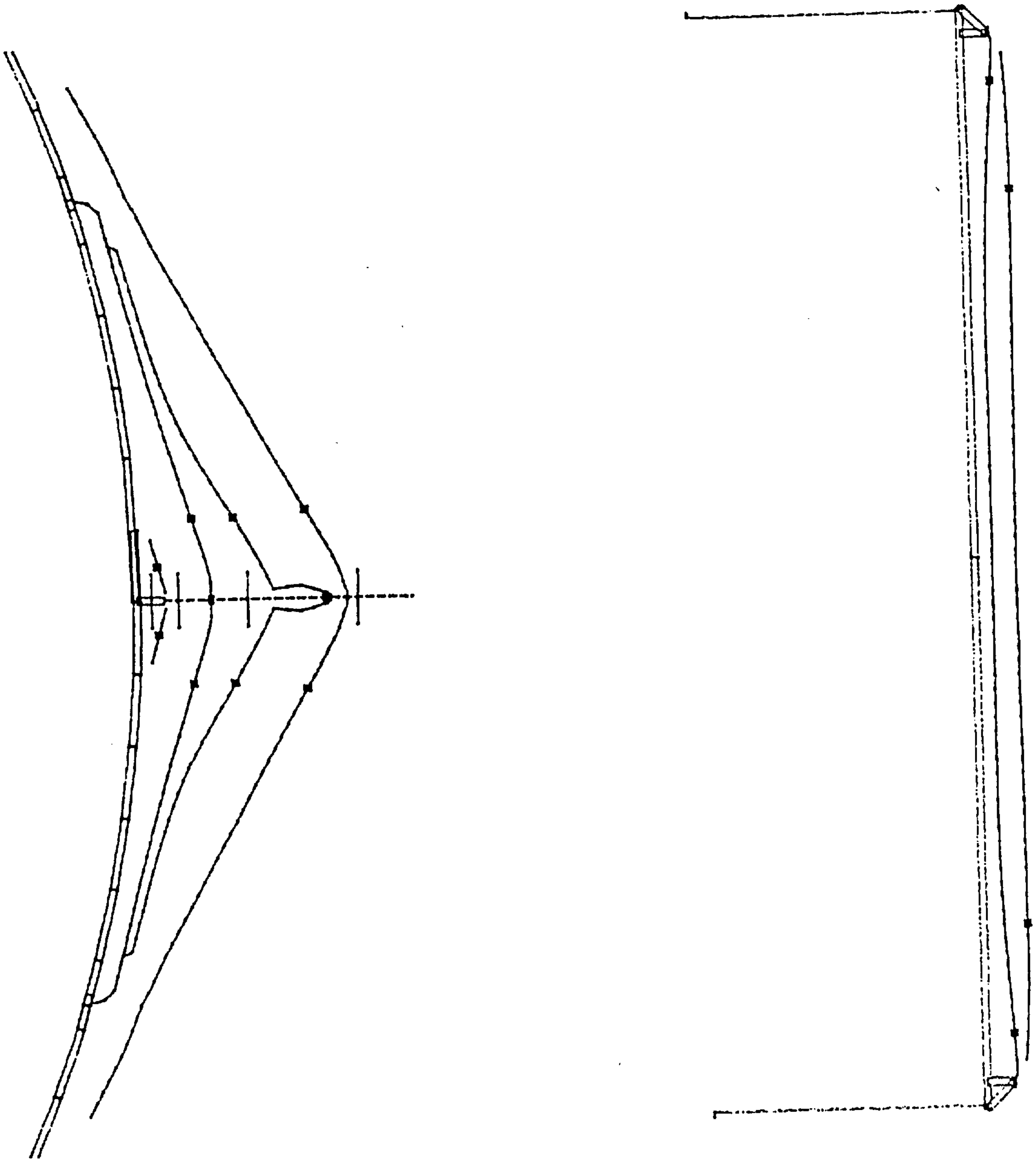

(a)

(b)

Figure 4.4.4. Formation of tensile fractures due to the presence of a crushing zone (a) formation of a dog-ear in the side wall of a borehole (b) formation of slabs in the side wall of a rectangalar tunnel.

formation of additional fractures in the tunnel sidewall must be preceeded by an expansion of the notch.

4.4.6 An upper bound for the extent of the inelastic area above a longwall stope

Backfill measurements (Gurtunca et al., 1989), indicate that differential inelastic vertical movements are initiated when the backfill pressure exceeds 1 MPa and cease when this pressure exceeds around 3 MPa. This suggests that a pressure of 3 MPa is required to reverse previous inelastic movements. If these inelastic movements are assumed to be induced by gravity of fractured rock only, then a simple estimate of the height of the effective fractured zone, based on a rock density of 2700kg/m^3 would be approximately 100m. This value is similar to the height of an arch which could be expected to develop over a longwall stope. If only gravity is opposing the support forces from the backfill, it is possible to conclude that the rock below the arch is completely fractured. Even in the extreme case of a completely fractured rockmass, only that portion of the rockmass which is situated below the arch would be affected by recompression stresses generated by the support. The fact that only 100m of rock is affected by recompression stresses can be contributed to the compressional stresses in the arch itself, which would prevent any opening or sliding of discontinuities. No inelastic movements are possible inside and above the arch; only the area underneath the arch is affected. The arch spans from abutment to abutment and its height is directly related to the span of the stope and the strength of the overall rockmass including all discontinuities.

If not only gravitational forces are controlling the resistance against backfill stresses during inelastic recompaction, but some form of wedging and subsequent additional resistance is mobilised, the affected height of rock will be reduced, depending on the relative contribution of the additional resistance. The pressure of 3 MPa would in that case be associated with the weight of a fractured zone of less than 100m plus a contribution from additional resistance. Only appropriate measurements can provide the required information, but the value of 100m would at least be a conservative working estimate for support design.

4.4.7 Potential for changes in elasticity modulus due to micro fracturing.

Micro fracturing in rock causes a reduction of stiffness. Most rocks will be damaged due to microfracturing after being retrieved from their natural environment. A practical effect of the presence of these microfractures is the sensitivity of the stiffness of the rockmass to the volumetric stress. As long as the microfractures are not completely closed, the stiffness of the rock can be substantially reduced compared to rock which does not contain such micro fractures. Some rocks appear to be more sensitive than others, but reductions of more than 50% for sandstone, 30% for norite and 25% for quartzite have been reported (Stravropoulou, 1982). Larger variations are possible, especially for porous rocks. The immediate practical implication of the sensitivity of the stiffness of rock with respect to the volumetric stress applied to the rock, is the incorrect assumption of linear elasticity in the computer modelling which could lead to incorrectly computed stress distributions. As an example, the modelling of laboratory tests on cylindrical specimens with different width to height ratios is shown. Assuming linear elasticity, the vertical stress distribution across the pillar is as shown in figure 4.4.5a; however by assuming a stiffening effect of the volumetric stress component, the vertical stress distribution has changed as is shown in figure 4.4.5b. The stresses at the pillar walls are substantially lower than in the linear elastic case, because the core of the pillar, which has become relatively stiffer due to the larger confinement imposed on it, has attracted a relatively larger proportion of the pillar load than the side walls, which have maintained their reduced stiffness. The effect on the failure of the pillar is substantial; as the stresses in the pillar sidewall are substantially reduced, an increased average pillar stress would be required to initiate failure in the pillar sidewall. The effect is stronger for wider pillars. Inelastic modelling, assuming an initial linear elastic behaviour, would not have been able to simulate correctly the effect of the width to height ratio on the failure strength of the pillar. Appropriate non linear elastic modelling would at least be able to predict the onset of failure correctly. Pronounced sensitivity as described above has been observed with specimens of chromitite from Impala platinum, but it is not unlikely that other rocks may demonstrate similar effects , be it to a lesser extent.

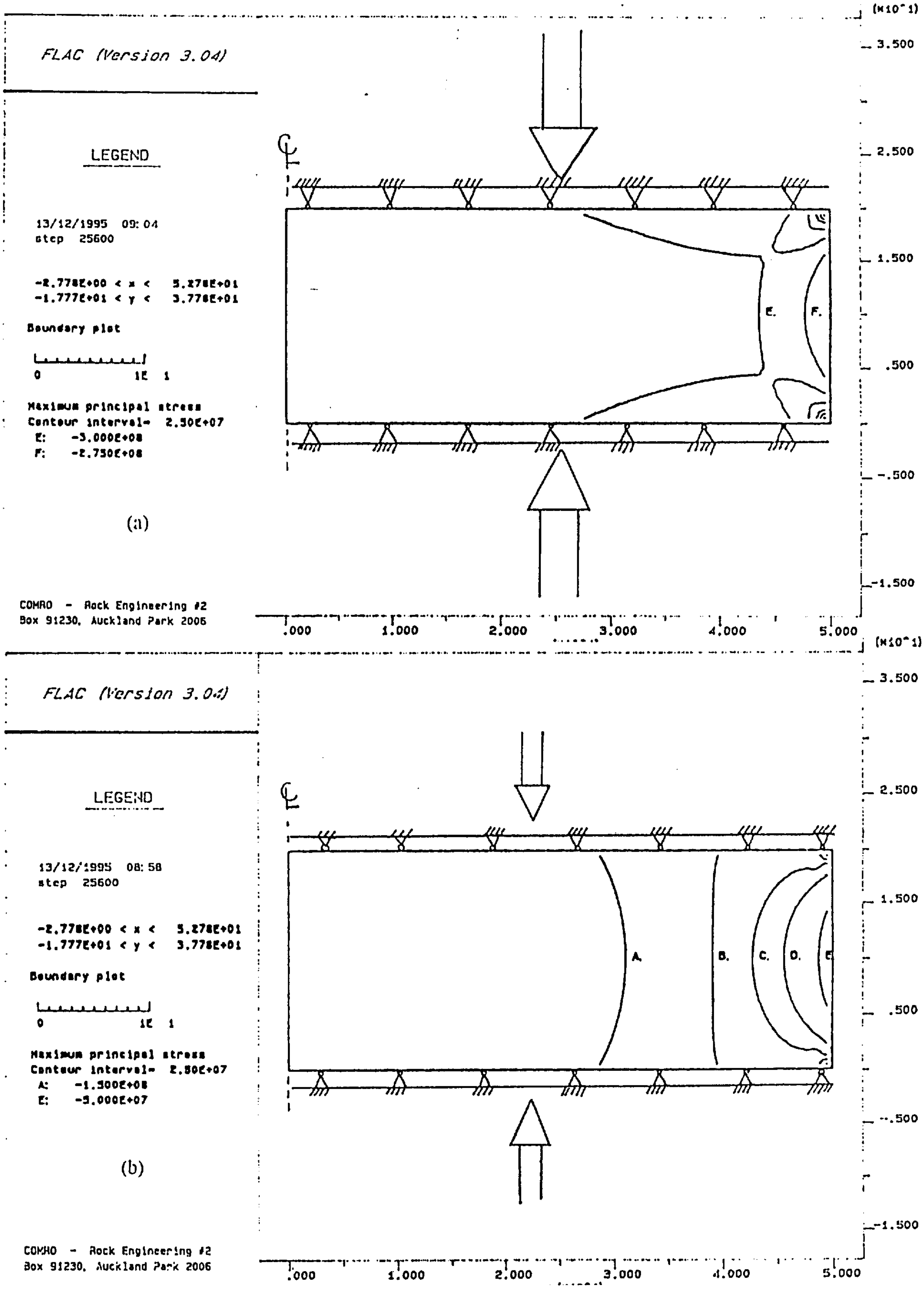

Figure 4.4.5. Vertical stress distribution in a circular pillar loaded between infinitely stiff platens restraining any slip (a) linear elasticity (b) elasticity modulus increases with confinement.

4.4.8 Potential for reduced rockmass strength due to stress rotations

Another possible effect of microfracturing has been raised by Martin (1993). According to him, stress rotations may have a weakening effect once the process of microfracturing is initiated. Figure 4.4.6 demonstrates the potential for microfracture extension by a rotating stress field; a microfracture which is initially aligned with the major principal stress direction will find itself inclined with respect to the major principal stress after the stress rotation; sliding along the microfracture will induce tensile stresses and allow for further microcrack growth. If the process is repeated, microfracture extension and associated damage accumulation is possible at any stress level which exceeds the initiation threshold of micro fracturing. As this level is typically 30%-50% of the failure strength which is observed under normal circumstances, the potential for such a mechanism should be seriously considered as it may affect the in situ strength of a rockmass considerably. An advancing excavation would typically induce rotating stresses in the rock mass surrounding it and if those rotating stresses would effectively increase the damage in the rockmass, then the strength of that rockmass may be reduced.

The stress path leading to failure is not assumed to influence the strength of rock in current rock engineering practice; however the evidence for this statement is obtained from laboratory tests in which no rotation of the stress field occurred, only the sequence of (biaxial) loading was varied. A new loading rig for laboratory specimens has been designed which will allow the principal stresses to rotate effectively by applying a varying torsional moment in addition to the standard triaxial load. Tests, conducted with this new loading rig, should be able to analyse the potential for the proposed mechanism.

4.4.9 Effect of stope span and depth on the potential for violent failure (rockbursts) along discontinuities

Ryder (1988) reported that 'an increase in the depth of mining of an isolated stope should in theory be accompanied by a reduction in the magnitude of the associated events', because the open span of a stope with a particular stoping width decreases with increasing mining depth and the zone which is disturbed by mining induced stresses is directly related to the mining span. In the same paper Ryder also mentioned that 'This observation is not well substantiated

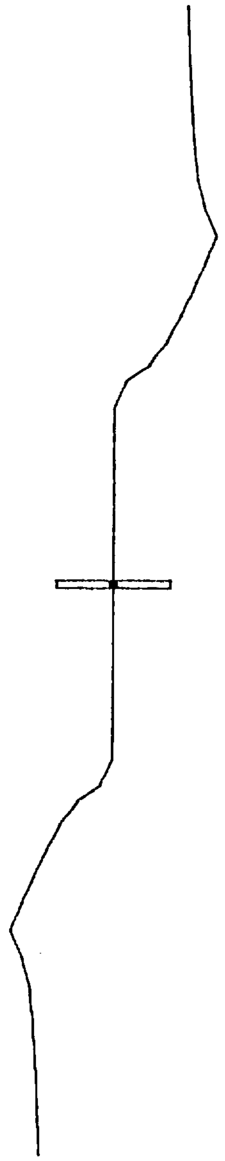

Figure 4.4.6. Effect of rotating stress field on microfracture extension (DIGS).

by seismic or other data,' and it is essential that this observation should be considered carefully; apparently there is a discrepancy between the results of theoretical analyses and recorded behaviour.

The following is an attempt to address this difference: a potential fault without inherent strength will slip without inducing a stress drop or associated seismicity. The model, which is based on the disturbance caused by a longwall stope approaching a discontinuity, becomes questionable at depths shallower than 2000 m - 3000 m. At such depths the theoretically open longwall span exceeds 300 m x 300 m for a 1 m stoping width (figure 4.4.7) For practical reasons such dimensions will not be reached and it is therefore not possible to infer seismicity trends at depths shallower than 2000 m - 3000 m with this model. Figure 4.4.7 does however give an indication of the potential for seismicity with increasing depth based on the assumption of a tabular long wall stope.

Artificial reduction of Excess Shear Stress (ESS) by leaving pillars and placing backfill in order to reduce the effective stoping span, is considered to be good practice for rockburst prevention; however attempting to reduce ESS may only succeed in reducing the amount of seismicity induced from slip on discontinuities. Triggering a small event which is located at a small distance from the working area could have a similar damaging effect (rockburst) as the initiation of a larger event at a larger distance from the area of interest. The effect of reducing the stoping span may only be reflected in the total amount of seismicity, while having a marginal effect on the potential for rockburst. Simulations with the computer program WAVE (described in chapter 2) have shown that the problem of a stope approaching a fault and subsequently inducing violent slip along that fault, is scale independent with respect to the velocities generated around the stope. Although total seismicity increases with a larger stope span, the distance between the fault and the stope at the initiation of fault slip also increases with a larger stope span. Velocities around the stope are however not affected by a reduction in stope span and the potential for rockbursting may thus not have been reduced. Reducing ESS is therefore no guarantee for improved mining conditions.

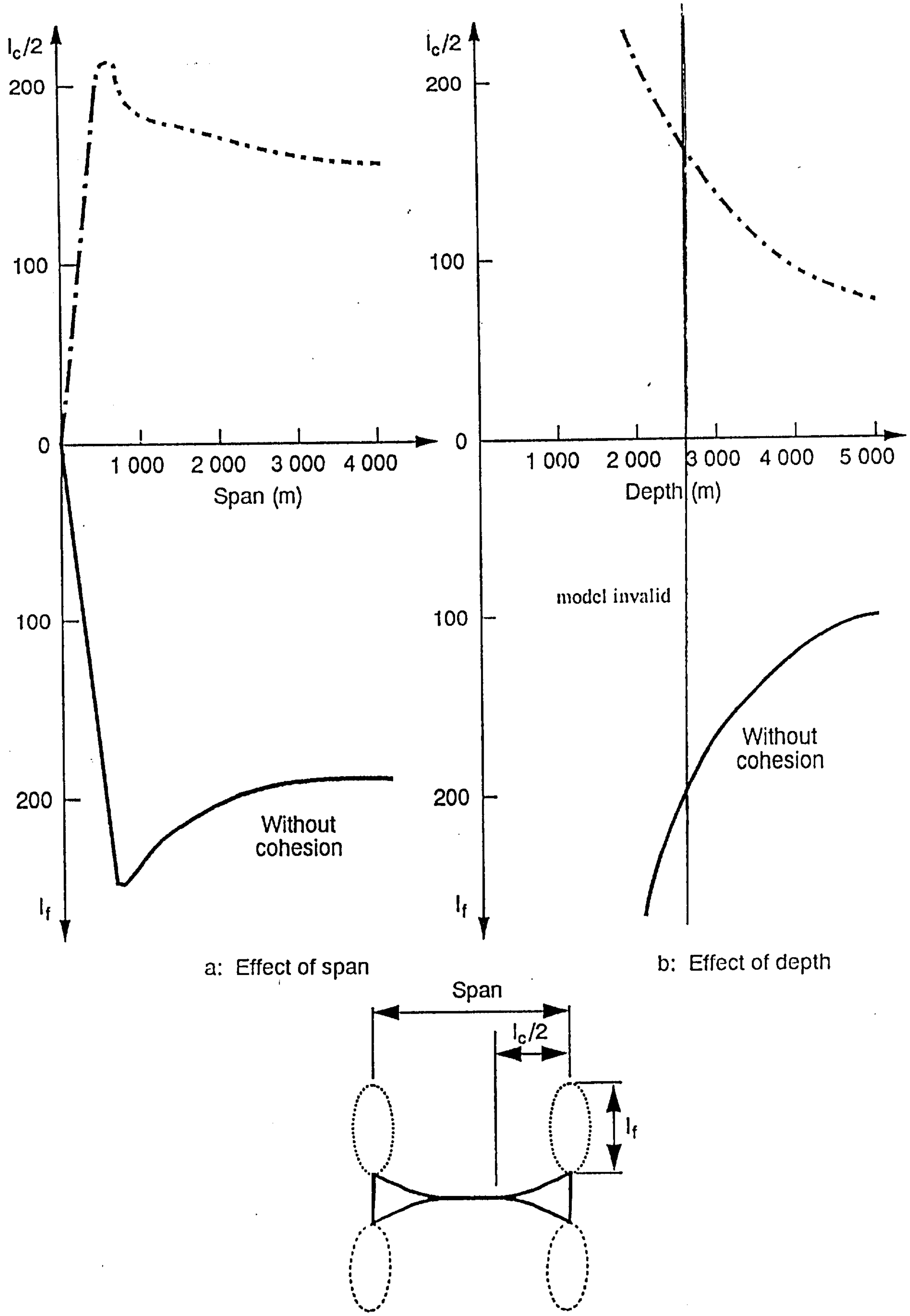

Figure 4.4.7. Relation between mining depth on open span and size of failure zone (ESS lobe)

4.4.10. Design of a rockburst resistant support system

At present the focus in rock engineering research is mainly on reducing seismicity, predicting seismicity and on avoiding seismicity as it is perceived that the only other alternative, namely the design of a support system which can resist any rockburst, is impossible.

Previous and recent (black box) monitoring has indicated that the (fractured) skin around deep level mining excavations is accelerated away from the solid rockmass while at the same time seismic waves are trapped in the fractured skin, after a seismic event has occurred nearby. Elastodynamic models have shown similar trends and both indicate an amplification by the fractured skin, which appears to have a negative influence on the effect of seismicity near underground openings. Support requirements are even more demanding, as the velocity and the mass of potential keyblocks are the critical parameters for support design (Wagner, 1984). This approach forms presently the basis for rockburst resistant support design but has not been properly tested. If the assumptions inherent in this design philosophy are too conservative, relaxation of them could lead to the design of more efficient support.

An alternative assumption is proposed here, namely the proper incorporation of the fractured hangingwall skin in the design of support. Under severe rockburst conditions it might not be necessary for the support to maintain the (fractured) skin in position; this requirement could be relaxed and the only function of the support in that case would be to maintain an opening which is completely covered by the support, providing a safe shelter for workers. This could be achieved by allowing the support to punch into the fractured skin (or in fact by allowing the skin to 'flow' around the support) in such a way that a sufficient opening can always be maintained. Punching of (small) support units is often observed and is regarded as an undesirable effect since the support is not designed to accommodate this ground movement. However by recognising the fact that the fractured skin has lost most of its strength it could be possible to design a support system which makes optimum use of this strength reduction. It would also be possible to 'precondition' the fractured skin in such a way that its properties could be engineered to make optimum use of the support capabilities. An alternative support strategy like this may prove to be a more practical way of combatting the effect of rockbursts on the loss of human life and, if proven to be effective, may even be used in combination with caving as a temporary support system capable of maintaining a safe working space near the stope face even under the most severe rockburst conditons.

Conclusions

Formation of a pattern of shear fractures ahead of a longwall stope in the form of wedges has been simulated .

Inelastic shear deformations can be responsible for locked in stresses during the process of mining.

Geological discontinuities can induce extension fractures around a longwall stope resulting in an increase of the 'effective' stoping width. This mechanism may explain the observation of different fracture patterns around stopes in different geological areas.

Crushing of rock ahead of a stope face in combination with the presence of bedding planes provides a mechanism for the effective compression of the skin around such a stope.

Crushing zones are a potential failure mechanism in rock and can induce secondary tensile fracturing. Spalling and slabbing are simulated based on this mechanism.

An upper bound for the height of the inelastic zone above a longwall stope is the height of the Vousoir arch over that stope. Backfill measurements indicate a potential height of approximately 100m.

Linear elastic behaviour may be an incorrect assumption for rock which has been damaged due to micro fracturing caused by removing rock from its highly stressed, natural environment.

Stress rotations, due to the mining process, may reduce the strength of in situ rock by extending micro fractures at relatively low stress levels.

A critical depth, at which seismic activity reaches a maximum, may exist.

Rockburst potential is not necessarily associated with the level of seismicity.

The potential for the design of a rockburst resistant support system may be enhanced by recognising and incorporating the reduced strength of the fractured skin around mine openings.

References

Arnold D.A., (1993) An evaluation of cave mining in weak hangingwall conditions at Hartebeestfontein gold minining company limited. MSc Thesis, University of the Witwatersrand, Johannesburg

Brummer R.K., (1986) Fracturing and deformations at the edges of tabular gold mining excavations and the development of a numerical model describing such phenomena. PhD Thesis, Rand Afrikaans University, Johannesburg

Gurtunca R.G., Jager A.J., Adams D.J. and Gonlag M. (1989) The in situ behaviour of backfill materials and the surrounding rockmass in South African goldmines. Proceedings Innovations in mining backfill technology, Balkema, Rotterdam, pp. 187-197

Kuijpers J.S., (1992) Effect of horizontal parting planes on hanging and footwall stability. Internal Note no. 07/92, COMRO, Johannesburg

Kuijpers J.S. and Napier J.A.L. (1991) The effect of loading history on stress generation due to inelastic deformations around deep level tabular stopes. J.S. Afr. Inst. Min. Metall., Vol. 91, no. 6, pp. 183-194

Lajtai E.Z., (1974) Brittle fracture in compression. Int. J. of Fracture, Vol. 10, pp. 525-536

Martin C.D., (1993) Strength of massive Lac du Bonnet granite around underground openings. PhD Thesis, University of Manitoba, Winnipeg, Canada

Napier J.A.L. and Hildyard M.W., (1992) Simulation of fracture growth around openings in highly stressed, brittle rock. J.S. Afr. Inst. Min. Metall., Vol. 92, no. 6, pp. 159-168

Roering C., (1979) Annual report for the Chamber of Mines of South Africa in fulfillment of research grant GTI P04, Rand Afrikaans University, Johannesburg

Ryder J.A., (1988) Excess shear stress in the assessment of geologically hazardous situations. J.S. Afr. Inst. Min. Metall., Vol. 88, no. 1, pp. 27-39

Wagner H., (1984) Support requirements for rockburst conditions, Proceedings first international congress on rockbursts and seismicity in mines, SAIMM, Johannesburg

5 CONCLUSIONS

Specific conclusions have been noted at the end of relevant sections in the main body of the report. General conclusions concerning the overall results of the research project are summarized with respect to the three main work areas.

In the elastodynamic work area, the finite difference computer program WAVE has proved to be of great utility in the solution of a number of simplified elastodynamic problems. Additional confidence in the performance of the program has been gained by comparing numerical results to photoelastic experiments of wave propagation in composite plates containing bonded or slipping interfaces between two different material types and with a centrally placed slot-shaped opening. It is recognized that the simplicity and efficiency of the WAVE code rests strongly on the restriction of an orthogonal grid structure. It is proposed that future work should explore the use of more general mesh structures or finite element methods and should address problems of simulating crack growth processes. These studies should be carried out in conjunction with analyses of observed rockburst mechanisms and explicit simulations of the interaction of seismic waves with discontinuity structures.

Simulations of simplified mining problems involving a single stope and fault combination has shown that two-dimensional elastodynamic analyses can over-estimate the predicted peak particle velocities as compared to empirical velocity-distance correlations whereas three-dimensional analyses seem to yield results that are closer to observed correlations. The back analysis of an actual seismic event, using a finite element code, has shown that a broad correspondence to particle velocity amplitudes can be obtained by adjusting the friction properties of an assumed source model but that more detailed replication of the observed motions requires a much more detailed knowledge of both the large scale rock mass behaviour and the source structure.

Progress has been made in controlling and understanding the nature of numerical instabilities in boundary element based elastodynamic numerical analyses. This approach offers great flexibility in analysing arbitrarily oriented fractures but in its present form the boundary element method is limited in the practical working size of elastodynamic problems that can be analysed. The possibility exists that this restriction could be removed for two-dimensional problems by adopting a volumetric body force formulation of the dynamic problem. In this case the necessity for maintaining a history of the elastodynamic solution at all previous time steps would be avoided. In addition, the so-called multipole technique that has been developed for the solution of large scale static problems of interacting cracks could be adapted for the efficient solution the dynamic body force problem.

The development of methods to analyse the mechanics of the stope fracture zone has been assisted by the use of the special purpose computer program DIGS that can be used to model fracture growth and can be employed to analyse multiple assemblies of interacting fractures. An improved solution technique (the "multipole" method) has been included in the program to allow analyses of several thousand elements to be performed. It must be noted, however, that it is still computationally arduous, and in certain cases not feasible to model crack growth problems requiring thousands of growth steps. This restriction remains a significant challenge to the development of a large scale stope fracture zone simulator. Work has also been carried out on the development of a model for interacting regions having bonded interfaces but different elastic properties (for example, dyke structures). Extensions to this work are required to allow fracture initiation at these interfaces and slip on the interfaces. An initial formulation of polygonal-shaped elements has been carried out as a first step towards the development of a three-dimensional interacting fracture growth simulator.

A number of studies have been carried out to analyse micro-fracture processes in assemblies of rock grains. It has been found that the simulated grain shape can influence the modelled post-failure load shedding behaviour. This suggests an initial approach to the development of material sensitive constitutive models for different rock types. It is important to extend these investigations to the analysis of micro and macro failure mechanisms in three dimensions and to support these studies with suitable physical modelling experiments.

Several fundamental mechanisms that lead to extension and shear fracturing around stopes have been identified. Supplementary physical modelling experiments have provided assistance in confirming proposed failure mechanisms. These include the initiation of extension failure from simulated parting planes and the initiation of wedge-like shear fractures from below a strip punch, corresponding to a pillar foundation failure. It is proposed that additional physical modelling work should be undertaken with multiaxial loading conditions. In addition, the effects of stress field rotation should be studied to understand processes of fracture growth and strength degradation that occur near incrementally advanced excavations.

Several basic mechanisms that lead to the formation of spalling fractures and borehole breakout fracturing have been identified. These mechanisms rely on the recognition of secondary tensile fractures that are induced to form adjacent to strongly crushed zones at points of high stress concentration. These mechanisms have been demonstrated by both physical modelling experiments and by numerical simulations of fracture growth.

Good progress has been made in completing a number of enabling studies that are needed prior to being able to make quantifiable proposals for improved fracture zone control. These include an insightful survey of information relating to the initial tectonic stress state and the impact of different assumptions in the implementation of numerical modelling studies. Efforts have also been made to evaluate the interaction between the excavation process (blasting) and the formation of fractures around an opening. It was concluded that this interaction could assist the formation of "bow-wave" fractures in haulages but the extent of this interaction in stopes is still unclear. Studies of creep-like deformations near stopes were initiated. This work will form the basis for determining whether the rate of face advance can be used to control the recurrence and intensity of seismic activity. It was found that a simple viscoelastic model could provide a good description of observed closure movements in particular stopes. It is also recognised that slip on discontinuities must play a fundamental role in determining the creep-like closure behaviour observed in certain stopes. Initial progress has been made in developing a method to characterize the surface roughness of selected discontinuities which can be correlated to experimental observations of creep movements on these discontinuities when they are subjected to long term sustained loading. Supplementary numerical studies have been carried out to demonstrate the effect of stress rotation on the growth of fractures from pre-existing flaws and, on a macro scale, the effect of fracture growth from parting planes in leading to horizontal stress relaxation and possible initiation of unstable behaviour which could be interpreted as a rockburst. Additional studies have also suggested that at greater depths, the degree of seismic intensity may decrease but the recurrence rate has not been estimated. The effect of increasing mining depth on rockburst potential requires further investigation.

It can be concluded finally that all major aspects of the research programme for project GAP029 in the period 1993 to 1995, have been addressed although definitive proposals for methods to engineer the stope fracture zone have not been formulated. An important mechanism that may be used to control fracture formation is the effect of blast induced fracturing. The work has laid a strong foundation of expertise in numerical and physical modelling.

6 RECOMMENDATIONS AND FUTURE DIRECTIONS

It is recommended that the experimental computer codes WAVE and DIGS should be made available in more accessible versions to the mining industry. Further work on WAVE should concentrate on relaxing the constraint of fixed orthogonal alignments of stopes and faults. In addition, experimental investigations to describe the mechanics of dynamic fracture growth should be carried out as well as studies of the interaction of seismic waves with the stope fracture zone and the mechanisms of rock bursting.

Fracture growth in three dimensions should be investigated, using extensions to the DIGS code, to develop constitutive models for the formation of fractures in different rock types. Coupled to this work is the need to characterise the fundamental nature of creep-like deformations that occur on mining induced or pre-existing discontinuities. The results of this work can be used to assemble a computer code for the simulation of the fracture zone formation as mining progresses. This would enable design studies to be carried out to determine the effect of face advance rate on the cyclicity and severity of seismic activity in different geotechnical environments and to evaluate the efficacy of support or other engineering strategies that are proposed to control the stability of the stope fracture zone.

An important by-product of these investigations is that a number of basic numerical tools will become available to produce an improved version of the MINSIM computer code which could have features of automatic element mesh generation, simulation of creep behaviour and the ability to evaluate intersecting stope-fault geometries. Consideration could also be given to the possibility of the automatic generation of planned mining sequences that would satisfy appropriate energy release constraints or other layout design criteria. This facility would greatly enhance the scope and effectiveness of conventional mine layout design procedures.